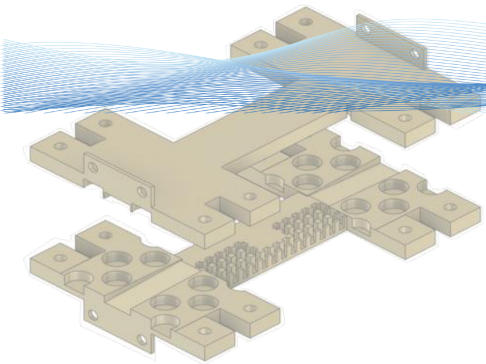

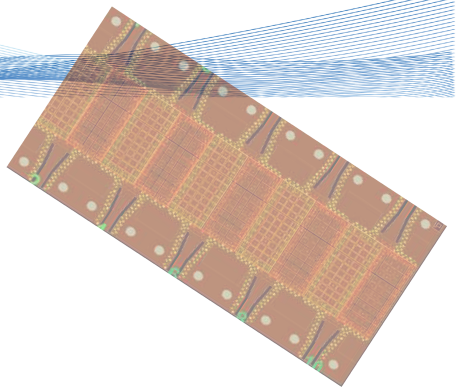

Parity Time-reversal Duality (PTD) Symmetric Structures

Iram Nadeem

PhD Thesis in Information Engineering & Science
University of Siena

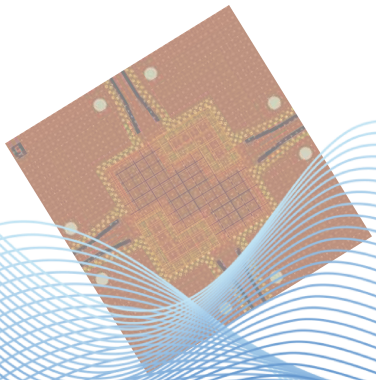

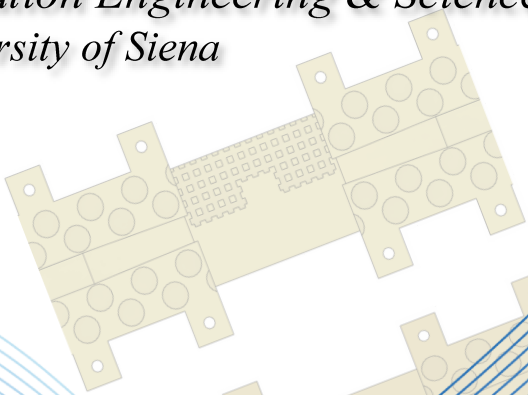

UNIVERSITÀ DEGLI STUDI DI SIENA

FACOLTÀ DI INGEGNERIA

DIPARTIMENTO DI INGEGNERIA DELL'INFORMAZIONE

Parity Time-reversal Duality Symmetric Structures

Iram Nadeem Iram Nadeem Signed 11/04/2023

Ph.D Dissertation in Information Engineering and Science

XXXV Cycle, 2019-2022

Supervisor

Prof. Stefano Maci

Co-Supervisor's

Prof. Alberto Toocafondi

Prof. Enrica Martini

SIENA

DECEMBER 12, 2022

With love to my Parents Asia Nadeem, Rifat Iqbal Nadeem and my husband Sadeque Khan

ACKNOWLEDGMENTS

This work is the result of a three year path togather with many people who, in different ways, contributed to its realization.

First and foremost I would like to acknowledge the efforts and input of my principle supervisor, **Prof. Stefano Maci**, and Co-supervisors, **Dr. Alberto Toccafondi**, & **Dr. Enrica Martini** for supporting me during the past three years.

Stefano is someone you will instantly love and never forget once you meet him. He is among one of the smartest people I know. I wish that I could be as lively, energetic, and passionate as Stefano and to someday be able to give directions to the audience as he can. His cheerful personality always makes his students feel confident. All his contributions during my time and funding to make my Ph.D. experience fruitful.

I am specially thankful to Dr. Alberto Toccafondi, for the excellent example he has provided as an outstanding professor and researcher.

This work would not have been possible without the help, suggestions, continuous and fruitful discussion with Dr. Enrica Martini. Her insight and knowledge into the subject matter steered me through this research. She is like a little angle in our group.

Besides my advisors, I wish to thank **Prof. Eva Rajo-Iglisisas** for passing me insightful knowledge about gap-waveguides technology during my visiting research studies in University of Charles III Madrid Spain. Furthermore, I want to acknowledge **Dr. Bruno Biscontini** (Huawei Technologies, Germany), Dr. Valentina Verri, Fabio Morgia and **Maurizio Mattivi** (Huawei Technologies, Italy) for financial support during the Ph.D. course, and making fruitful collaboration with professional researchers and laboratories. It is also worth mentioning **COST** committee especially **Prof. Guido Valerio** for providing me travel grant during my visiting research period in spain. It allowed my PhD studies to go the extra mile.

Friendship is a great gift that I received in these years. Therefore, I would like to thank all of my laboratory colleagues in Siena for their support, help and entertaining time: Ilir, Ravi, Laura, Anastasios, Alice, Joaquin, Christos, Giuseppe and Talha. Giuseppe was the first person to rescue me in piccolomini residence. I have extremely happy time with all these friends and have wonderful memories. I am also thankful to my office-mates Jose and Nelson in University Carlos III Madrid since, Madrid has been a great experience.

My special regards goes to Ms. Liana Smaldore for helping in each and every administrative stuff. She made life extremely easy here. My gratitude and appreciation also goes to all the team members of WaveUp; who have been a great source

of technical discussion.

Lastly, I would like to thank my parents for their love, believe, encouragement and support in all of my pursuits. Thanks to my husband **(Dr. Sadeque Reza khan)** for love, respect, care, support, sacrifices, and many more. Besides, to my sisters and my brothers who always encouraged me and supported me in this journey. I also want to mention my deep sorrow for my late grandmother and my uncle, who always showered their love and prayers on me during this period. But somehow i was unable to give them last hug. I thank everyone.

Iram Nadeem
Siena, Italy
Dec 15, 2022

ABSTRACT

Topological Edge modes (TPEMs) are the electromagnetic (EM) equivalent of the edge states in the integer quantum Hall effect that occurs due to topological phase transitions of matter, the discovery at the origin of the Nobel Prize awarded to Thouless, Haldane and Kosterlitz in 2016. The EM extension of TPEMs, originally found at atomic level, was then moved to plasmonics and microwaves areas, opening new and unexpected opportunities for innovation. The novel aspect of TPEMs is that they can be "protected against backscattering" thus, enabling a wave-guiding not affected by reflections due to disorder, imperfections, obstacles or deformations of the propagation path. TPEMs protection normally requires non-reciprocal elements. However, recent researches have shown that it can be also generated by reciprocal materials and this aspect is the main subject of this thesis.

A class of structures supporting modes protected against backscattering is the one of PTD-symmetric systems, i.e, systems invariant under the combination of the parity (P), time reversal (T) and duality (D) operators. This condition can be also fulfilled by passive and lossless reciprocal structures, provided that the electromagnetic properties become dual in Babinet sense upon mirroring with respect to a certain plane. If this condition is verified, the system is capable of supporting propagation without backscattering, i.e. the guiding structures, even if not rigorously unidirectional in topological sense, are intrinsically matched even in the presence of discontinuities if also these latter are PTD-symmetry complaint. The work in this thesis starts from the following considerations. Practical realization of dual volumetric materials can be cumbersome. However, for a homogeneously filled guiding structure, PTD-symmetry condition reduces to the duality of the boundary conditions (BCs), which can be implement through metasurfaces (MTSs). For instance, a possible PTD-symmetric structure consists of the combination of two dual parallel plate waveguides with one perfect electric conductor (PEC) and one perfect magnetic conductor (PMC) wall.

In this thesis we first describe the fundamental physics and numerical analysis of this ideal PTD-symmetric structure. It is shown that it supports a mode whose field is strongly confined at the edges between PEC and PMC. Therefore, we define this guiding structure as Bifilar Edge Waveguide (BEW). Then, two different solutions for PMC implementation through high impedance surfaces are investigated: Fakir's bed of nails and mushroom MTS. Relatively simple analytical models are considered to relate their equivalent impedance to the electrical and geometrical parameters. It is found that, compared to the Fakirs bed, the mushroom MTS is significantly more compact for a given impedance value, as the patch capacitive loading

allows for a significant reduction of the height of the pins. Simple BEW structures based on mushroom are designed by EM simulations. These include straight and segmented line branches, as well as multiple line structures. A number of prototypes are then fabricated and tested. A multiport junction working as a switchable microwave coupler is also designed, manufactured and experimentally characterized. Furthermore, alternative full metal structures based on the same concept are also investigated. Finally, a different PTD-symmetric structure, characterized by a higher degree of freedom and allowing for dual polarization operation, is presented and its potential as radiating element is investigated.

LIST OF ACRONYM

BEW	Bifilar Edge Waveguide
BC	Boundary Condition
CPW	Coplanner Waveguide
D	Duality
ELC	Edge-Line Coupler
EM	Electromagnetic
MTS	Metasurface
PEC	Perfect Electrical Conductor
PMC	Perfect Magnetic Conductor
P	Parity
PPW	Parallel-Plate Waveguide
ε_r	Relative Permittivity
SW	Slow Wave
SIW	Substrate Integrated Waveguide
TPEMs	Topological Edge Modes
T	Time-Reversal
TEM	Transverse Electromagnetic
TE	Transverse Electric
TM	Transverse Magnetic
λ	Wavelength
WAIM	Wide Angle Impedance Matching
WGs	Waveguides

Contents

List of Figures

Chapter 1

Introduction

Parity Time-reversal Duality (PTD)-Symmetric bifilar waveguides are particular waveguides that are robust against backscattering. For wave-guiding and transmission line applications PTD-symmetry theory provides a powerful solution to issues like scattering at sharp turns and manufacturing defects, as PTD-symmetric structures are endowed with natural robustness that traditional waveguides lack. The objective of the research presented in this thesis is manifold: starting from the study of the physics behind the ideal bifilar edge waveguide behavior, mathematical formulations and electromagnetic models are developed to obtain deeper understanding of the potential and limits of the approach for the design of innovative electromagnetic devices. Possible ways for practical implementations are proposed. Finally, the use of this concept for practical applications both in the field of planar microwave device and for radiating structures is explored.

1.1 PTD Symmetry

A structure is called PTD symmetric if it is invariant under the combination of the parity (P), time-reversal (T) and duality (D) transformations. An important point is that PTD systems can be formed by using reciprocal materials. In fact, time-reversal symmetry is closely related to reciprocity, albeit not equivalent. In particular, reciprocal lossless media are time-reversal symmetric [2]. Therefore, in reciprocal systems [3], the main attributes that guarantees the some propagating mode is immune to reflections is a duality link between the constitutive parameters

of the materials. For instance, assume that the parity transformation is (x, y, z) $\rightarrow$ (x, y,-z); the permittivity $\overline{\varepsilon}$ and permeability $\overline{\mu}$ tensors of a PTD-invariant system are then linked through the relationship $\overline{\varepsilon}$(x, y, z) $\cong$ V$\cdot\overline{\mu}^{\mathsf{T}}$(x, y,-z) where the superscript T denotes transpose and V is a tensor represented by a diagonal matrix with diagonal elements $\{1, 1, -1\}$. Furthermore, the magneto electric tensor $\overline{\xi}$, associated with a bianisotropic response, if not zero, must satisfy the condition $\overline{\xi}$(x,y,z) = -V$\overline{\xi}^{\mathsf{T}}$(x,y,-z) [4].

1.2 Objectives

The goal of the present thesis is manyfold.

The first goal is to investigate the properties of the particular kind of bifilar edge waveguide consisting on the combination of perfect electric conductor (PEC) and perfect magnetic conductor (PMC) walls shown in Fig. 1.1. The placement of the both walls are such a way that their inversion along y-axis produces dual boundary condition w.r.t original boundary conditions. The corresponding mode supported between these walls is denoted as bifilar edge mode.

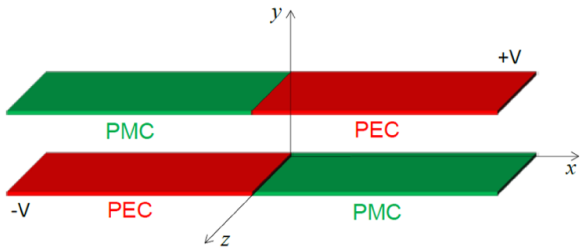

Figure 1.1: Geometry for the PTD-symmetric bifilar edge waveguide.

The second goal is to advance the state of the art dedicated to the design of bifilar edge waveguide devices, as well as their prototyping and characterization. Since PMC does not exist naturally, high impedance metasurfaces are required which can emulate this behaviour. In order to obtain compact structures, a mushroom-type metasurface is considered as high impedance boundary implementation. Accordingly, the first step in the design process was the sizing of the mushrooms to align the unimodal bandwidth of the bifilar edge waveguide within the desired operative bandwidth.

A further step consists in the design of a proper feeding structure to be used to excite the waveguide for the practical implementation. A rectangular waveguide (RWG) has been first considered and a parametric study has been conducted to determine the optimal size. Therefore, a transition RWG-bifilar edge waveguide has been modeled, with a wave port at the RWG section. Once these design processes were accomplished, different devices were designed based on this basic structure, and the performances verified through full wave simulations.

Finally, detailed prototypes based on these results were designed and numerically simulated. These include branches of straight transmission line, branch of transmission line with bends, multiport junctions and directional coupler. The considered frequency range is the Ka-band, more precisely between 22 and 30 GHz.

Next goal is to investigate this concept by using Gap waveguide technology (all metal). Metallic pins (pillars) are arranged densely to project PMC behaviour. A bifilar edge waveguide has been designed by using PEC and glide arrangement of pillars (w.r.t each other). Again RWG has been considered first, then a transition by using WR34 through tapering is considered. Fully metal means no lossy material is involved, so lossless propagation along the bent bifilar edge waveguide has been observed.

Third goal is to study the square TEM waveguide constituted by PEC and PMC, which exhibits two symmetry axes, as compared to bifilar edge waveguide. Two different types of bent PTD are deployed in the propagation paths of the square waveguide to visualize the transmissions inside them. Finally, PTD-symmetric waveguide arrays have been investigated for wide angle impedance matching properties by changing phases at the input ports.

1.3 Outline of the thesis

The core of the doctoral dissertation in organized in six chapters, detailed below.

1.3.1 Parity Time-reversal Duality (PTD) Symmetry in ideal bifilar edge waveguide

This chapter presents the analysis of the ideal PEC/PMC based parallel plate waveguide (PPW) denoted as bifilar edge waveguide (BEW). The properties of this particular kind of edge waveguide are investigated both analytically and numerically. In particular, it is shown that it supports a transverse electromagnetic (TEM) edge mode with characteristic and wave impedance equal to the impedance of free space.

Furthermore, it is demonstrated through full wave simulations that this waveguide is backscattering free in presence of discontinuity preserving the PTD-symmetry, including transition to free space. Possible solutions for its practical implementation are also considered.

1.3.2 Implementation of the Bifilar Edge Waveguides

This chapter addresses the experimental characterization of the bifilar edge waveguide consisting of a combination of perfect electric and high impedance metasurface. Rectangular waveguides (RWG) have been used to excite the BEW during the simulations. However, to make it compatible with SMA connector and with PCB technology, a proper feeding solution is required. Therefore, a grounded co-planner waveguide (G-CPW) to substrate integrated waveguide (SIW) has been used. Detailed prototype and layout of transmission line with bends and multiport junctions are shown. Experimental results confirm the possibility to guide the electromagnetic (EM) waves along the junction with low insertion losses and unique matching properties.

1.3.3 Switchable Bifilar Edge Line coupler (ELC)

A four ports edge line coupler (ELC) has been explained in this chapter. It is constituted by a parallel plate waveguide whose walls are formed by a junction between Perfect Electric Conductor (PEC) and Perfect Magnetic Conductor (PMC). Reversing the axis orthogonal to the plates interchanges the position of PEC and PMC. The ELC presented here is constituted by a 4-port junction in which each port is intrinsically matched due to the PTD symmetry, strongly coupled with a second port, strongly decoupled with a third port, and weakly coupled with a fourth port. A prototype of the coupler has been manufactured and measured. Furthermore, it is shown through simulations how the ELC ban be made electronically reconfigurable through the introduction of diodes.

1.3.4 All Metal Bifilar Edge lines

This chapter demonstrates the practical feasibility of using the bed of nails structure to construct a fully metallic PTD-symmetric bifilar edge waveguide (BEW). The waveguide design starts by considering first the ideal perfect electric condition (PEC) and perfect magnetic condition (PMC) based parallel plate waveguides

(PPW). Then, metallic pillars (Pins) are used to emulate the PMC boundary conditions. It is found that if the pillars in the upper right wall are shifted in glide manner also along the direction orthogonal to propagation gives larger unimodal band. Numerical results show the backscattering protection and the ability to confine the EM field in the proximity of the edge over a large bandwidth.

1.3.5 PTD-symmetric transverse electromagnetic (TEM) Square Waveguide

This chapter investigates the reflection and transmission properties of the square TEM waveguide constituted by two opposite perfect electric conductor and perfect magnetic conductor walls. This waveguide exhibits a parity time-reversal duality (PTD) symmetry with respect to both the diagonal axes. Furthermore, the active impedance properties of an infinite array constituted by TEM waveguides open ended in a checkerboard PEC-PMC ground plane is studied. In this case, contiguous WGs are rotated of 90° to get dual polarization. The proposed waveguide array exhibits wide angle (0°-60°) active impedance matching over a large bandwidth, together with a good isolation between the cross-polarized ports.

Chapter 2

Parity Time-reversal Duality (PTD) Symmetric Protected Edge Modes in Junctions

Recent discovery of topological insulators showed interfacial electrons transport without dissipation, even in the presence of impurities. In fact, in a broad class of electromagnetic devices, one-way power transfer that is immune to backscattering is very desirable. This backscattering protection normally requires non-reciprocal materials. However, new studies have revealed that it can also be produced by materials that are reciprocal. Due to their chiral type features, the edge modes in this instance are bidirectional but mostly immune to backscattering. This offers a remarkable robustness to a wide class of disorders, which could enable very prominent fabrication tolerance. Similarly, their immunity to backscattering at sharp bends has the potential to shrink device footprint by eliminating gradual bends or careful engineering needed at the edge to overcome losses, or higher order mode mixing when a turn is required in the waveguide.

2.1 Literature Review

Topological edge modes (TPEMs) [5] have recently attracted considerable attention, thanks to their robustness against scattering from discontinuities and capability to travel in only one direction. It is shown that the electromagnetic counterpart of the chiral edge states arising in two-dimensional electron systems subject to a large magnetic field applied perpendicular to the plane in which the electrons reside (quantum Hall effect) [6]. A basic introduction of topological phenomena in electromagnetic systems including geometric phase is given in [7]. TPEMs are usually associated to non-reciprocal elements , [8], [9], [10], [11], [12].However, the latest researches have revealed that they can also be supported by reciprocal structures [3], [13], [14], [15]. Which reveals one of the startling effect in the form of highly robust mode at the edge between reciprocal materials. This special modes, called edge mode, exist within the bandgap of the material due to sudden change in invariant across the boundaries. In this respect, the edge modes produced are bidirectional, but mainly (in the ideal cases) are immune from backscattering. Especially, in [4] it is shown that this phenomenon arises in PTD symmetric structures. i.e. in structures which are invariant under the composition of the parity, time reversal, and duality operators. This implies that PTD-symmetric systems may support waves that are insensitive to any form of perturbation or discontinuity that satisfies the PTD symmetry. Moreover, when a PTD-symmetric waveguide supports an odd number of propagating modes it is always possible to define an excitation that also guarantees the absence of reflections due to modal conversion [4]. In other words, it can be said that a bidirectional PTD-symmetric N-port networks are characterized by a scattering matrix with vanishing diagonal elements, i.e. $S_{11} = ... = S_{NN} = 0$. Thus, a PTD-invariant microwave network is always matched at all ports. Quite remarkably, this property can also be achieved in passive, lossless and reciprocal guiding structures, which implies a significant simplification for practical realization with respect to active or non reciprocal solutions. In fact, since passive, lossless and reciprocal structures are time reversal symmetric, PTD symmetry in this case is achieved anytime an axis exists in the transverse cross-section whose inversion produces dual boundary conditions (BCs) with respect to the original ones (Fig. 2.1(a)). Propagation in such guiding structures will be unaffected by any perturbation or defects that do not break the PTD symmetry. It is noted that also the perturbation introduced by termination into free space belongs to this class. The topological insulators introduced in [16], [17] are particular examples of reciprocal systems with an Ω-type bianisotropic coupling. Different symmetry-protected waveguides (WGs) proposed in the literature can be cast in

this framework [18], [19], [20]. Interestingly, PTD symmetry can be achieved also without bulk magnetic materials, since duality can be played on boundary conditions by using metasurfaces. These latter, in fact, can be conveniently used to manipulate electromagnetic fields [21–24]. In particular, the waveguide introduced

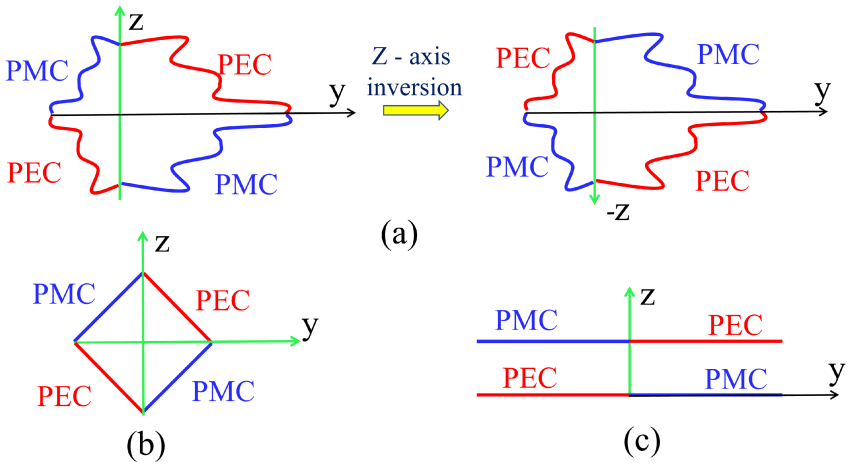

Figure 2.1: Examples of cross-sections of PTD-symmetric waveguides. (a) PTD symmetric waveguide where the z-axis is the parity axis (b) Square cross-section structure with two parity axes (both z and y-axis), (c) PTD symmetric bifilar edge waveguide with z-axis as parity axis, which is a simplified model for the structure discussed in this paper.

in [19] consists in a junction between two planar surfaces characterized by complementary impedance boundary conditions (capacitive and inductive). Similarly, an analytical study has been shown that a line wave occurs with in the complementary surfaces [25], [26] . These structures supports an edge mode, whose field is tightly confined in proximity of the junction; such a mode exhibits highly efficient propagation also along non rectilinear paths, as experimentally demonstrated in [27]. However, the structures in [19], [27] are open; as a consequence, their Green's functions are characterized by a continuous spectrum of modes and therefore, even if there is no backscattering at PTD-symmetric discontinuities, there can be radiation losses. In contrast, a PTD symmetric waveguide with a closed cross section does not suffer from this impairment. Examples of this latter class of guiding structures are presented in Fig. 2.1. In particular, the square cross section structure in

Fig. 2.1(b) has been studied in [18]. An array of such open-ended WGs has been investigated in [28], [29]. The array elements are arranged so that the overall structure still satisfies PTD-symmetry with respect to multiple axes, and this allows one to obtain wide angle beam scanning with good matching performance.

2.2 Bifilar Edge Waveguide using Ideal Boundary Conditions

A PTD-symmetric waveguide consists of the combination of two semi-infinite parallel-plate waveguides (PPWs), each consisting of a PEC and a PMC walls separated by a distance d as shown in Fig. 1.1. This structure was first suggested and numerically investigated in [18]. The transverse cross-section of the waveguide shows a potential of 2V between the PEC walls of the PPW. Every individual PPW reveals a bandgap from zero frequency to the cut-off frequency for which d = $\lambda/4$, their pairing generates a transverse electromagnetic (TEM) mode strongly confined along the discontinuity of the boundary conditions (BCs), with penetration depth of the order of the distance between the walls. This mode expresses few similarities with the modes supported at the interface between two planar surfaces with complementary surface impedances presented in [10]. However, the closed waveguide of Fig. 1.1 is PTD-symmetric with reference to the parity transformation $\{x, y-d/2, z\}$ $\rightarrow$ $\{x, d/2-y, z\}$. This declares that the supported edge mode is immune from backscattering from PTD-symmetric defects. Especially, it is noted that, since free space fulfills the PTD-symmetry requirement, an open-ended PTD symmetric bifilar edge waveguide transmits without any reflections, regardless of its thickness.

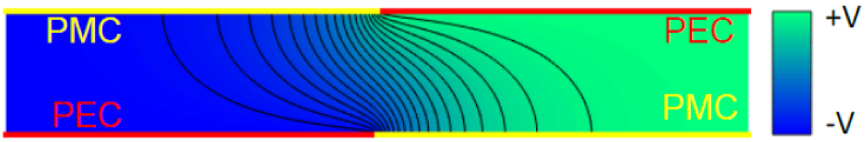

Figure 2.2: Potential distribution for the PTD-symmetric PEC-PMC bifilar edge waveguide shown in Fig. 1.1.

The exact appearance of the edge mode supported by this structure is determined in [20] with various approaches. There are three analytical forms to calculate the exact solution of TEM mode named as conformal mapping, mode-matching,

and Fourier-transform method [30], [31]. It is found that these three solutions are coincident and each of them highlights different aspects of the modal field in structure. The characteristic impedance of the TEM mode remains same as the wave impedance and free space impedance of the mode.

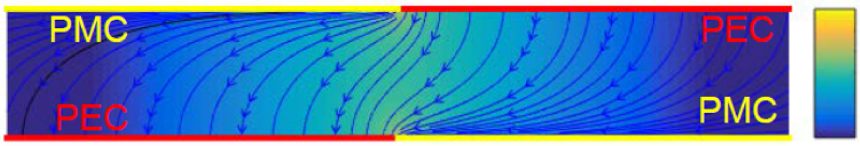

Figure 2.3: Electric field distribution for the PTD-symmetric PEC-PMC bifilar edge waveguide shown in Fig. 1.1.

Fig. 2.2 presents the distribution of the potential across the PTD-symmetric waveguide cross section in logarithmic scale, along with the equipotential contour lines. The snapshot of the electric field at the face of the waveguide is shown in Fig. 2.3.

2.3 Dispersion Analysis

As a primary step, a modal evaluation of the PEC-PMC bifilar edge waveguide has been finished to confirm the conformity of numerical outcomes in terms of dispersion curve, modal structure and characteristic impedance [20]. This implications of the theory have been investigated through the commercial software HFSS by using ideal PEC and PMC boundary conditions. This analysis is important both to define the envelope of the performances one can aim for; with real structures. The geometry for the analyzed structure is shown in Fig. 2.4. In the simulation, the geometry of the bifilar edge waveguide can be represented through a rectangular air box with proper boundary conditions to emulate the perfect electric and perfect magnetic conductors. More specifically, PEC and PMC walls have been assigned "*Perfect E*" and "*Perfect H*" boundary conditions, respectively. "*Perfect H*" boundaries are indicated in blue and "*Perfect E*" boundaries in red are shown. The separation between the walls along the z-direction is equal to $d = 1\,mm$, the overall length of the waveguide along the y-direction is equal to $L = 20\,mm$ (10 mm for each PEC or PMC wall).

Dispersion analysis has been performed by assigning Master/Slave boundary

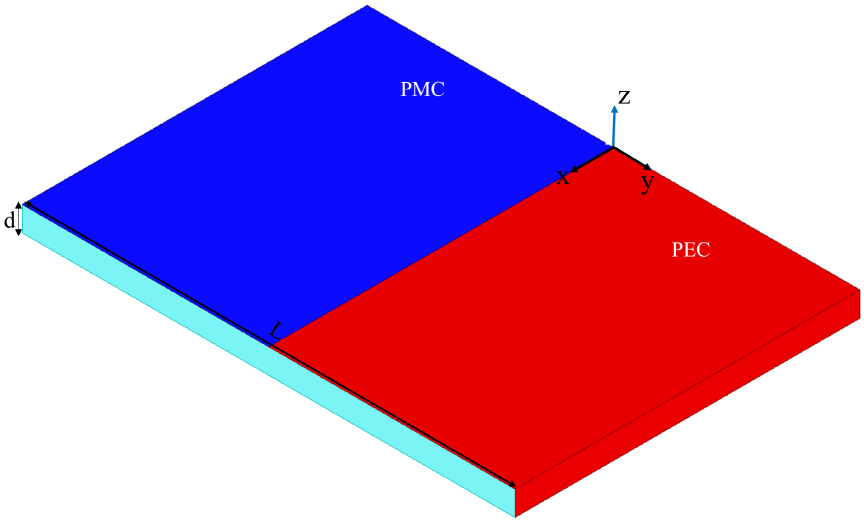

Figure 2.4: Geometry for the ideal bifilar bifilar edge waveguide simulation.

conditions at the orthogonal faces to the edge direction (x-axis) and parametric "*eigenmode*" analysis for different values of the phase shift has been applied. A "*Perfect E*" boundary has been set in the direction orthogonal to the y-axis to terminate the analysis domain. This condition has no impact on the edge mode, due to the fast attenuation of the field in the transverse direction. The dispersion curve for the edge mode is shown in Fig. 2.5. It can be seen, that it coincides with the one of free space, which is also reported in the same figure for the sake of comparison. As expected, the structure is unimodal in the considered frequency range.

The electric and magnetic field distribution at 10 GHz is shown in Fig. 2.6 and Fig. 2.7, respectively. It presents that the field distribution is totally consistent with the one predicted in [15], with high field value in correspondence of the boundary condition discontinuity at the walls, where the theory prescribes a singularity.

2.3.1 Implementation of PMC Boundary

In practice, the PMC condition can be implemented in a given frequency range through a high impedance impenetrable artificial surface or metasurface (MTS). In the microwave range, MTS are generally realized by properly patterning electrically small metallic inclusions over a thin grounded dielectric layer. In fact, when

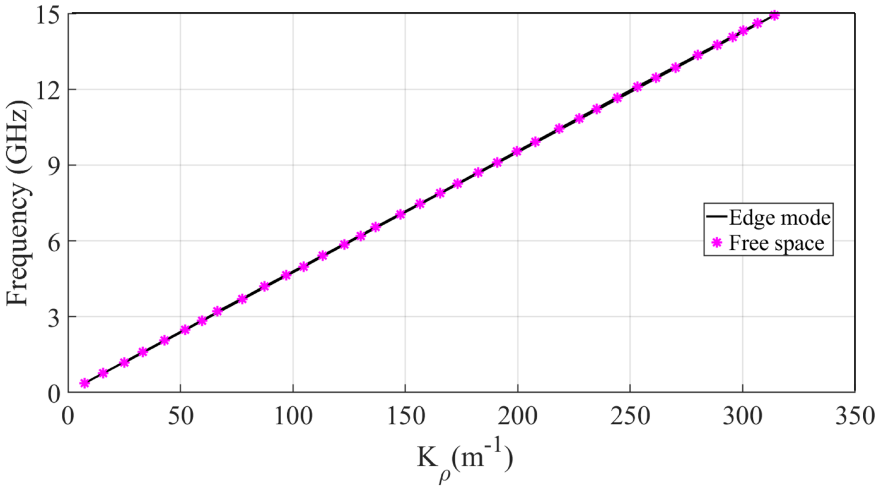

Figure 2.5: Dispersion diagram for the bifilar edge waveguide of Fig. 2.4.

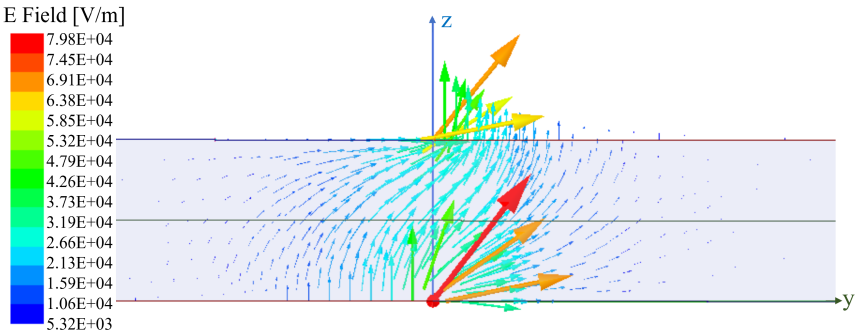

Figure 2.6: Electric field distribution at 10 GHz across the transverse section of the PEC-PMC bifilar bifilar edge waveguide

the period of the texture is much smaller than the wavelength, the structure can be described by using an effective medium model, and its attributes can be sum up into a single parameter that is called the surface impedance. This boundary condition defines the ratio of the tangential electric field to the tangential magnetic field at the surface. While a smooth conducting sheet has low surface impedance, with a specially designed geometry, the textured surface can have high surface impedance.

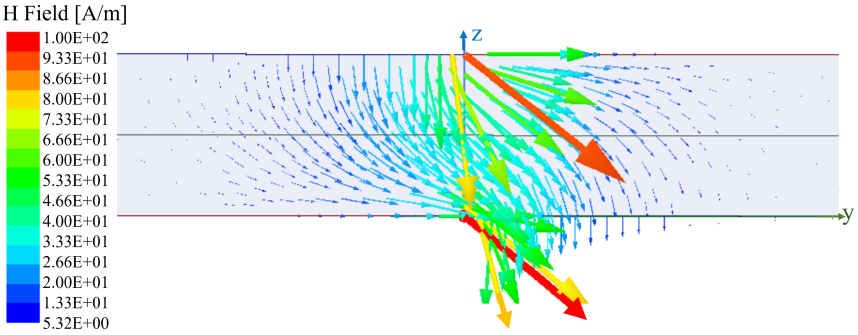

Figure 2.7: Magnetic field distribution at 10 GHz across the transverse section of the PEC-PMC bifilar bifilar edge waveguide

This property has been extensively exploited to enhance the radiation of low profile antennas or to reduce mutual coupling [32]. The high impedance condition can be verified both in terms of scattering and dispersion of the supported surface wave. First case corresponds to an electric field reflection coefficient with phase close to 0 (as opposed to the 180° phase of the PEC). Second case shows the correspondence to a bandgap, i.e. a frequency band in which the propagation of surface wave is inhibited. The two concepts are represented by the grey regions in Fig. 2.8. Two different structures for high impedance implementation are described in the following. Beside possessing the desired electromagnetic behavior and being light weight and easy to fabricate, these two structures have another important property: relatively simple analytical models are available to relate the equivalent impedance to the electrical and geometrical parameters. This is a fundamental point for the design of electromagnetic devices exploiting the edge mode phenomenology. Therefore, the bed of nails and mushroom MTS are two considered approaches.

2.3.2 Bed of nails Metasurface

The first considered structure is called Fakir's "*Bed of nails*". It consists of a periodic arrangement of thin metallic pins attached to a conducting ground plane and sunk in a dielectric layer. The geometry for the structure is illustrated in Fig. 2.9. The pins are arranged at the nodes of a square lattice of period a, have radius r_0 and height h. They are immersed in a dielectric layer of thickness h and relative permittivity ε_r. Some of the properties of this artificial surface have been known

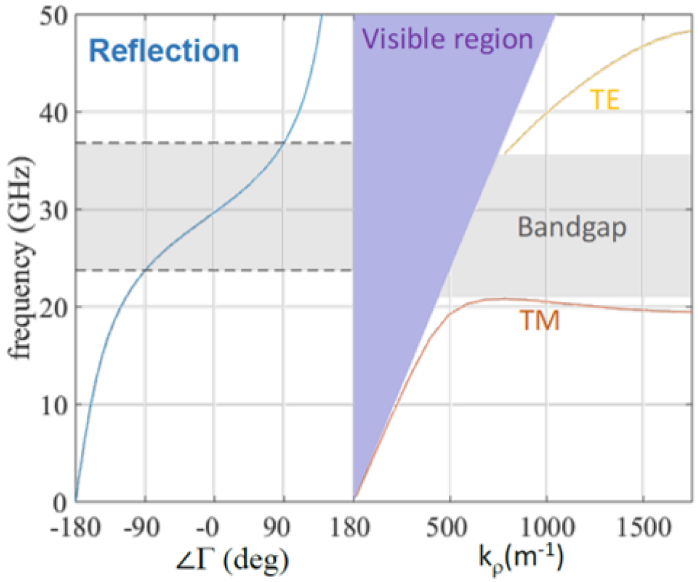

Figure 2.8: Illustration of the equivalence between the definition of high impedance in terms of surface wave (SW) dispersion and in terms of reflection coefficient

for some time [33], but only more recently an analytical model has been derived for their characterization [34], [35].

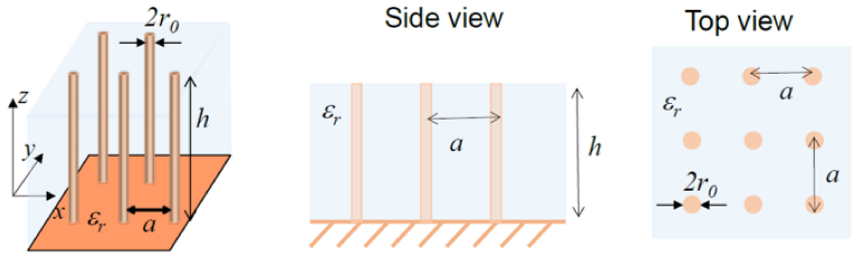

Figure 2.9: Geometry for the bed of nails MTS

The analytical model is valid when the wavelength limit ($\lambda \gg$a), is based on the of homogenization of the wire medium formed by continuous wires immersed

in a homogeneous substrate. It means modelling should be done as an effective anisotropic medium. In [36], [34] it was expressed that the wire medium is strongly spatially dispersive (i.e. its constitutive parameters depend on the propagation direction), and is represented in Fig. 2.9 by following tensor permittivity.

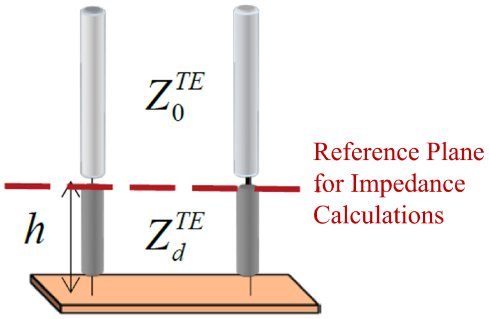

Figure 2.10: Equivalent transmission line model of the bed of mails MTS for TE polarization.

$$\underline{\varepsilon} = \begin{bmatrix} \varepsilon_0\varepsilon_r & 0 & 0 \\ 0 & \varepsilon_0\varepsilon_r & 0 \\ 0 & 0 & \varepsilon_0\varepsilon_{zz} \end{bmatrix} \tag{2.1}$$

Where the effective relative permittivity along the metallic via is given by

$$\varepsilon_{zz} = \varepsilon_r(1 - k_p^2/k^2 - q_z^2) \tag{2.2}$$

In (2.2), $k = k_0\sqrt{\varepsilon}_r$ is the wavenumber of the base material, k_p is the plasma wavenumber which depends on the geometrical properties of the lattice [34]

$$k_p = \frac{1}{a}\sqrt{\frac{2\pi}{ln(\frac{a}{2\pi r_0})} + 0.527} \tag{2.3}$$

This structure can be studied as grounded slab of thickness and their equivalent impedance can be derived by considering the scattering of the impinging plane wave, distinguishing between the transverse magnetic (TM) and transverse electric (TE) polarization. In general the TE polarization has the electric field parallel to the ground plane therefore, it does not interact the vias. As a result, for this polarization

the bed of nails MTS is equivalent to the bare dielectric slab backed by a ground plane.

The corresponding equivalent impedance is obtained from the analysis of the equivalent transmission line shown in Fig. 2.10, where the ground plane is represented by a short circuit, the dielectric slab by a branch of transmission line with propagation constant $k_{zd} = \sqrt{k^2 - k_\rho^2}$, where $k_\rho = k_0 \sin\theta_0$, and characteristic impedance $Z_d^{TE} = \xi_0 \mathrm{k}/\sqrt{\varepsilon_r} k_{zd}$, and the free space by an indefinite transmission line with propagation constant $k_z 0 = k\cos\theta_0$ and characteristic impedance $Z_0^{TE} = \xi_0(k_0/k_{z0})$, Therefore, the equivalent impedance for the TE polarization is

$$Z_s^{TE} = jZ_d^{TE}\tan(k_{zd}h) \tag{2.4}$$

In case of TM polarization the electric field has a vertical component, and therefore it interacts with the pins. The scattering problem can be rigorously handled by expanding the electromagnetic field in a proper set of modes in the artificial dielectric. The wire medium supports three modes: a TEM mode, a transverse magnetic (TM-z) mode and a transverse electric (TE-z) mode, with the following dispersion equations

$$TEM\,mode : K_z = k \tag{2.5}$$

$$TM\,mode : K^2 = k_\rho^2 + k_x^2 + k_y^2 + k_z^2 \tag{2.6}$$

$$TE\,mode : K^2 = k_x^2 + k_x^2 + k_y^2 + k_z^2 \tag{2.7}$$

An impinging TM polarized wave can excite the TM and TEM modes, not the TE mode. By imposing the proper boundary conditions on the ground plane ($\hat{n}$ x E$|_{z=0}$= 0) and the continuity of the tangential electric and magnetic field plus the additional boundary condition [37] $\varepsilon_r E\cdot\hat{n}\,|_{z=h^-} = \varepsilon_r E\cdot\hat{n}\,|_{z=h^+}$ at the interface between the free space and wire medium (z=h), the closed expression of the total field can be obtained, from which equivalent surface impedance is derived

$$Z_s^{TM} = Z_0^{TM}\frac{kk_p^2\tan(kh) - k_\rho^2\gamma_{TM}\tanh(\gamma_{TM}h)}{\varepsilon_r\gamma_0(k_p^2 + k_\rho^2)} \tag{2.8}$$

Here, $\gamma_{TM} = \sqrt{k_p^2 + k_\rho^2 - k^2}$ and $\gamma_0 = \sqrt{k_\rho^2 - k^2}$. This is link to an inductive reactance for low frequencies ($h \ll \lambda_d$, where λ_d is the dielectric wavelength). The impedance become high when h approaches $\lambda_d/4$. This mimics the behaviour of a

PMC. From equation 2.4 and 2.8 following analytical formula of reflection coefficient has been derived

$$\Gamma^{TE,TM} = \frac{Z_s^{TE,TM} - Z_0^{TE,TM}}{Z_s^{TE,TM} + Z_0^{TE,TM}} \tag{2.9}$$

It is noted that equation 2.4 and 2.8 can also be applied to slow waves (i.e. waves with $\mid k_\rho \mid \gg k_0$) which is helpful in studying the dispersion of the surface wave (SW) supported by the bed of nails based MTS.

$$Z_s^{TE,TM} + Z_0^{TE,TM} = 0 \tag{2.10}$$

2.3.3 Mushroom Metasurface (MTS)

The mushroom metasurface was introduced by Sievenpiper as a compact high-impedance boundary [38]. It consists of array of patches printed over a grounded dielectric slab pierced with metallic vias. Compared to the bed of nails solution, the mushroom MTS is significantly more compact, as the height of the pins can be significantly reduced due to the patch capacitive loading.

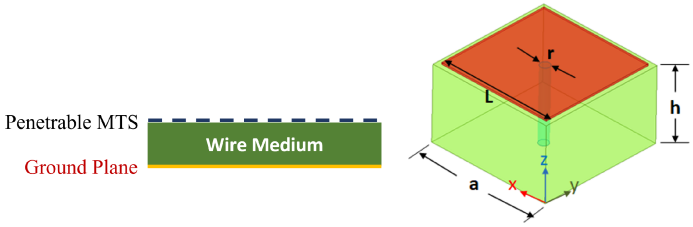

Figure 2.11: Model of the mushroom MTS as a grounded slab of wire medium capped with a penetrable MTS

In fact, the mushroom metasurface can also be seen as a grounded slab of wire medium topped by a penetrable MTS [39] consisting of square patches as shown in Fig. 2.11. This penetrable equivalent impedance of the square patches MTS has been derived in [40]. It can be define as follows for the two polarizations.

$$Z_g^{TM} = -j\frac{\eta_{eff}}{2\alpha} \tag{2.11}$$

$$Z_g^{TE} = -j\frac{\eta_{eff}}{2\alpha(1 - \frac{k_0^2}{k_{eff}^2}\frac{sin^2\theta}{2})} \tag{2.12}$$

Where

$$\alpha = \frac{ak_{eff}}{\pi} \ln\left[\frac{1}{\sin(\frac{\pi(a-L)}{2a})}\right] \tag{2.13}$$

$$k_{eff} = k_0\sqrt{\varepsilon_{eff}}$$

η_{eff} is the wave impedance of the uniform host medium while ε_{eff} is the relative effective permittivity. α is called the grid parameter [41].

$$\eta_{eff} = \frac{\zeta_0}{\sqrt{\varepsilon_{eff}}}$$

$$\varepsilon_{eff} = \frac{\varepsilon_{eff}+1}{2}$$

While a and L are period and the patch side length, respectively. The impenetrable equivalent impedance of the mushroom MTS can be calculated as the shunt connection of the bed of nails MTS and of the equivalent impedance of the patch layer

The high impedance metasurfaces are required to design practical structures that can mimic the behavior of the ideal PMC. A necessary condition for the existence of unimodal propagation supported by the edge mode is the existence of a bandgap for the two halves of the structures. In fact, the unimodal bandwidth of the bifilar edge waveguide is contained in the bandgap of the two constituent parts.

2.4 Propagation

The second step is to investigate propagation inside a rectilinear ideal bifilar edge waveguide, to assess the degree of robustness against backscattering from PTD-symmetric discontinuities. The geometry for this analysis is shown in Fig. 2.12. Similar to the previous section, "*Perfect E*" and "*Perfect H*" boundaries are indicated in blue and red color, respectively.

Wave ports have been assigned at terminations orthogonal to the x-axis. Dimensions of the waveguide are: $L1 = 6\,mm$, $L2 = 10\,mm$, $L3 = 6\,mm$ and $L4 = 22mm$. Simulated scattering coefficients are reported in Fig. 2.13.

As it can be seen, there are negligible reflections (due to numerical issues), and the power is practically completely transferred from one port to the other, despite the abrupt discontinuity in the edge path. This is due to the PTD-symmetry of the structure, combined with the fact that the bifilar edge waveguide is unimodal in the considered frequency range. Fig. 2.14 shows the electric field distribution at 30 GHz for the structure of Fig. 2.12 excited at port 1.

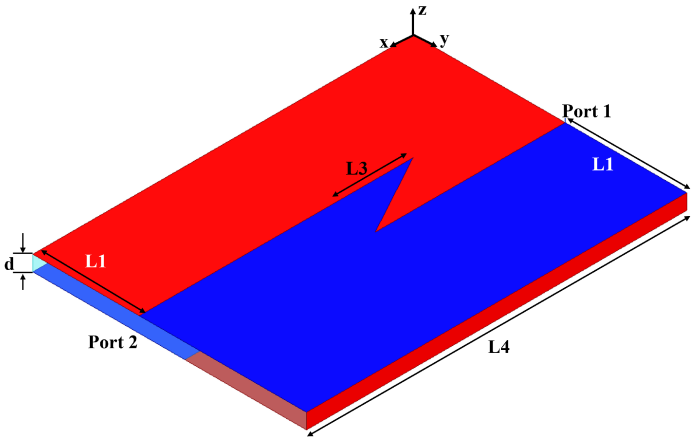

Figure 2.12: Geometry for the non rectilinear path of the PEC-PMC bifilar edge waveguide

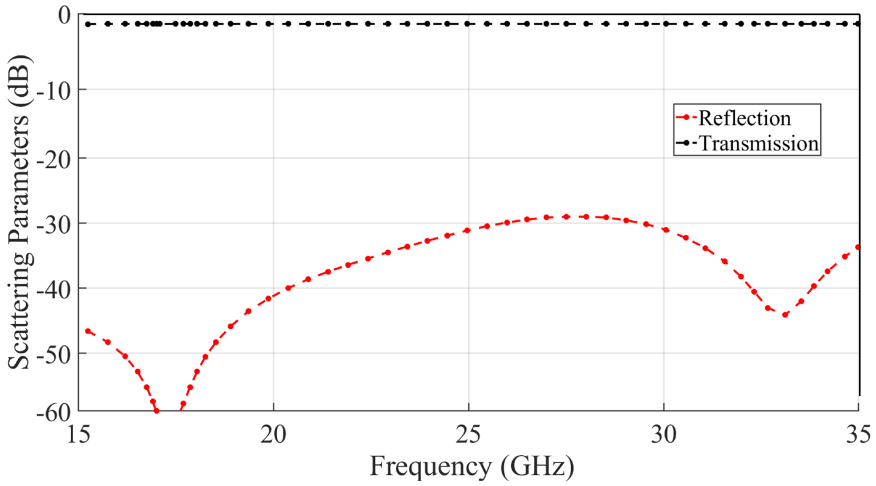

Figure 2.13: Simulated scattering coefficients for the non rectilinear path of the PEC-PMC bifilar edge waveguide

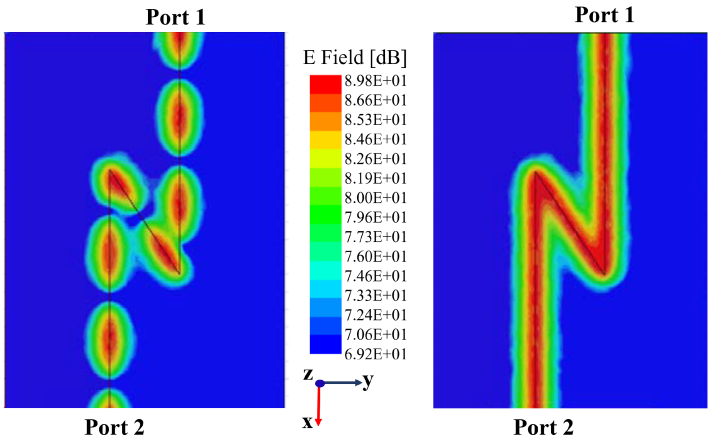

Figure 2.14: Simulated E-field distribution (instantaneous amplitude : Left) (complex amplitude : Right)

2.5 Transition to Free Space

A terminated bifilar edge waveguide represents an abrupt transition between the waveguide and free space. Since free space is a PTD-symmetric structure, this discontinuity is expected to present low reflections, despite the small thickness of the bifilar edge waveguide itself.

It is also noted that, as a difference from the cases in the previous section, the free space is not unimodal, because it supports a continuous spectrum of modes. However, both the modal and the characteristic impedance of the TEM edge mode are equal to free space impedance, and this provides a good matching in the transition from the bifilar edge waveguide and the free space. This has an important impact for the design of radiating structures. In particular, the robustness against reflections can be exploited to design arrays that remain well matched under different scanning conditions.

The robustness of the concept has been verified through simulations of a terminated ideal PEC-PMC edge WG surrounded by free space. First, the configuration reported in Fig. 2.15 has been simulated. It consists of a piece of bifilar edge waveguide, with separation between the walls equal to $d = 1\,mm$, terminated on an air brick, with radiation boundaries over its surfaces (except for the area corresponding to the waveguide section). A wave port is defined on the opposite side

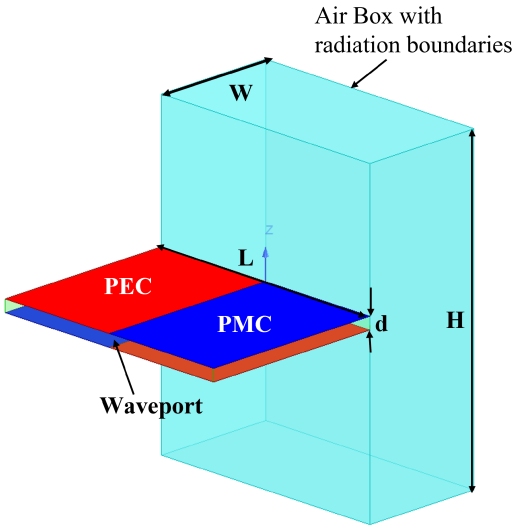

Figure 2.15: Geometry for the terminated edge waveguide with air box in front. Dimensions are: d = 1 mm; H = 20 mm, W = 5 mm, L = 12 mm

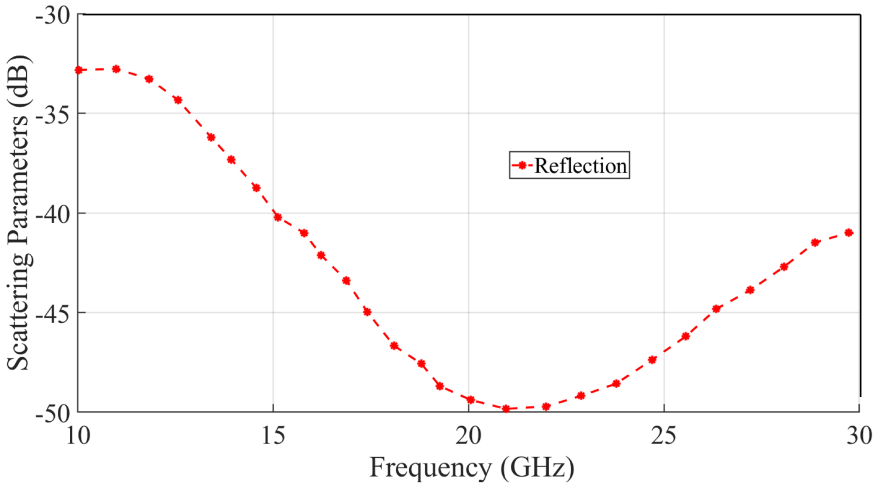

Figure 2.16: Simulated reflection coefficient for the terminated edge waveguide

of the air box. The reflection coefficient for this configuration is reported in Fig.

2.16. As it can be seen, in spite of the very small spacing between its walls (equal to $\lambda \div 30$ at 10 GHz), the bifilar edge waveguide is well matched to free space over the whole frequency range. In order to more accurately model the radiation phenomenon, it is desirable to have air all around the structure.

2.6 Summary of the chapter

Bifilar edge waveguides consisting of only reciprocal materials and robust against backscattering have been considered both theoretically and from the point of practical implementation. The study starts from the analysis of the ideal PEC-PMC bifilar edge waveguide. It is shown that this waveguide support a TEM mode with characteristic and wave impedance equal to the impedance of free space. Through full wave simulations, it is also illustrated that this waveguide is backscattering free in presence of discontinuity that preserves the PTD-symmetry, including its transition to free space. It has been also shown that the behavior of the PMC in bifilar edge waveguide can be mimicked in practice, by using high impedance MTS. In particular, bed of nails and mushroom MTS have been considered in detail, providing simple analytical models for their characterization. In conclusion, full wave simulations on the real structure have shown the dispersion curve, demonstrating the existence of a unimodal band, and very low backscattering in the presence of curved propagation paths with sharp bends.

Chapter 3

Backscattering Protection in PTD-Symmetric Bifilar Edge Waveguides

This chapter describes the design and experimental characterization of microwave structures based on parity time-reversal duality symmetric bifilar edge waveguides (PTD-BEWs) realized through a parallel plate waveguide loaded by a metasurface. The analyzed structures include transmission lines with bends and multiple line arrangements. Due to their unique symmetry properties, these structures are robust against backscattering, thus, resembling the behaviour of topological waveguides, despite the fact they are reciprocal. This makes it possible to guide the electromagnetic (EM) waves along the edge with low insertion losses and unique matching properties. Measurements, performed in the frequency range between 24 and 32 GHz, have confirmed the feasibility of the theoretical concept. [1]

[1] This chapter has been published as "Experimental Verification of Backscattering Protection in PTD-Symmetric Bifilar Edge Waveguides" in *IEEE Transaction on antennas and propagation, 2022* [42]

3.1 Introduction

Use of parallel plate waveguide (PPW) as transmission lines by applying PTD symmetric operator was first considered in [20]. PPW consist of ideal PEC and PMC as explained in previous chapter, tells that ideal PMC does not exist therefore, high impedance mushroom MTS of certain dimensions are required to realized the bandgap and unimodal region through dispersion analysis [43]. It shows a supported unique mode strongly confined at the edges between PEC and mushroom MTS. In the simulations, rectangular waveguides (RWG) have been used to excite the structure. In the realization, the RWG is substituted by a grounded coplanar (CPW) waveguide to benefit from the printed circuit board (PCB) technology. Three layers of dielectric materials are glued together by means of two layers of Astra MT77 Prepreg 1035LD of certain thickness each. The first dielectric layer is Rogers RO3003, with a top and bottom metallization made by copper. The third layer is also of the same material as the first one, with same metallization on the top and in the bottom. Hence, this chapter thoroughly explain the evidence of robust unidirectional propagation in it.

3.2 Dispersion of Bifilar-edge Waveguide

For the practical implementation of the waveguide in Fig. 3.1 is performed by using a mushroom type metasurface to emulate PMC BC. The unit cell of this metasurface consists of a square patch printed on a grounded dielectric substrate and connected to the ground plane through a central via, as shown in the inset of Fig. 3.1. In the ideal case of Fig. 2.1(b) each half of the structure consists of a PPW with PEC/PMC BCs on the two plates; for separation distances between walls smaller than a quarter of wavelength, such a waveguide does not support any modal propagation.

In the practical implementation, the PMC is substituted by a mushroom metasurface designed to exhibit high impedance in the desired frequency band. This way, each half the PTD-BEW, which consists of the mushroom metasurface covered by a metal plate, individually exhibits a bandgap in the same frequency band. A parametric study has been carried out in order to optimize the mushroom unit cell. Finally, the following geometrical parameters have been selected: size of the unit cell a = 1.6 mm, side of the square patch L = 1.45 mm, via radius r = 0.1 mm. The space between the PEC wall and the top of the mushroom is filled by a dielectric with relative permittivity $\varepsilon_r = 2.33$ and has a thickness d = 0.508 mm. The resulting structure has been analyzed with Simulia CST. The dispersion diagram,

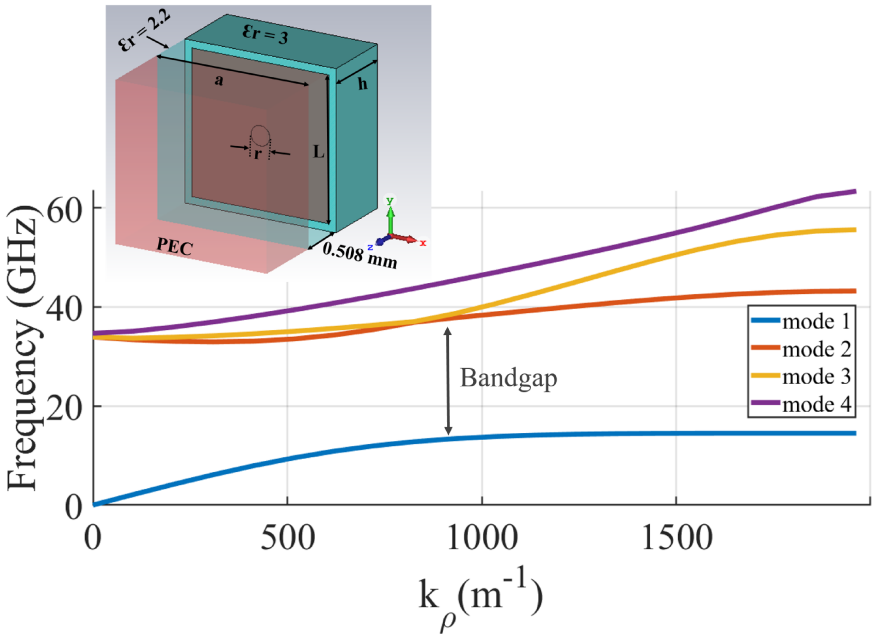

Figure 3.1: Dispersion diagram of the PEC-covered mushroom metasurface.

reported in Fig. 3.1, exhibits a bandgap between 15 GHz and 32 GHz.

When the waveguide in Fig. 3.1 is paired with an analogous structure with PEC on bottom and mushroom on top, the two edge-lines at the junction support a bifilar edge wave, whose field is exponentially attenuated on the two sides $x > 0$ and $x < 0$ with a penetration depth (inverse of the attenuation constant) approximately equal to the separation distance between the top surface of the mushroom and the PEC wall, d. Since the field is confined between the two edge lines, the structure resembles a bifilar transmission line. The dispersion diagram of this structure is reported in Fig. 3.2 along with the light line in the filling dielectric. It is worth noting that the light line crosses the BEW dispersion curve at the frequency where the mushroom surface better emulates the PMC. Around this point, the edge mode is quasi-TEM. In fact, for the ideal PEC-PMC BCs, the supported mode is TEM [20], [2], but the practical implementation of the PMC through mushrooms introduces a limited dispersion, so that the mode will be quasi-TEM. It is noted that around the central frequency, at which the mode is perfectly TEM, the dispersion curve crosses the light line, which means that around that frequency the mode exhibits a transition from a

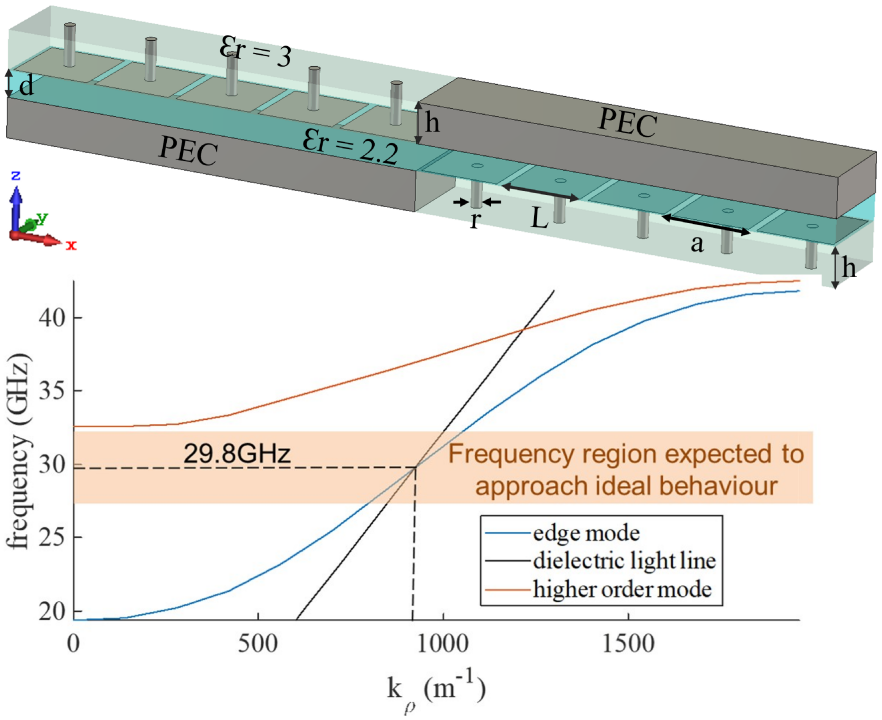

Figure 3.2: Dispersion diagram of the PTD-BEW. The black line represents the light line in the dielectric filling the waveguide.

fast wave to a slow wave. This occurs also in other closed guiding structures with impedance loaded walls, for example in the realization of the waveguide in Fig. 2.1(b) with practical high impedance surface, due to the fact that the impedance of the walls changes from inductive to capacitive [44]. As opposed to the case of ideal PEC/PMC BCs, this transition is associated to a group velocity smaller than the speed of light. Despite this effect, the backscattering protection seems to be preserved. The unimodal bandwidth ranges from 19.36 GHz (the cut-off frequency of the edge mode) to 32.57 GHz (the cut-off frequency of the higher order mode), corresponding to a percent bandwidth of approximately 50 %. However, the percentage bandwidth in which the structure is expected to approach ideal behaviour, represented by the shaded area in Fig. 3.2), is around 20 %.

3.3 Basic Bifilar Edge Waveguide Structures

The first considered structure, represented in Fig. 3.3, has been used to design a practical feeding arrangement to excite the PTD-BEW. It consists of a branch of PTD-BEW based on the basic unit cell introduced in the previous section and shown in Fig. 3.2, connected at the two sides to two sections of RWG. The height of the RWG has been set equal to the distance between the mushroom surface and PEC wall in the PTD-BEW (i.e., 0.508 mm), and its width has been varied to obtain a good matching over the frequency band of interest. A parametric study has been conducted on HFSS to this end. The reflection coefficients resulting from

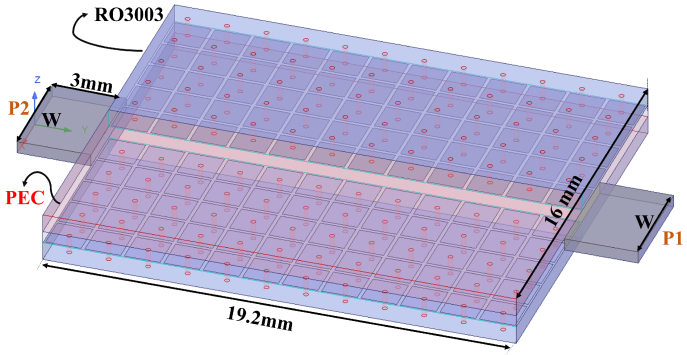

Figure 3.3: Branch of Bifilar Edge WG fed by RWGs.

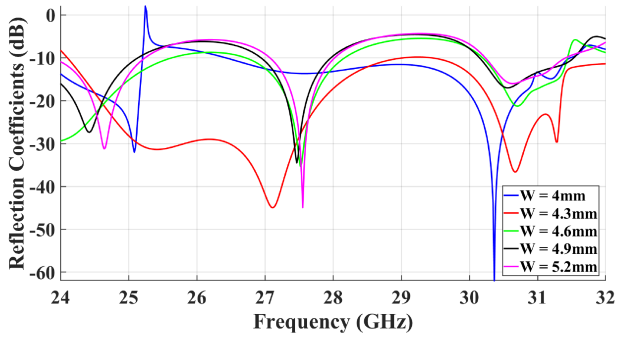

Figure 3.4: Simulated reflection coefficient for different values of the RWG width, W.

this parametric study, with the width W ranging between 4.1 mm and 4.8 mm, are reported in Fig. 3.4. For the smallest size, the low frequency peak corresponds to the cut-off frequency of the waveguide; results are therefore to be considered significant only above that frequency.

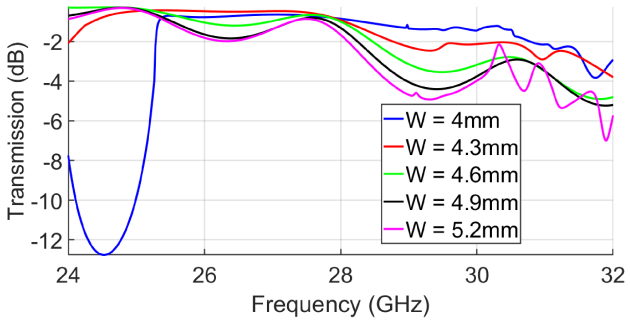

Figure 3.5: Simulated transmission coefficient for different values of the RWG width, W.

Fig. 3.5 presents the amplitude of the transmission coefficient for different value of W. The best matching performance in the frequency range between 25 and 32 GHz is obtained for W = 4.3 mm. This value makes the modal impedance of the TE_{10} mode of the RWG close to the intrinsic impedance of the TEM-BEW.

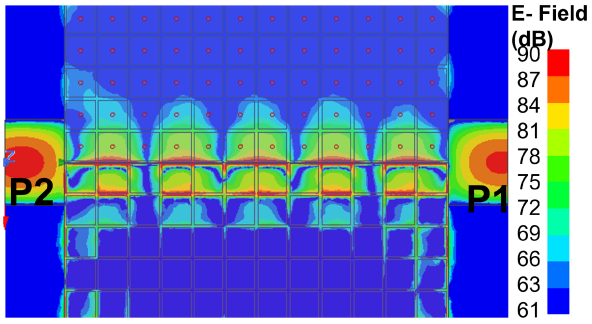

Figure 3.6: Snapshot of the electric field in the central longitudinal section of the structure in Fig. 3.3 when the port on the left (P2) is excited.

Fig 3.6 presents a snap shot of the amplitude of the electric field inside the

waveguide. As can be seen, the field is confined at the bifilar junction of PEC and mushroom, with a penetration distance approximately equal to a couple of mushroom unit cells. A certain coupling of the RWG with the lateral edges is also perceivable from the picture.

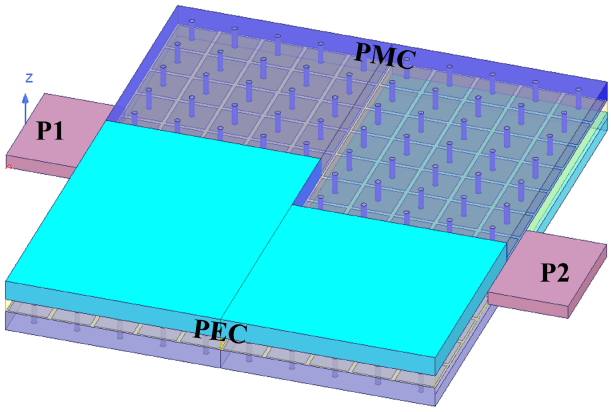

Figure 3.7: PTD-BEW path with 90° bends. The light blue color denotes the PEC part of the top-wall

Once the feeding structure has been designed, other configurations can be analyzed. Fig 3.7 shows a WG path with 90° bends (segmented PTD-BEW). This structure serves to test the robustness of the guiding structure against reflections. The PTD-BEW is entirely enclosed by metallic walls laterally.

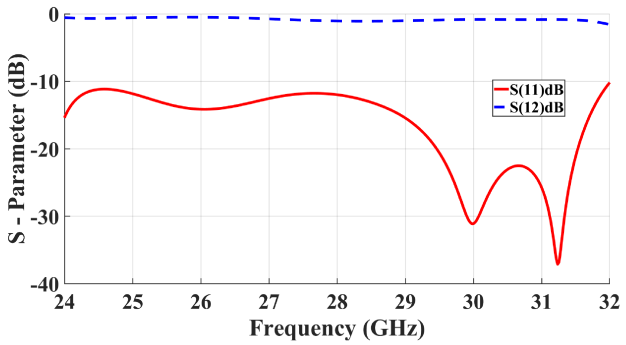

Figure 3.8: Simulated Matching of the bifilar edge WG at 90° bend.

From the simulated S-parameters reported in Fig. 3.8 we observe that reflection at the input port is limited over the entire bandwidth. The reflection coefficient is below -20 dB in the frequency range between 29.5 GHz and 31.5 GHz, where the PTD-BEW is expected to better emulate the ideal behavior (Fig 3.2). It is worth noting that these results also include the effect of the two transitions to RWG, which s the major cause of reflections.

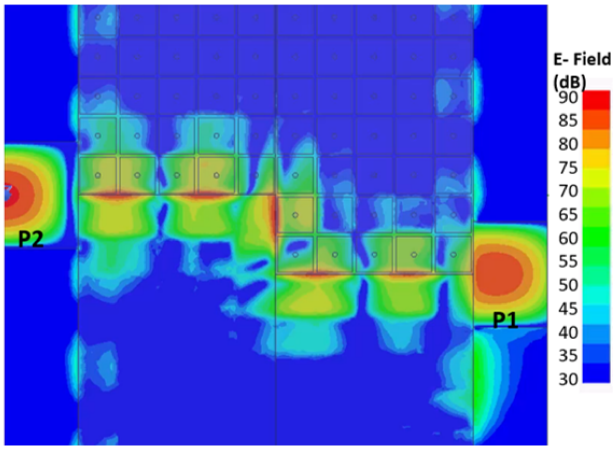

Figure 3.9: Snapshot of the electric field in a longitudinal cross-section for the PTD-BEW with 90° bends.

A snapshot of the electric field in the longitudinal cross section can be seen in Fig. 3.9. We observe that the field is properly confined at the edge throughout the entire path and the propagation follows the bends.

3.4 Detailed Prototype Design

PTD-BEW prototypes have been realized in PCB technology. The stratification of the prototypes is shown in Fig.3.10. Three layers of dielectric materials are glued together by means of two layers of Astra MT77 Prepreg 1035LD of thickness 0.126 mm each. The first dielectric layer is Rogers RO3003 of thickness 0.762 mm, with a top metallization made by copper of 0.06 mm and a bottom one of 0.05 mm. The third layer is also of the same material as the first one, with 0.05 mm metallization on the top and 0.06 mm in the bottom.

In between those two layers of RO3003 (used for the realization of the mush-

Figure 3.10: Stack-up of the prototypes.

room metasurface) there is a layer of Rogers RT5870, which has $\varepsilon_r = 2.33$ and electric loss tangent equal to 0.0012.

Fig. 3.11 shows the cross-section of the PTD-BEW structure transverse to the propagation direction. The region that should act as PEC is created by a dense distribution of metallic vias made of copper crossing the RO3003 layer, while the mushroom surface is realized in the same dielectric layer, with the external metalizations acting as ground planes and the patches created in the inner metalizations and connected to the external copper layer by vias. All vias have radius of 0.2 mm and the mushroom patches are immersed in the prepreg.

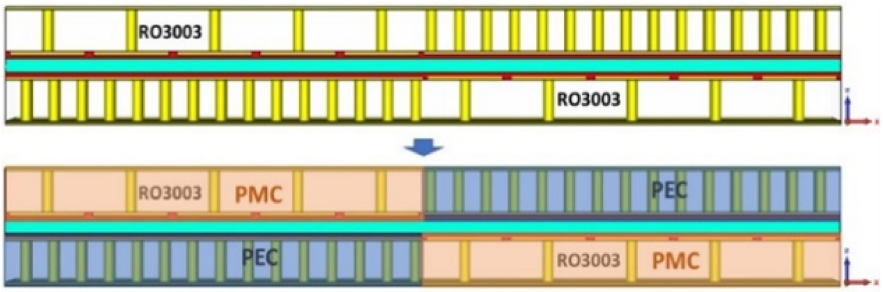

Figure 3.11: Transverse cross-section of the PTD-BEW. The prepreg is represented in red, copper in yellow, Rogers RT5870 in light blue. The bottom picture highlights the regions emulating the ideal PEC/PMC BC.

The examples discussed until here are with RWG feeding. An alternative solution more convenient for PCB realization, and including a transition to SMA connector is presented in Fig. 3.12. This solution includes a transition from a grounded-coplanar waveguide (G-CPW) to a substrate-integrated waveguide (SIW), which is used to feed the PTD-BEW [45], [46], [47]. The basic rules for the design of the SIW are provided in [48], [49]. The central strip of the G-CPW has an initial width of $w_0 = 1.56\,\text{mm}$ to exhibit $50\,\Omega$ at the input port, while the width at the end

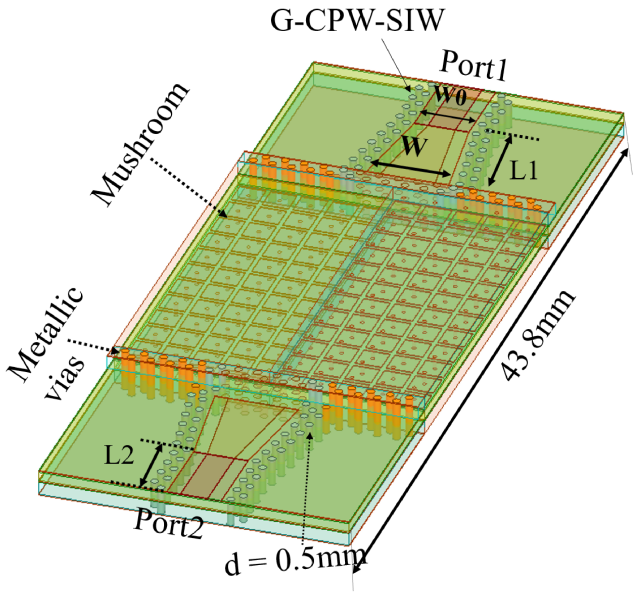

Figure 3.12: Straight PTD-BEW section fed by a G-CPW port. The feeding structure includes a transition to SIW.

of the tapered section is $W = 4.3\,\text{mm}$. The lengths $L1$ and $L2$ of the tapered and non-tapered sections, approximately 12 mm. The diameter of the vias for the feeding structure is $d = 0.5\,\text{mm}$. There are few metallic vias of 0.7 mm crossing all the dielectric layers (both RO3003 and RT5870) enclosing the PTD-BEW waveguide to support the handling of the structure. The strip of the G-CPW is printed at the same level of the mushroom surfaces patches. Taking into account the additional thickness due to the presence of the prepreg, the thickness of the RT5870 was taken equal to 0.254 mm in order to achieve performance similar to the ones obtained without prepreg and a thickness of 0.508 mm.

The branch of PTD-BEW includes 12 unit cells, and the total length of the structure, including the feeding sections, is 43.8 mm. A length corresponding to 5 unit cells of the mushroom metasurface has been considered in the transverse direction for each side; the overall width of the structure is 16.5 mm.

The simulated scattering coefficients of this structure are shown in Fig. 3.13. The structure exhibits good matching over the whole bandwidth from 25 to 32 GHz and low losses (the transmission coefficients is larger than -1 dB up to 30.5 GHz,

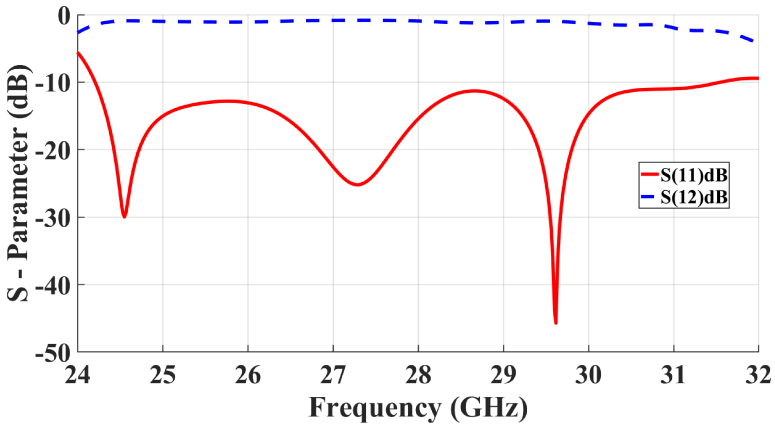

Figure 3.13: Simulated scattering coefficients of the structure shown in 3.12

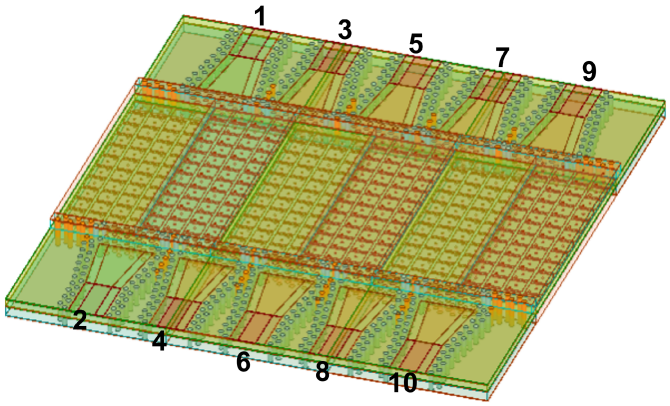

Figure 3.14: Multiport PTD-BEW structure in which five BEW sections are arranged together.

with an average value of 0.6 dB.

The second considered structure is an arrangement of parallel PTD-BEWs and it is used to investigate the mutual coupling between them. Five pieces of BEW WGs are realized in the same PCB to obtain a multiple port configuration as shown in Fig. 3.14. Each BEW has 4 mushrooms unit cells for each side in the transverse cross section, and the same 4 unit cells are shared by two adjacent waveguides. It

is important to note that there is no physical separation between the various BEW structures. The distance between the centers of adjacent line ports (and therefore between adjacent edge junctions) is 8 mm which is approximately 0.8 free space wavelengths. The simulated coupling coefficients among different ports are reported in Fig. 3.15. It can be seen that the coupling is always lower than -30 dB between ports located in the same side, and below -20 dB for ports located at opposite sites. At the same time, the matching of each channel appears unaffected by the presence of the other channels.

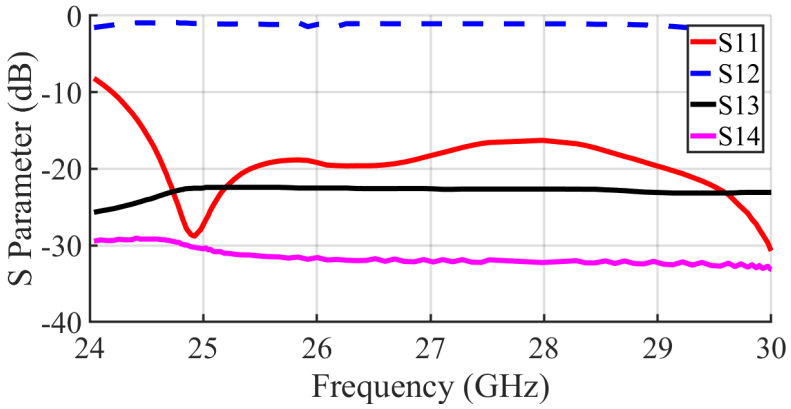

Figure 3.15: Simulated coupling coefficients for the structure in Fig. 3.14

3.5 Experimental results

To verify the findings from the simulated results following different layouts has been manufactured and measured in huawei research center for ka-band.

3.5.1 Straight PTD-BEW section

Fig. 3.16 shows a picture of the realized prototype of a straight PTD-BEW section fed with a GCPW-to-SIW transition, according to the design presented in the previous section. Fig. 3.17 shows the measured scattering parameters in a range from 20 to 36 GHz.

It is seen that the structure presents a reflection coefficient smaller than -7.5 dB across the whole band from 24 to 31 GHz, and smaller than -15 dB within the sub-

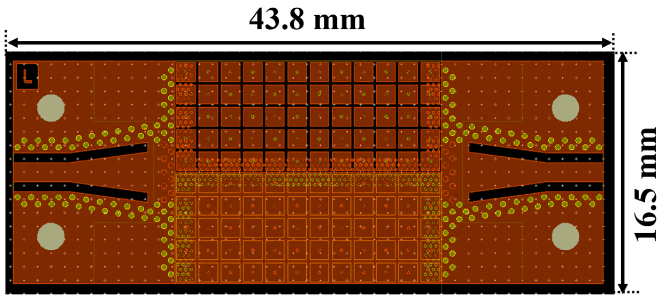

Figure 3.16: Layout of the realized PTD-BEW section with GCPW-to-SIW transitions.

band from 24 to 26.5 GHz. The transmission coefficient is around -1.5 dB between 24 and 31.5 GHz. The discrepancy with respect to simulations is thought to be due to realization imperfections and higher losses in the real materials.

Fig. 3.18 shows a different realization of a straight PTD-BEW section with GCPW-to-SIW transition. In this case, only three mushrooms unit cells are used in the transverse direction, while 12 unit cells are used in the longitudinal direction.

The measured results for this structure are illustrated in Fig. 3.19; the reflection coefficient is generally lower than in the previous case, with a bandwidth at -9.5 dB between 24.5 and 31.5 GHz, probably due to a better realization. The insertion loss is still around -1.5 dB.

The layout in Fig. 3.20 is relevant to a longer PTD-BEW section, including 24 unit cells, for a total length of 63.6 mm. In this case, five mushrooms unit cells are considered in the transverse direction.

The relevant measured results can be seen in Fig. 3.21. The structure exhibits an insertion loss around -2 dB, with a good matching between 24 and 26.5 GHz and between 29 and 30.8 GHz.

3.5.2 Segmented PTD-BEW structure

The layout of a segmented PTD-BEW structure is presented in Fig. 3.22. The path is constituted by a single square meander, with four 90° bends. This layout is analogous to the one in the example given in Fig. 3.7 and it is used to test the robustness of the propagation against discontinuities in the path.

Despite the abrupt discontinuities provided by the four right-angle bends, mea-

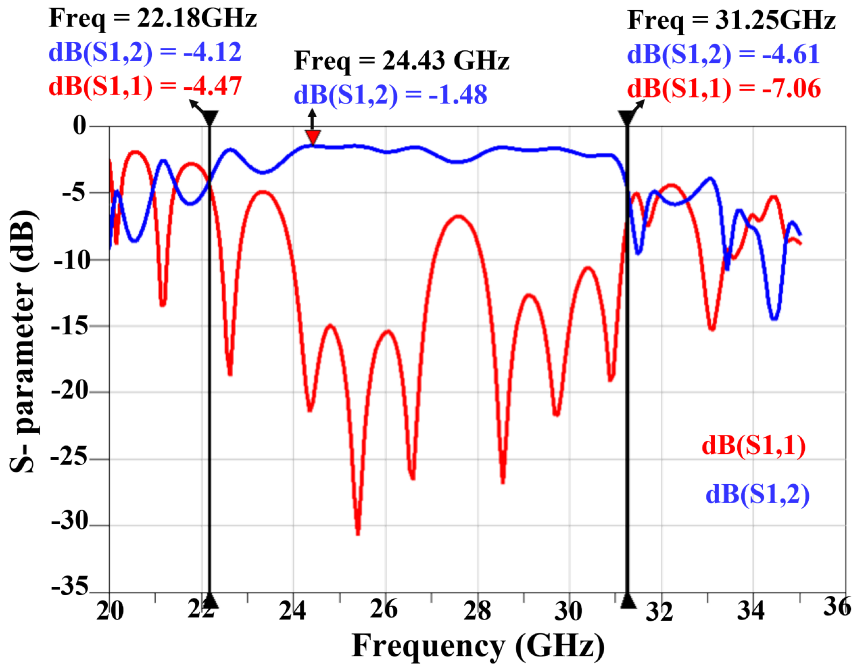

Figure 3.17: Measurements of S_{12} (blue line) and S_{11} (red line) in the range 20-36 GHz.

surements in Fig. 3.23 show the same level of matching seen for the straight path (around -10 dB in the range from 24 to 31 GHz) with -2 dB of insertion loss.

3.5.3 Multiple PTD-BEW

The last structure analyzed consists in an arrangement of adjacent PTD-BEW sections and its layout is shown in Fig. 3.24.

The distance between adjacent lines is about 16 mm, corresponding to about one wavelength at the lowest frequency of the bandwidth. It can be seen from Fig. 3.25 and Fig. 3.26 that the measured level of cross coupling has an average value of -50 dB in the range 20-30 GHz, with a maximum value of -45 dB. The transmission coefficients is around -1.7 dB.

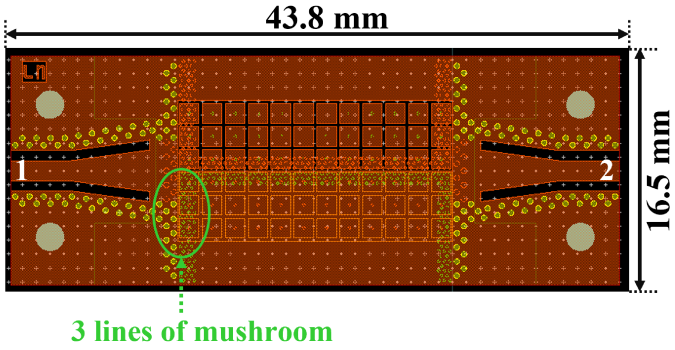

Figure 3.18: Layout of the PTD-BEW section with GCPW-to-SIW transitions with a smaller number of mushroom unit cells.

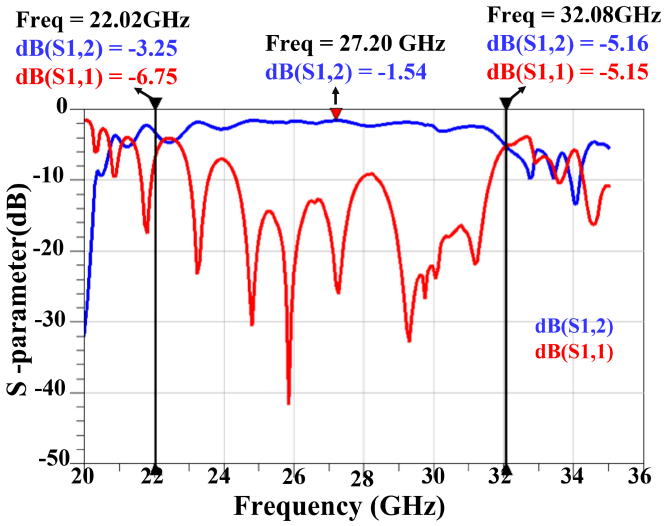

Figure 3.19: Measurements of S_{12} (blue line) and S_{11} (red line) in the range 20-36 GHz for the layout shown in Fig. 3.18

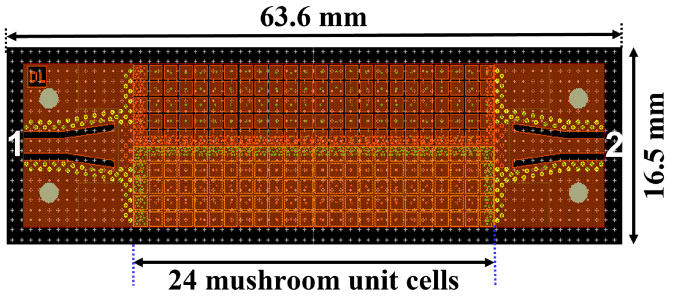

Figure 3.20: Layout of a PTD-BEW section with 24 mushroom unit cells in the longitudinal direction and GCPW-to-SIW transitions.

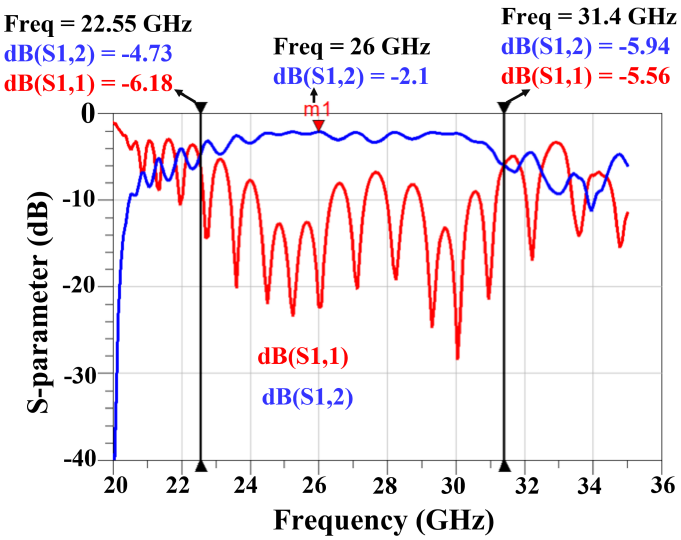

Figure 3.21: Measurements of S_{12} (blue line) and S_{11} (red line) in the range 20-36 GHz.

3.6 Summary of the chapter

The experimental verification of robust propagation in the PTD-symmetric BEW proposed in [20] has been carried out in this chapter. The practical feasibility of the

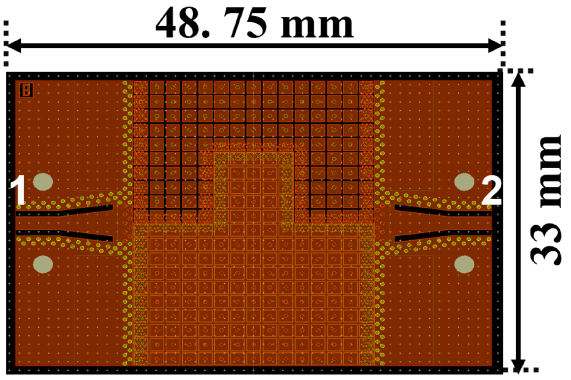

Figure 3.22: Layout of the PTD-BEW path with 90° bends.

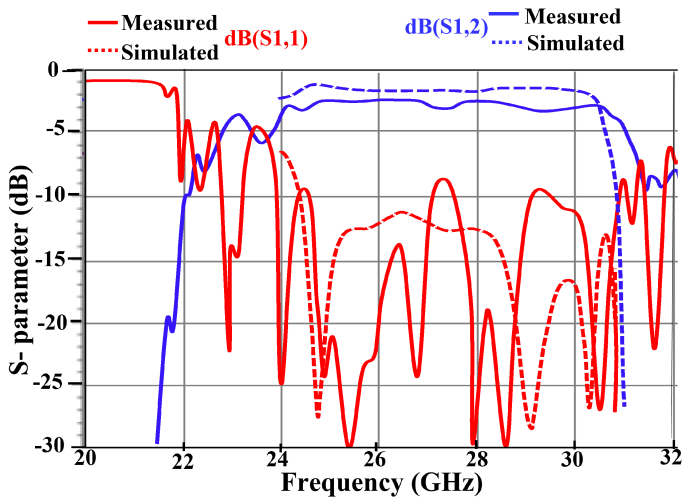

Figure 3.23: Measurements of S_{12} (blue line) and S_{11} (red line) in the range 20-36 GHz.

structure has been demonstrated in the range between 22 to 32 GHz. For practical implementation, mushroom metasurfaces have been used to emulate the PMC BCs. The analyzed structures include transmission line with bends and multiport junctions. Despite the passivity and the absence of non-reciprocal elements, the PTD-

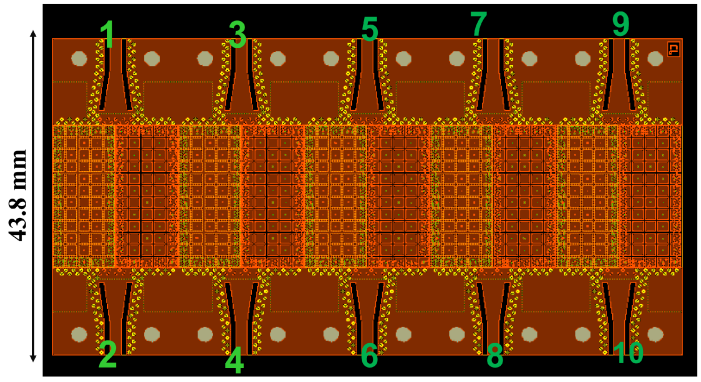

Figure 3.24: Layout of the multiple PTD-BEW structure.

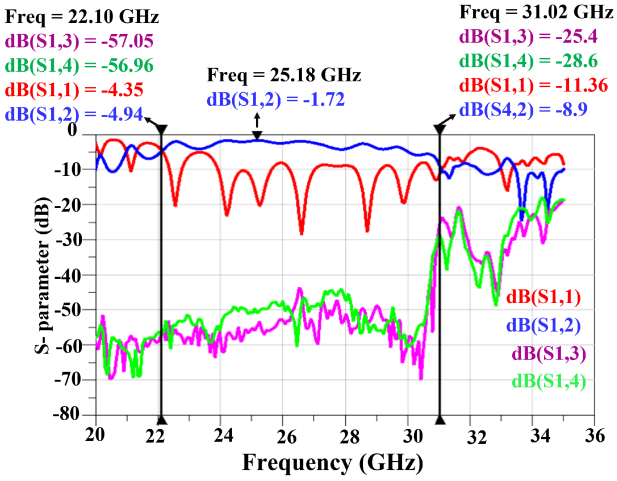

Figure 3.25: Measurements of S_{12} (blue line), S_{11} (red line), S_{14} (green line) and S_{13} (magenta line) in the range 20-36 GHz.

BEW is immune from reflections for those discontinuity which respect the PTD symmetry. Thanks to this property, it is possible to guide the bifilar mode along bended paths with low insertion loss and good matching. In the simulations of the structures we did not include any losses, because our focus was on the demonstration of backscattering protection feature. In the fabricated structure we had some

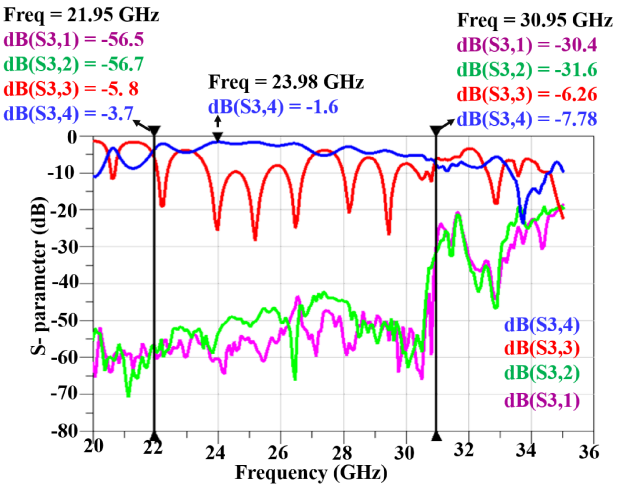

Figure 3.26: Measurements of S_{34} (blue line), S_{33} (red line), S_{32} (green line) and S_{31} (magenta line) in the range 20-36 GHz.

losses which were caused by two sources: (i) finite conductivity of the metal and (ii) losses in the dielectric. Leakage towards the lateral PPWs, on the other hand, is prevented due to the existence of a bandgap. It is also worth noting that other type of bandgap structures, such as the ones used in gap waveguide technology, could be used to reduce losses. This is currently being considered and will be the subject of future work. It should be also noted that the leakage in the lateral structures is prevented only in the bandgap region, which represents a limit to the operational bandwidth of any device that uses the PTD-BEW, such as beamformers or couplers. In spite of the many criticalities related to the manufacturing, experimental results have been found fully satisfactory. This paves the way to the possibility of designing new microwave devices with low return losses up to the Ka band.

Chapter 4

Switchable Bifilar Edge-line Coupler

In this chapter, a four port broadband Edge-Line Coupler (ELC) based on Parity Time-reversal Duality (PTD) symmetry has been designed, constructed and measured. The PTD-BELs are constituted by a parallel plate waveguide whose walls are formed by a junction between PEC and PMC boundary conditions. The ELC presented here is constituted by a 4-port junction in which each port is intrinsically matched due to the PTD symmetry, strongly coupled with a second port, strongly decoupled with a third port, and weakly coupled with a fourth port. The ELC is designed by using mushroom for the PMC portion of the device; the connection is based on a switch circuit which imposes open and short conditions on the two opposite sides of the structure. Switching simultaneously the open and short circuits reroutes the signal in a different port, while maintaining the same level of coupling with the other ports. A static prototype has been built and its measurements have confirmed the matching performance and the good directionality of the coupler in a broadband frequency range between 24 and 30 GHz. [1]

[1] This chapter has been published as "Switchable Edge-line Coupler Based on Parity Time-Reversal Duality Symmetry" in *Scientific Reports, 2022* [50]

4.1 Introduction

PTD-BELs are used to design a switchable directional coupler suitable for PCB technology realization. Directional couplers are fundamental components for several microwave and millimeter-wave systems, and various solutions have been developed for their implementation [51]. Rectangular waveguide realizations are suitable for high-performance and high-power applications [52]. However, they are bulky, rather expensive and difficult to integrate with other circuit components. On the other hand, branch-line hybrid and coupled-line directional couplers in stripline and microstrip technologies offer the advantages of compactness, planarity, low fabrication cost, and integrability with active devices. In the recent years, substrate-integrated waveguide (SIW) solutions have been developed as a compromise between the previous technologies. These include planar single [53, 54] and multilayer [55] structures, as well as three dimensional configurations [56]. They normally use slots (multiple apertures or a continuous one, depending on the desired coupling level) in the common wall of two adjacent SIW waveguides. In all the cases above, the couplers are static. However, some applications require the possibility to either reroute the signal towards a different port or change the coupling level of the coupled port. Various approaches have been reported for low-frequency (less than 5GHz) couplers with tunable power division ratio [57–59] and some other also include direction switching capability [60, 61]. In this chapter, we present a compact solution for a switchable directional coupler whose design is based on PTD symmetry theory

4.2 Ideal PEC-PMC Case

Consider a geometry consisting of a parallel plate structure with distance h between the two plates. Each plate has four quadrants alternating PEC and PMC BCs (Fig. Fig. 4.1). In pairing the top and bottom walls, the PEC and PMC quadrants are placed one on top of the other (see Fig.Fig. 4.1a and Fig. 4.1b). This structure is PTD symmetric with respect to the axis z orthogonal to the plates ("parity axis"), since changing z in -z makes the BCs dual.

This arrangement can also be seen as a 4-port junction constituted by the confluence of four PTD-BELs, a kind of edge WG which has been theoretically studied in [20] and experimentally verified in [28]. This transmission line is robust to backscattering for any PTD symmetric discontinuity, like the one at the central point of the junctions. Therefore, according with the PTD theory, the $S_{ii}, i = 1..4$ parame-

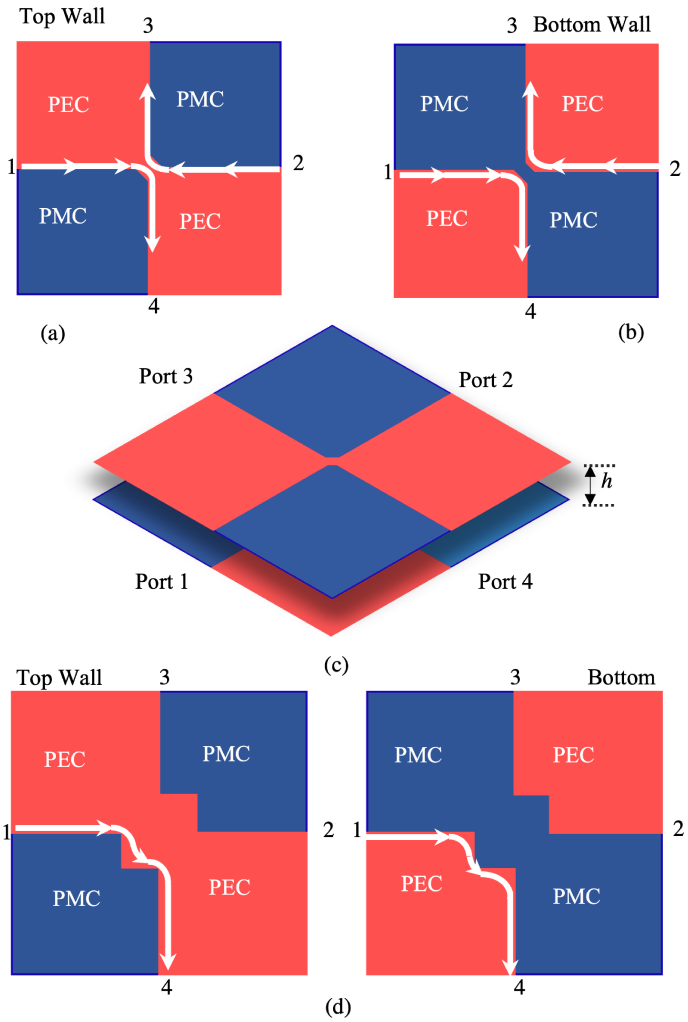

Figure 4.1: Ideal 4-ports coupler composed by a parallel plate with four alternating PEC/PMC squares on top (a) and dual wall on the bottom (b). A small bridge at the central connection maintains the PTD-symmetry of the device with respect to the orthogonal axis.(c) Three dimensional view of the coupler. (d) Alternative geometry with a larger central part.

ters at the input ports are rigorously zero, namely, the 4-port junction is perfectly matched at the ports. However, it is important to note an aspect which has an impact on both modelling and practical implementation: the BCs at the connection point at the confluence of the four PTD-BELs is undefined. If one does not properly attribute the BCs at this point, this implies a violation of the PTD symmetry. To guarantee a PTD symmetry, it is necessary to attribute opposite BCs on the top and bottom walls at the connection point, for instance PEC on the top wall and PMC on the bottom wall (Fig. 4.1).

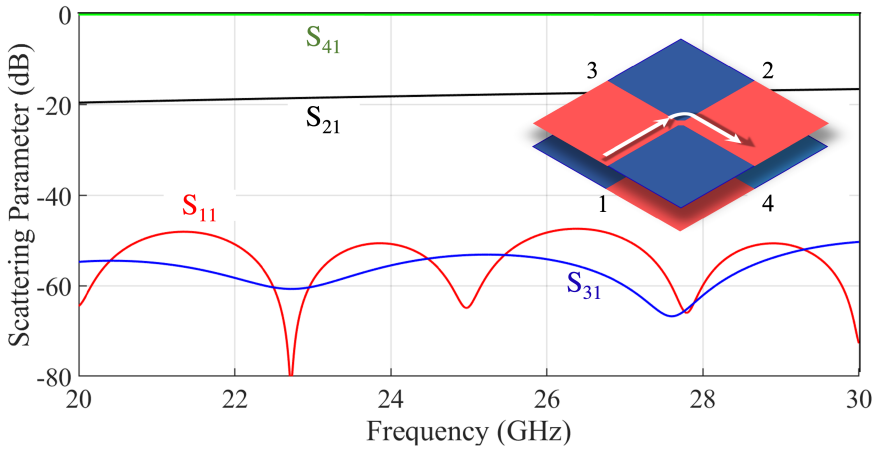

Figure 4.2: Simulated scattering parameters of the ideal 4-ports junction shown in Fig. 4.1(c).

In this way, the complementary behavior when swapping z in $-z$ is ensured, and therefore the matching property at the 4 ports is guaranteed. In practice, the attribution of the BC to the central point of the junction is done on the top wall by connecting the PEC quadrants with a small PEC bridge (see Fig.4.1a), and on the bottom wall by separating PEC quadrants by a PMC gap (see Fig.4.1b). The attribution of complementary BCs at the central point not only renders the structure PTD-symmetric, but it also defines edge-line paths between Ports 1 and 4 and between Ports 2 and 3, as shown by the arrows in Fig. 4.1a and 4.1b. These arrows represent the flow of electric currents, essentially concentrated on the metallic part close to the edge. The magnetic currents follow the same edge driven path on the PMC part. It is also worth noting that this behavior is independent of the size of the central bridge. Therefore, for practical implementation, one can also increase the

size of the central part, as represented in Fig. 4.1d. The current will still flow along the edges without any reflection. As we will see next, this arrangement allows to better control the coupling factor to port 2 in practical realization.

Fig 4.2 shows the scattering parameters S_{ij} obtained by a numerical full-wave analysis, performed through Simulia CST for the case in Fig. 4.1c.

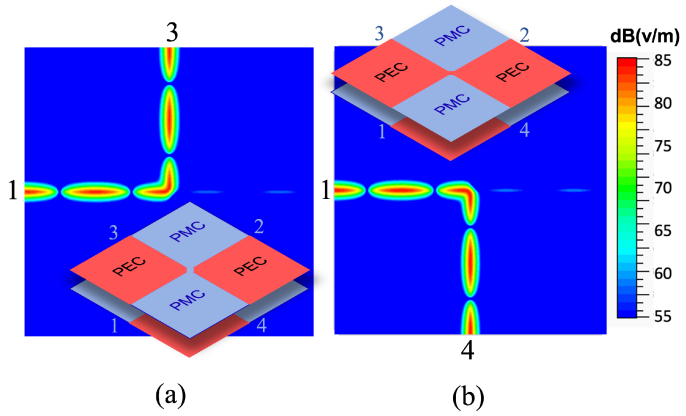

Figure 4.3: Amplitude of the electric field in the ideal 4-ports junction for dual BCs on the central gap, as shown in the insets

Ideal BCs are assigned to the two walls, which are separated by a distance $h = 1$ mm. Port 1 is fed by exciting the modal field distribution at the corresponding section. The S-parameters show that Port 1 is almost perfectly matched and nearly all the input power is delivered to Port 4. Isolation of Port 3 is very high, only limited by the numerical accuracy, and the coupling to Port 2 is around 20 dB in all the considered bandwidth. The directivity of this coupler (power at port 2 over the power at port 3) is therefore more than 35 dB in all the bandwidth.

The remarkable thing is that the behavior can be completely changed by only acting on the central connection point. In fact, if the PEC and PMC BCs of the central bridge are swapped, Port 1 will be connected to Port 3, and Port 2 to Port 4. Figure 4.3 illustrates the amplitude of the electric field for the two different conditions of the central connections: in the first case, power supplied to Port 1 is delivered to Port 3 and weakly coupled to port Port 2, with a high isolation of port 4. In the second case, power supplied to Port 1 is delivered to Port 4 and coupled to port 2, with a high isolation of port 3. In both these cases, the return loss is excellent. This means that it is possible to re-route the signal by changing

the nature of a very small region at the junction central point. This can be done in practice by using simple switching elements like PIN diodes.

4.3 Design based on mushroom metasurfaces

The practical implementation of the ideal 4-ports PTD coupler in Fig. 4.1 is obtained by using a mushroom type metasurface [38] to emulate PMC. The unit cell of this metasurface and corresponding, dispersion analysis is same as shown in previous section of Fig. 3.2. Due to the finite dimension of the mushroom unit cell, we cannot create only a small-bridge at the confluence point, but we must have a finite region consisting of a certain number of unit cells. Therefore, the structure in Fig. 4.1d describes the practical implementation of the ideal switchable coupler better than the one in Fig. 4.1c.

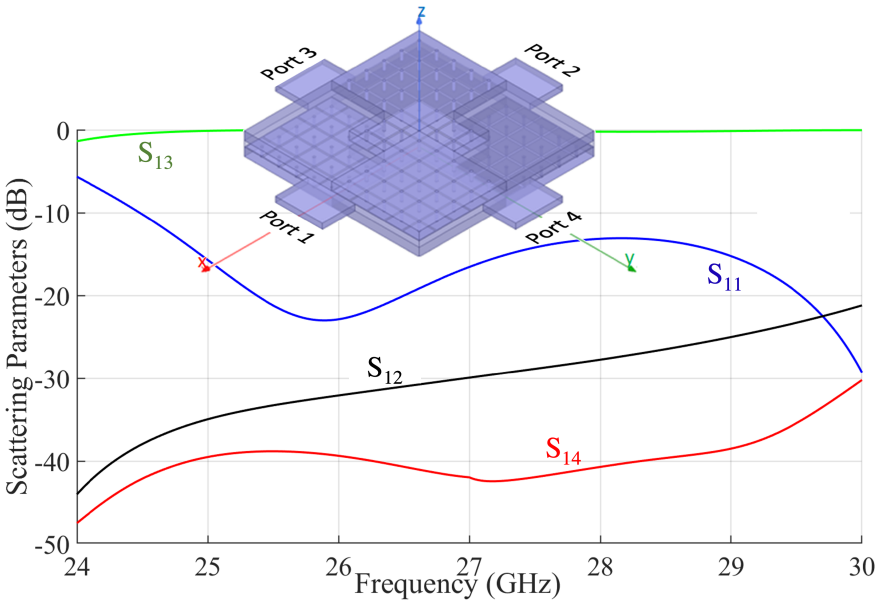

Figure 4.4: Simulated scattering parameters for the ELC coupler implemented through mushroom metasurfaces with 4x4 unit cells in the central part.

Two designs have been analyzed. In the first design, a 4x4 unit cell region is defined at the center, with mushroom distribution on the top wall and metal on the

bottom. The structure is illustrated in the inset of Fig. 4.4. The arrangement is such that the directionality is from Port 1 to Port 3 and from Port 2 to Port 4. The simulated scattering parameters for this structure are shown in Fig. 4.4. It can be seen that in the considered frequency range almost all the power fed at Port 1 is delivered to Port 3 with a good return loss. The coupling factor to Port 2 ranges from 35 dB up to 20 dB in the bandwidth. Isolation of port 4 is almost constant around 40 dB up to 29 GHz.

4.3.1 Switchable Edge-line Coupler

A second design is shown in Fig. 4.5(a). In order to realize a reconfigurable device for signal routing it is necessary to switch the behavior of the central region from PEC to PMC.

This is implemented by setting 2x2 mushroom unit cells in the central region on both the top and the bottom walls, and by introducing switchable connections (PIN diodes) among adjacent patches (see Fig. 4.5b and 4.6c).

When the diodes are on, they short-circuit the patches, thus emulating the PEC behavior. When the diodes are off, they act as small capacitance, thus, leaving substantially unaffected the PMC-type mushroom behavior. In the full-wave analysis, the diodes are first emulated with ideal short or open circuits; in practice, they can be biased by using channels inside the pins of the mushroom [38]. Fig 4.5(b) and 4.6(a) shows two different configurations for the states of the diodes and Fig. 4.5(c) presents the relevant scattering parameters as simulated by Ansys HFSS v2020 [1].

Rectangular waveguides (RWGs) have been used to feed the ports, and have been included in the numerical simulation; the thickness of the RWGs has been fixed equal to the distance between the mushroom surface and the PEC walls (i.e., 0.508 mm), while their width is set to 4.3 mm, which is the value that provides the best matching to the BEL. As expected, in both the configurations the power supplied to Port 1 is delivered to Port 3, and the return loss is quite good. In the case of Fig. 4.5(b), isolation of Port 4 is better than 25 dB in the frequency range $25 - 29.5$ GHz and the coupling level of Port 2 is constantly around 12 dB in the same bandwidth. As a consequence, the directivity of this coupler is better than 13 dB, quite stable in the mentioned bandwidth. The configuration in Fig. 4.6(c) exhibits a similar behaviour, but with a slightly increased coupling to port 2 and a lower isolation. This shows how the switches can not only reroute the signal with good matching, but also control the amount of power transmitted to the ports.

Comparison with the results of Fig. 4.4 shows essentially a different coupling level of port 2, due to the different number of cells used in the central region. Fig.

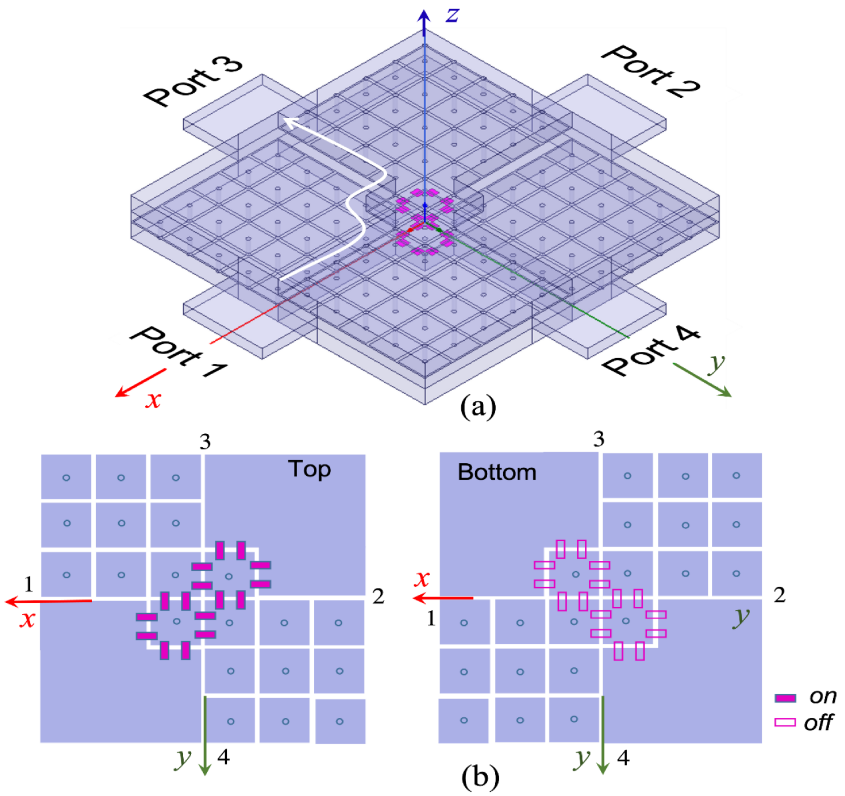

Figure 4.5: (a) Switchable coupler realized by using 2x2 mushroom unit cells in the central part both on the top and the bottom walls; (b) configurations of the pin-diodes with on-off state highlighted

4.7 shows snapshots of the electric field distribution at 29.8 GHz for the structure in Fig.4.4 and for the one in Fig. 4.5(a).

We remark that the difference between the two structures in Fig. 4.6 is not only that the first one (inset of Fig. 4.4) has a larger central area (4x4 cells vs 2x2 cells) but also that in the second one (Fig. 4.5) the PEC in the central area is recreated by connecting diodes across the mushroom elements. In both cases, the signal is delivered from Port 1 to Port 3 with a small coupling factor to Port 2.

The main difference in the scattering parameters is the value of the coupling factor, which is controlled by the dimension of the central part (the larger the central,

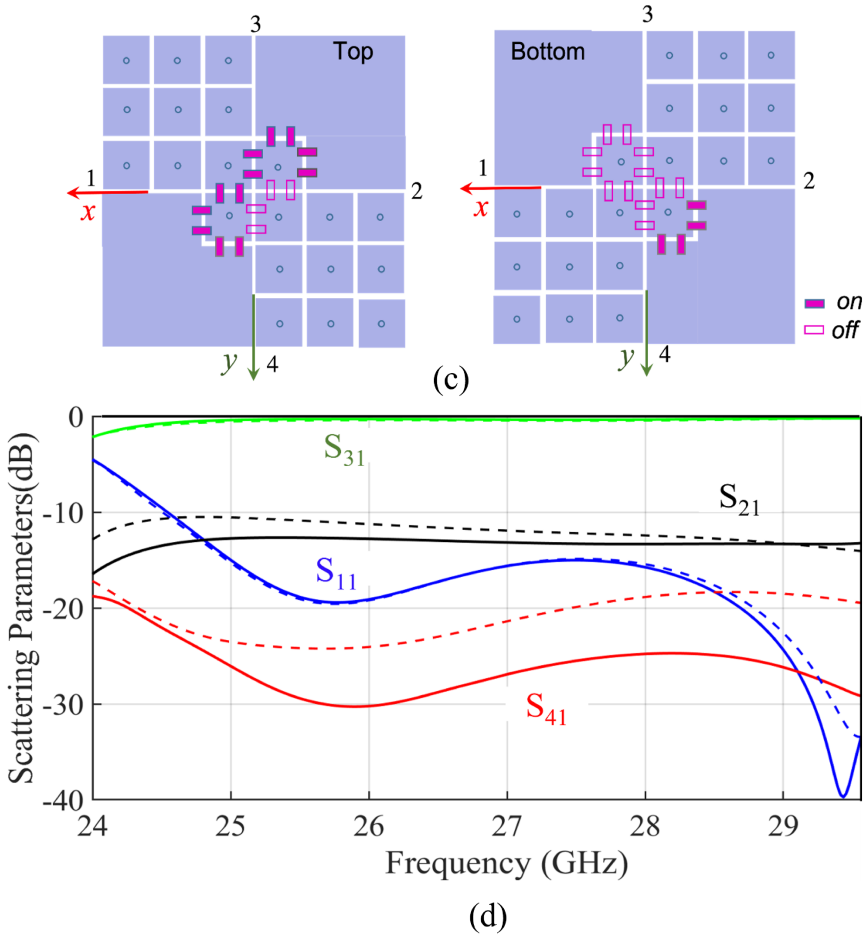

Figure 4.6: (a) configurations of the pin-diodes with different on-off state highlighted (b) Simulated Scattering parameters obtained by using HFSS [1] for the two configurations: Fig. 4.5(b) solid lines (c) dotted lines.The full wave analysis includes the waveguide ports, as shown in Fig. 4.5(a).

the smaller the coupling factor toward port 2).

It is clear by symmetry that switching the state of the diodes re-routes the signal from Port 1 to Port 4 with the same coupling factor to port 2.

Finally, a more realistic model has been considered for the PIN diodes, to assess

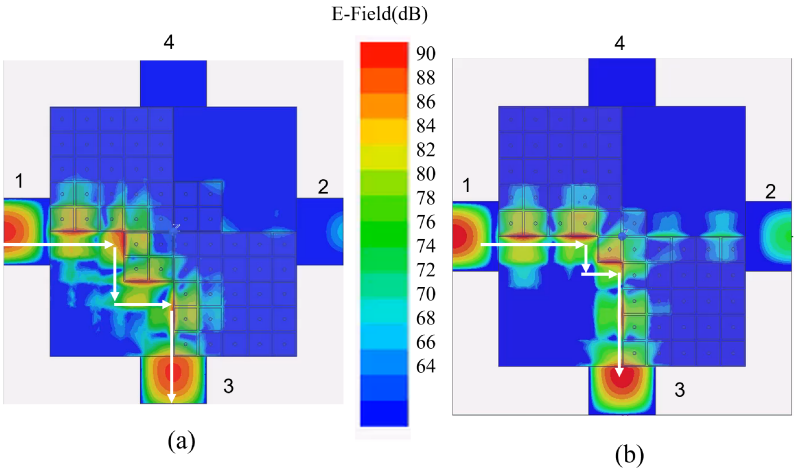

Figure 4.7: Amplitude of the electric field at 29.8 GHz, (a): 4x4 unit cells in the central region (design of Fig.4.4); (b): 2X2 cells in the central region (design of Fig.4.5(b).

the impact of parasitic effects on the device performances. These effects in general depend on PIN diode type and package. Here, we have considered a commercially available surface mount PIN diode (Macom MA4FCP200) able to operate as a Single Pole Single Through switch up to 40 GHz.

In accordance with the information provided in the data sheet [62], we have modelled any forward biased PIN diodes as a 2.8 Ohm resistance and any reverse biased PIN diode as a 20 fF capacitance. The results of the relevant full wave simulations for the configuration in Fig. 4.5b are reported in Fig. 4.8. Simulation results show that parasitic effect cause a small deterioration of the performances, especially in terms of reduced isolation and increased losses but, overall, they do not significantly affect the behavior of the proposed device. This confirm that, with the actual state-of-the-art PIN-diodes, the proposed configuration is feasible up to the Ka-band. It is apparent that non ideality of the switches has a smaller impact at lower frequencies.

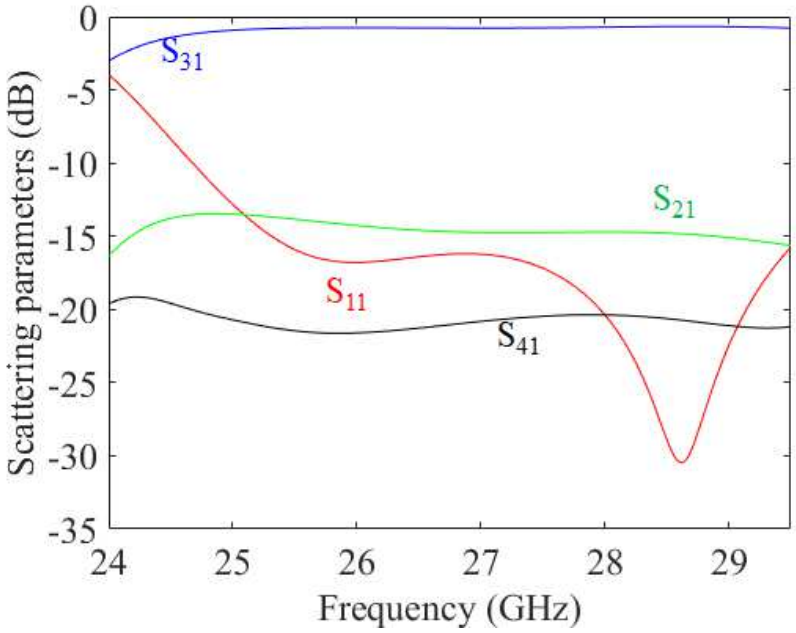

Figure 4.8: Simulated scattering parameters for the structure in Fig. 4.5(b) with a realistic model for the PIN-diodes, accounting for the main parasitic effects.

4.4 Prototyping and measurements

A prototype of the four ports PTD-Symmetric ELC shown in Fig. 4.4 has been realized in PCB technology. Three layers of dielectric materials are glued together by means of two layers of Astra MT77 Prepreg 1035LD of thickness 0.126 mm each. The first dielectric layer is a Rogers RO3003 of thickness 0.762 mm, with a top metallization made by copper of 0.06 mm and a bottom one of 0.05 mm. The third layer is made of the same substrate as the first one. In between these two RO3003 slab layers (used for the realization of the mushroom metasurface) there is a layer of Rogers RT5870, which has relative permittivity $\varepsilon_r = 2.33$ and loss tangent equal to 0.0012. The central part consists of a square region with 3x3 mushroom MTS unit cells on top and a PEC block in the bottom as shown in the layout of Fig. 4.9.

The examples discussed in the previous sections are with RWG feeding. In or-

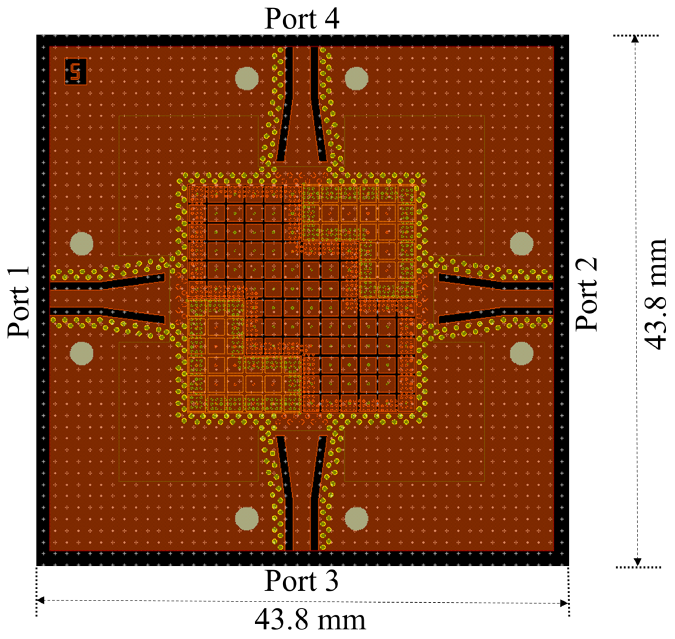

Figure 4.9: Layout of 4-ports PTD-Symmetric ELC by using grounded-coplanar waveguide to a substrate-integrated waveguide transition.

der to realize the structure in PCB technology, with an easy coupling to an SMA connector, we have considered a grounded coplanar input port, complemented by a transition from grounded-coplanar waveguide (G-CPW) to substrate-integrated waveguide (SIW). The strip of the G-CPW is printed at the same level of the mushroom surfaces patches. Taking into account the additional thickness due to the presence of the prepreg, the thickness of the RT5870 was taken equal to 0.254 mm in order to achieve performance similar to the ones obtained without prepreg and a thickness of $d = 0.508$ mm.

The realized prototype is shown in Fig. 4.10. The entire structure with all the feeding transitions has been simulated by a full-wave solver (Ansys HFSS 2020 [1]) and the results for the scattering parameters when power is supplied to port 1 are shown in Fig. 4.11 with continuous lines. The corresponding measured scattering parameters are reported in the same figure with dotted lines. The trend of the measured curves is similar to the one obtained by numerical simulation, with less

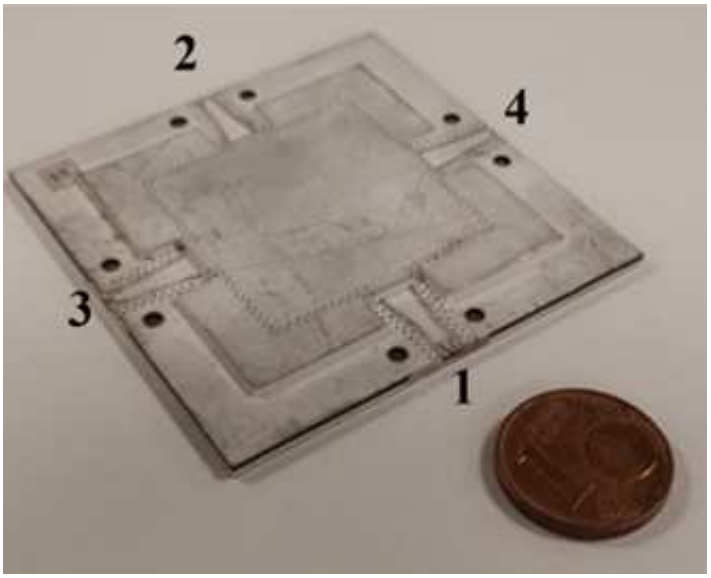

Figure 4.10: Picture of the realized prototype.

satisfactory return loss (around -10 dB) and slightly higher insertion loss, probably due to imperfection in the fabrication.

Measured scattering parameters for excitation at port 2 are reported in Fig. 4.12 Since, the overall structure is PTD-invariant by swapping the vertical axis, Port 1 is connected only with Port 3, and Port 2 only with Port 4. The measured scattering parameters clearly show this symmetry.

4.5 Summary of the chapter

A PTD-invariant edge-line switchable coupler has been presented in this chapter. In the ideal case of PEC and PMC boundary conditions, a couple of ideal synchronized switches at the confluence among the bifilar edge-lines can re-route the signal from one port to another with excellent matching isolation to one port and very small spill-over to another port. This realizes a very good switch over an extremely large bandwidth. Of course, the need to approximate PMC with practical metasurfaces (like mushroom) imposes a certain dimensions to the central switching region. The minimum dimension that one can realize in practice consists of 2x2 mushroom

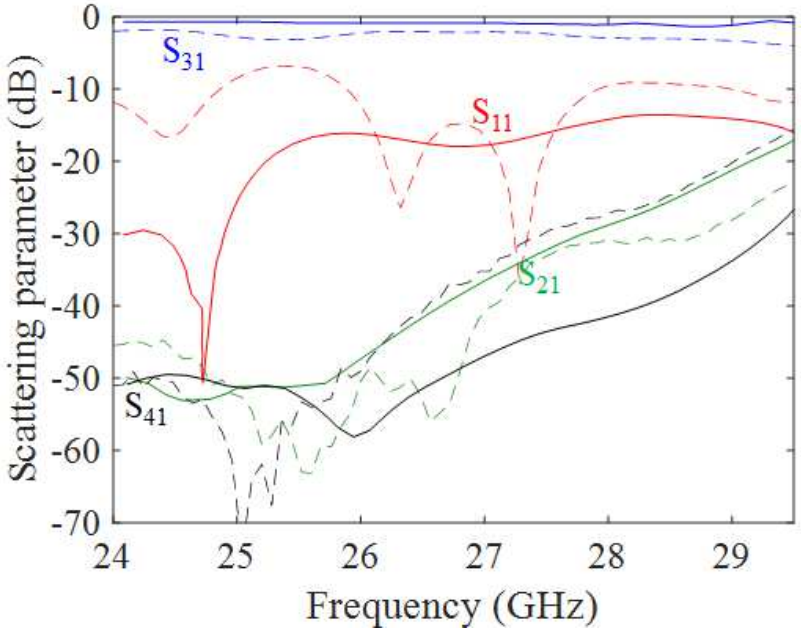

Figure 4.11: Simulated (continuous lines) and measured (dashed lines) scattering parameters of the PTD-Symmetric ELC using grounded-coplanar waveguide substrate-integrated waveguide transition for excitation at Port 1.

cells. It is seen in this case that a combination of switches implies strong coupling to one port, high isolation to the opposite port and a spill-over of power to the front port to a level of -12 dB, thus realizing a large bandwidth switchable coupler. Different combinations of switches can also modulate the power coupled to the front port. If the central region is instead constituted by more cells (e.g., 4x4), the structure emulates better the ideal case, and the spill-over of power to the front port reduces drastically, as predicted by the PTD theory. However, rerouting the signal in this case requires a higher number of switches and a control board. Although the implementation of the device did not include switches, the experimental results have not only demonstrated the applicability of the PTD-symmetry concept, but also opened the path to the fabrication of microwave devices competitive in terms of design flexibility and bandwidth performance.

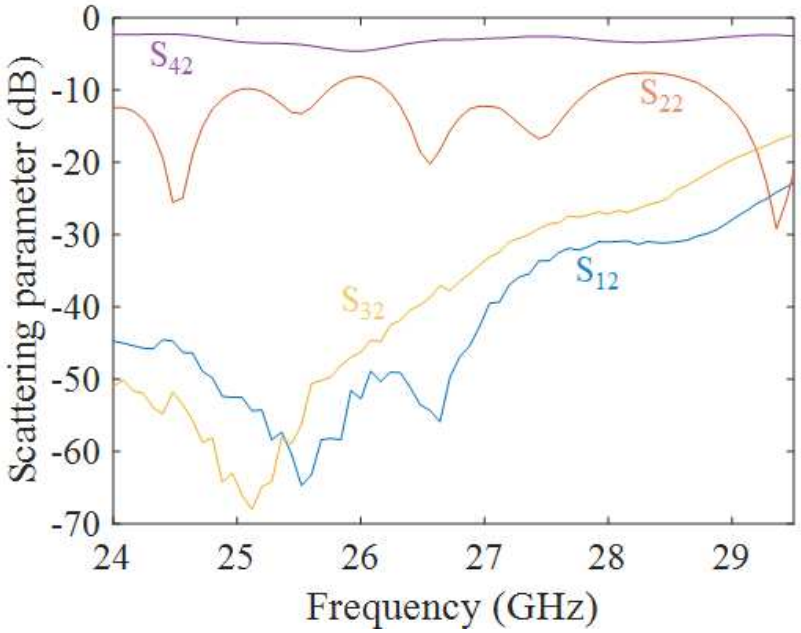

Figure 4.12: Measured scattering parameters of the PTD-Symmetric ELC using grounded-coplanar waveguide substrate-integrated waveguide transition for excitation at Port 2.

Chapter 5

All Metal Bifilar Edge lines

This chapter demonstrates the practical feasibility of using the bed of nails structure to construct a fully metallic parity (P), time-reversal (T), duality (D) symmetric bifilar edge waveguide. The waveguide design starts by considering first the ideal perfect electric condition (PEC) and perfect magnetic condition (PMC) based parallel plate waveguides (PPW). Then, metallic pillars (Pins) are used to emulate the PMC boundary conditions. Three different kinds of PTD-symmetric unit cells of PEC-pillar PPW are considered initially. The first case has the pillars aligned on top and bottom walls, while in the second case the pillars in the upper wall are shifted in glide manner along the propagation direction with respect to the ones in the lower plate. Finally, in the third case, the pillars in the upper right wall are shifted in glide manner also along the direction orthogonal to propagation. Numerical results show the backscattering protection and the ability to confine the EM field in the proximity of the edge between complementary boundary over a large bandwidth. [1]

[1]This work was conducted while the author was a visiting Ph.D. student at University Carlos III, Madrid (Spain), from May to August 2022 (working with. Prof. Eva Rajo). Some part of the work is submitted in upcoming EuCAP 2023 conference Florence (Italy).

5.1 Introduction

Metallic waveguides are one of the earliest types of guiding structures implemented by electromagnetic engineers. They have been broadly employed since they have low losses and no leakage. Additionally, they can handle high power and have cross-talk free characteristics. As we know that by using reciprocal structures parity (P) time-reversal (T) duality (D) symmetry [3], [14] is achieved. The practical realization of PEC-PMC bifilar edge Waveguides requires the implementation of a high impedance metasurface [38], to mimic PMC boundary condition. However, the selection of the periodic structure that provides the PMC boundary condition affects the losses of the waveguide. In order to overcome these limitations metallic gap waveguides as discussed in [63], [64], [65] are considered. In metallic gap waveguide technology, the waves are guided in air, reducing the losses with respect to artificial metasurfaces [66]. Additionally, these structures do not require metallic contacts between upper and lower plates, which is a relevant advantage in manufacturing process, and they can be used in packaging to minimize radiation losses, unwanted coupling, and resonant mode influence [67]. Metallic Pin type artificial materials [68] has been commonly used in gap waveguide technology to block propagation of wave in undesired areas [69], [70]. Holly structures in gap waveguide technology has valuable properties at high frequencies, it provides the cost effective manufacturing of the designs.

5.2 PEC-Pillars Unit Cell

Consider the transverse cross-section of the canonical PTD-symmetric bifilar edge waveguide (PTD-BEW) which consists of the parallel plate structure shown in Fig. 5.1(a). When the two plates are separated by a distance $d < \lambda/4$, the structure supports only an edge mode, whose electric field distribution is sketched in the $XY - plane$. The field is exponentially attenuated on both sides $x > 0$ and $x < 0$ with a penetration depth (inverse of the attenuation constant) approximately equal to the separation distance between the plates, d. Since the field is confined between the two edge lines, the structure resembles a bifilar transmission line. This structure is PTD-symmetric with respect to the reflection along the y axis, since this operation makes the BCs dual, as illustrated in Fig. 5.1(b).

The inset of Fig. 5.2 shows the basic unit cell used to implement the PTD-BEW, which is analogous to the one used in [2]. It consists of two parallel plates each of which composed by a PEC block of thickness $Pil_{Length} = 4.42mm$ and metallic

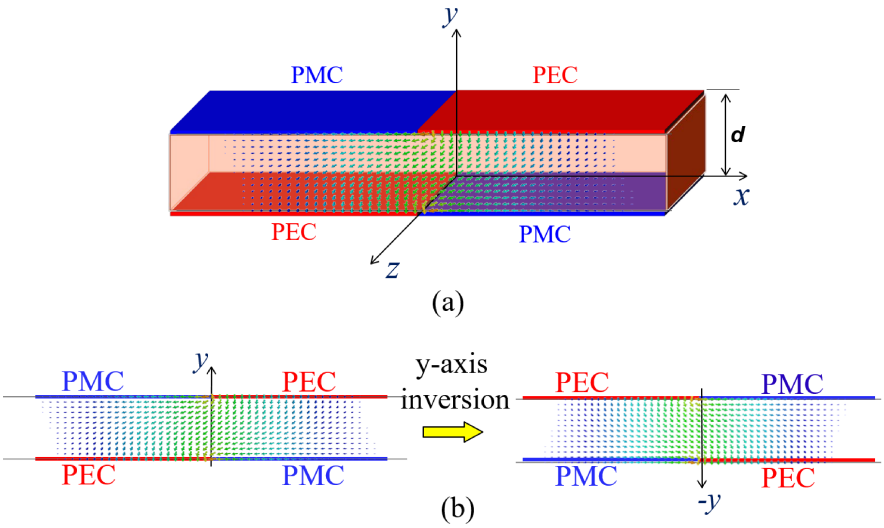

Figure 5.1: *(a)* Ideal BEW constituted by alternating PEC/PMC BCs *(b)* graphical illustration of the PTD symmetry concept.

pillars, or pins, emulating the PMC wall. The unit cell size for the pins is $P = 3.2\,mm$, while the pin width is $Pil_{width} = 1.6\,mm$. The air gap between the top and bottom PEC-Pillars based parallel plates is $h_{air} = 0.5\,mm$. Finally, $L_y = 9.34\,mm$ and $L_x = 32\,mm$. The dispersion diagram of this unit cell is shown in Fig. 5.2. The red line is associated with the bifilar edge mode, while the dashed black line is the light line in the air (the medium filling the space between upper and lower plate of the PPW). Since the mode supported by the ideal PEC-Pillars is TEM, we can assume that the frequency at which the pillars better emulate the PMC is the one where the air light line crosses the dispersion curve of the bifilar edge mode, i.e. around $f = 27.8\,GHz$. In this case, the unimodal bandwidth ranges from 16.56 GHz (the cutoff frequency of the edge mode) to 29.57 GHz (the cutoff frequency of the higher order mode). However, the above mentioned crossing point is too close to the cutoff frequency of the higher order mode to allow wideband operation.

Hence, the concept of glide symmetry [71], [72] is explored to increase the propagation region which is protected from backscatter. The inset of Fig. 5.3 shows the unit cell geometry of a second structure, where the upper metallic pillars are glide shifted along the $z-axis$ by the amount $P/2$. The dimensions of the unit cell

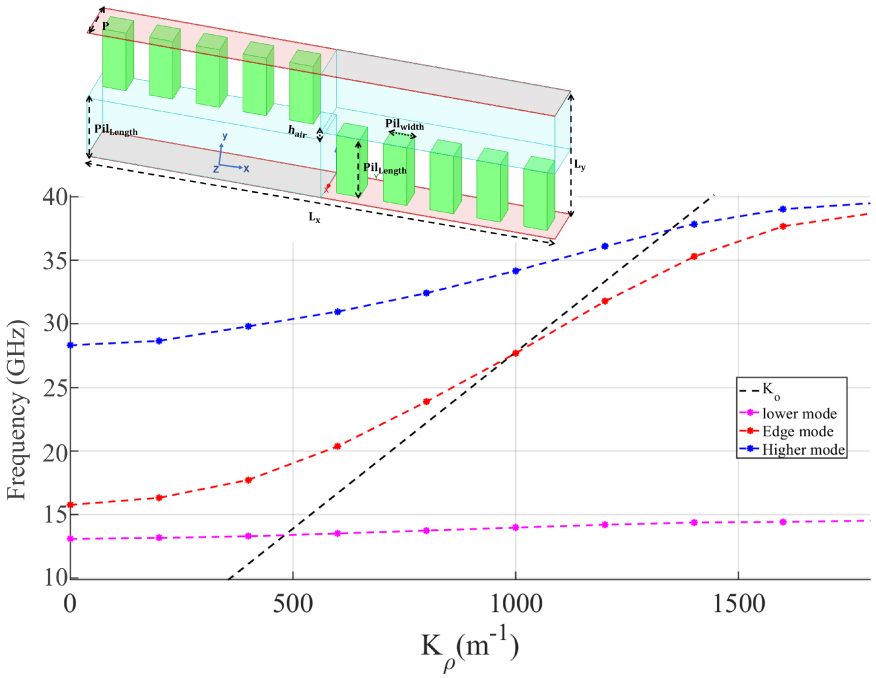

Figure 5.2: PEC-Pillars based PTD symmetric unit cell and corresponding dispersion diagram.

are the same as in Fig. 5.2. The air gap between PEC-Pillars based parallel plates is h_{air}= 0.5 mm, while the period is P = 3.2 mm.

The dispersion diagram of this unit cell is given in Fig. 5.3. The red line is associated with the bifilar edge mode while the dashed black line is the light line in the air. In this case, the air light line crosses the dispersion curve of the bifilar edge mode around $f = 27.5$ GHz. The unimodal band ranges from 15.3 GHz to 28 GHz. This also yields the same situation where the frequency of quasi-TEM mode behaviour is too close to the cutoff of the higher order mode.

To improve this, now the glide shifting [73], [74] is applied both along the z and the x directions with a period P/2. The resulting geometry is shown in the inset of Fig. 5.4. The dimensions of the cells are Pil_{width} = 1.6 mm and Pil_{Length} = 3.3 mm. The air gap between PEC-Pillars based parallel plates is h_{air}= 0.5 mm, while the period is P = 3.2 mm, and L_y = 7.1 mm and L_x = 32 mm. The dispersion diagram shows that the unimodal bandwidth ranges from 18.26 GHz to 36.57 GHz,

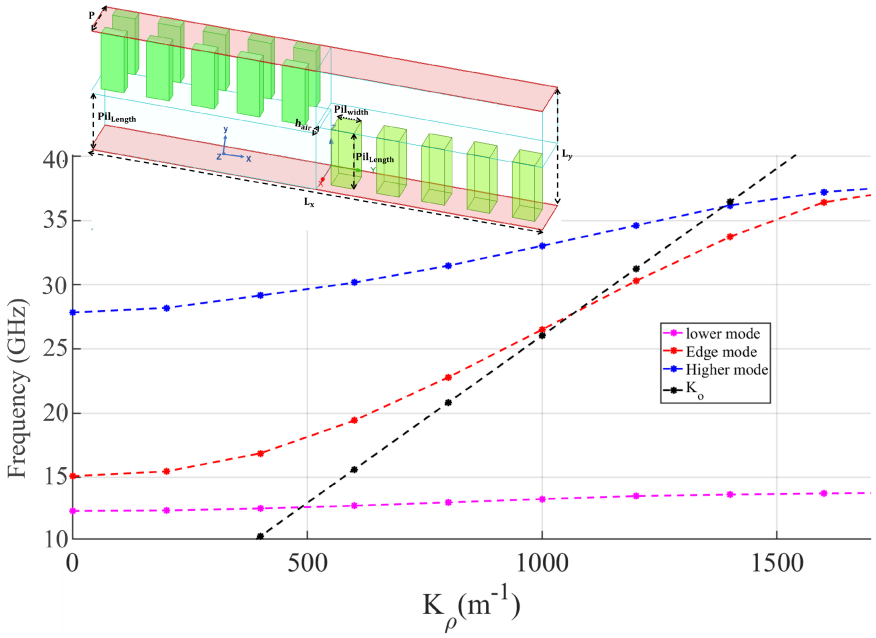

Figure 5.3: PEC-Pillars based unit cell with glide-Symmetry along z and its dispersion analysis.

corresponding to a percent bandwidth of approximately 67%. Furthermore, the percentage bandwidth in which the structure is expected to approach ideal behaviour is around 40%.

It is quite visible that by using the glide arrangement of the pillars along two directions (x and z), we can achieve a larger unimodal band, and a less bulky structure can be obtained since the dimension L_y, which corresponds to the height of the pillars, is reduced from $9.34\,mm$ to $7.1\,mm$. This means that the bandwidth can be increased even for lower values of the dimensions.

5.3 Basic PEC-Pillars BEL Structures

The PTD-symmetric unit cell with the glide arrangement of the pillars along two directions is considered for further investigation.

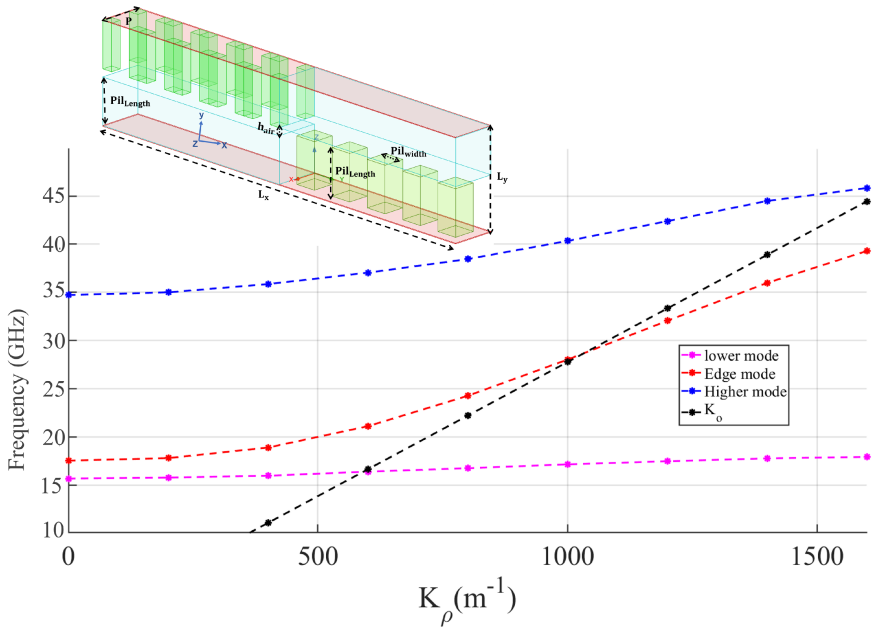

Figure 5.4: PEC-Pillars based unit cell with glide-Symmetry along x and z and relevant dispersion diagram.

5.3.1 Straight PTD-BEL

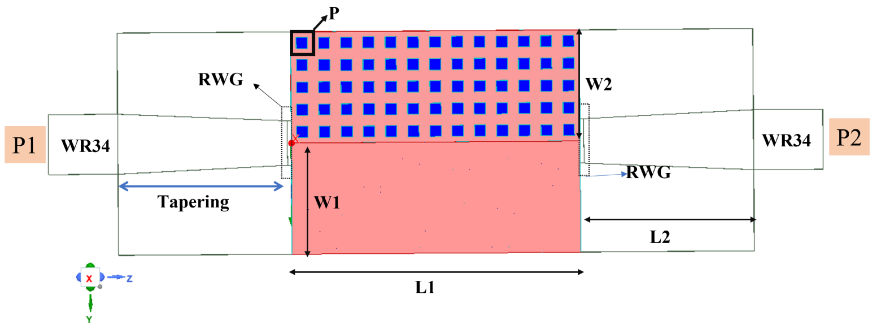

Figure 5.5: PTD-symmetric bifilar edge line based on the unit cell given in Fig.5.4.

Fig. 5.5 shows a branch of the PTD-symmetric bifilar edge WG and the relevant

feeding structure. The length of the BEW is $L1 = 41.6\,mm$, while the length of the feeding part is $L2 = 25\,mm$. Each PMC wall consists of the arrangement of 65 pillars on the top side and 65 on the bottom side. A feed structure is required at both ends of the bifilar edge WG to excite a quasi-TEM mode. Therefore, two rectangular waveguides (RWGs) have been introduced and optimized to form the two ports of the guiding structure. The height of the RWGs has been set equal to the distance between the bifilar edge WG walls (i.e. $0.5\,mm$), while their width has been optimized using a parametric study performed in $HFSS^{©}$.

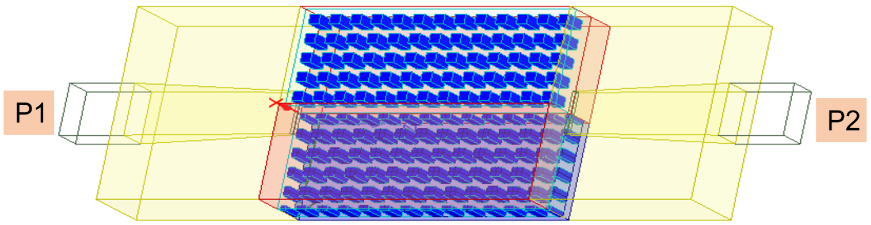

Figure 5.6: 3 dimensional view of the PEC Pillars bifilar edge line.

Fig. 5.6 shows the different prospective of the bifilar edge waveguide.

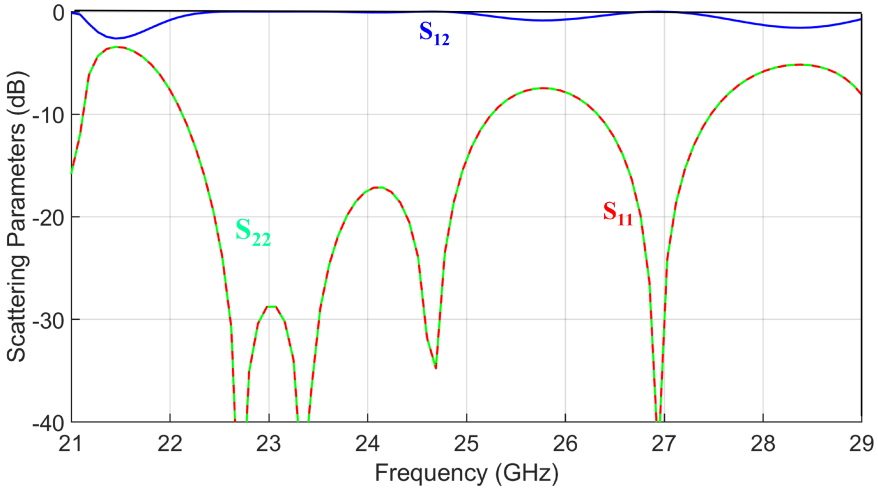

Figure 5.7: Simulated Reflection and Transmission coefficients for the structure of Fig. 5.5.

Since the RWG obtained dimensions are not standard, a tapered transition to a standard WR34 (waveguide for mmwave) is introduced.

The scattering parameters are shown in Fig. 5.7. It is found that the reflection coefficient (dB) is below -8 dB in all the frequency range between 22 GHz and 28 GHz, while the transmission coefficient is close to zero over the same band.

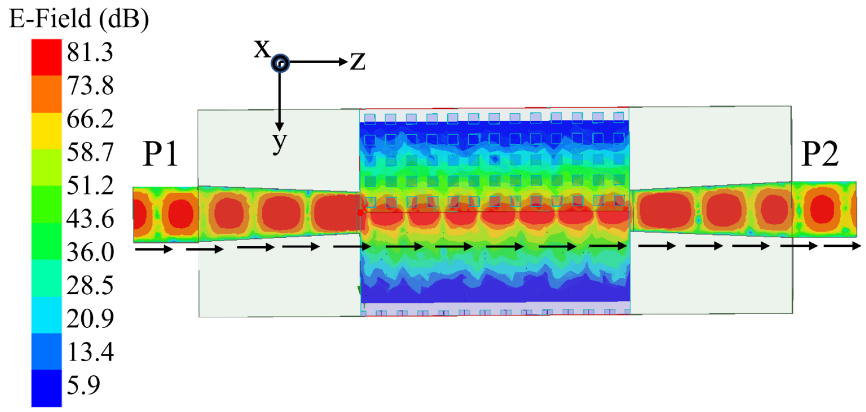

Figure 5.8: Amplitude of E-field at the frequency of 24 GHz.

Notice that this reflection coefficient includes the effects of the four transitions, WR34-to-non standard RWG, non standard RWG-to-BEW, BEW to non standard RWG and non standard RWG to WR34. Hence, the matching of the PTD edge WG is quite satisfactory. The electric field distribution at $f = 24\ GHz$ in the transverse plane in the middle of the edge waveguide is shown in Fig. 5.8. The field, excited at one port, is highly confined close to the junction of PEC-Pillars.

5.3.2 Segmented PTD-BEL

In this section, we study the field propagation in the bent PTD-Symmetric BEW shown in Fig. 5.9. The dimensions of the edge line are the same as described in the previous section. This particular case is used to estimate the effect of repeated 90° bending discontinuities on the propagation line.

Fig. 5.11 shows the simulated reflection coefficient. It can be seen that it is below -10 dB in the frequency range between 21.5 to 26 GHz. Fig. 5.11 presents the

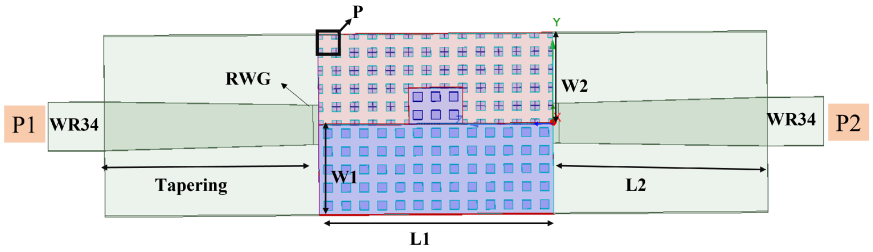

Figure 5.9: Bent PTD-symmetric bifilar edge line based on the unit cell given in Fig. 5.4.

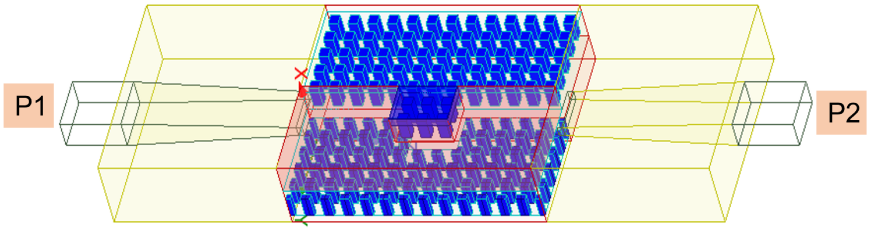

Figure 5.10: 3 dimensional representation of the edge line with bent.

electric field map on a plane located in the middle of the gap between the PEC/Pillars walls.

It is seen that the propagation is protected over the entire path, with a low reflection coefficient at the input port over the entire bandwidth. It turns out that the electric field is strongly confined close to the edge also at the line discontinuity, with no diffraction losses.

5.4 Detailed Prototype

In order to make proposed structure manufacturing friendly the prototype should be design in two pieces. When joined together with screws to reduce manufacturing costs. It will be discussed in this sections.

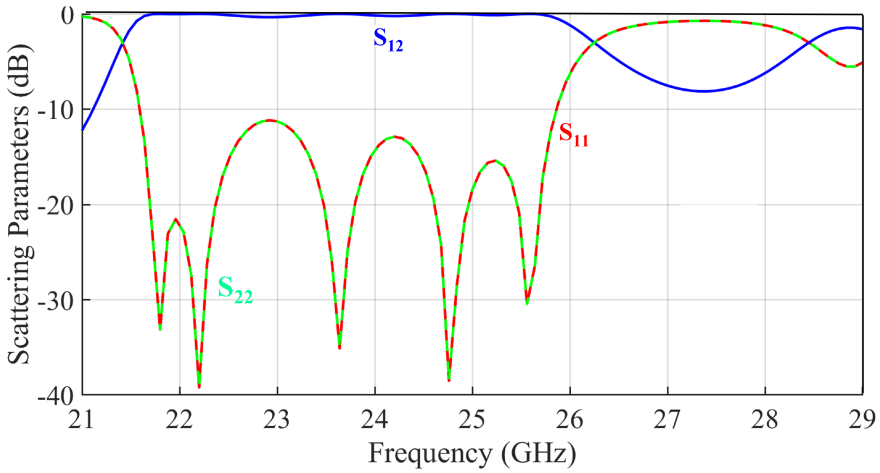

Figure 5.11: Simulated Reflection and Transmission coefficients (dB) for the PTD-BEL with bents.

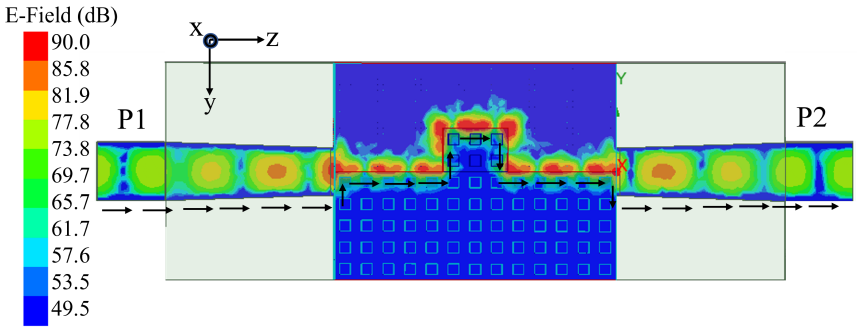

Figure 5.12: Amplitude of E-field inside the bent PTD-BEL at 24 GHz

5.4.1 Holey glide symmetric Structure

A sketch 2D glide operators [72], [75], together with the corresponding PPW unit cells, is given in Fig. 5.13(a). In the 2D case, the minimum unit cell is positioned in the diagonal direction. we will keep the notation of periodicity in the x- and y-directions, i.e., P_x and P_y and d = $\sqrt{2}\times P_x$ as shown Fig. 5.13(b). Since, the bandwidth of the bandgap has inverse relation with the gap so, we have used the g = 0.25 mm between upper and lower part of the PPW.

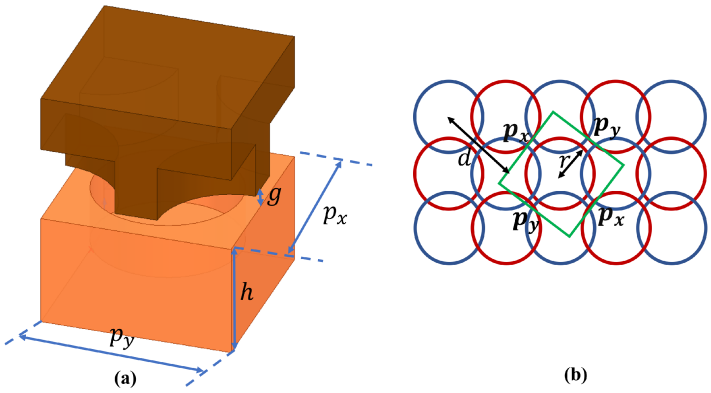

Figure 5.13: (a) Sketch of periodic unit cell of 2D glide symmetric PPW structure, (b) Sketch of 2D glide symmetric structure red and blue circles denote holes at the top and bottom plates of parallel-plate waveguide (PPW).

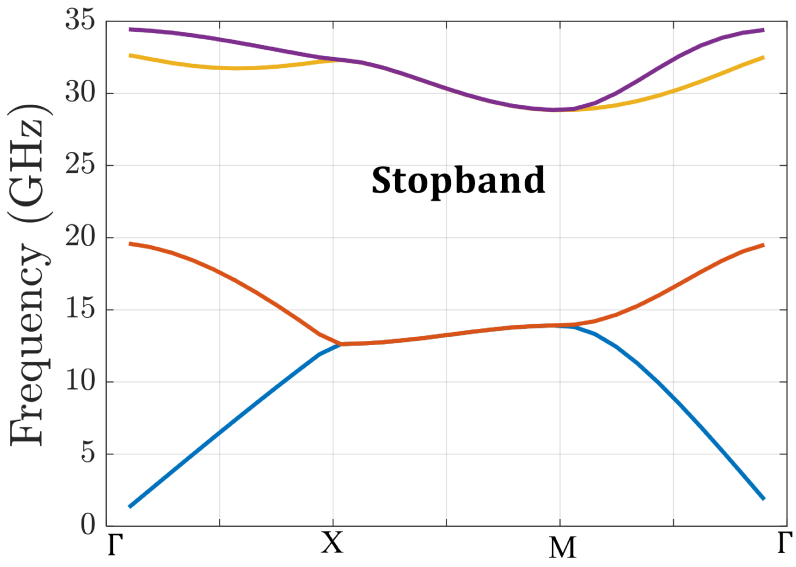

Figure 5.14: Dispersion diagram of the 2D glide symmetric structures obtained using CST Microwave Studio.

This unit cell geometry reflects the corresponding dispersion diagrams, we considered glide symmetric periodic structures with the stop-band in the Ka-band. Without loss of generality we fixed the diameter and the depth of the holes (2r = 7 mm and h = 3 mm, respectively). We used the period that maximizes the bandgap, and thus the $\sqrt{2}\times P_x$ = 12.7 mm for the 2D periodic structure. Fig. 5.14 presents the dispersion diagrams and attained stop-band with the implemented dimensions goes from 18 GHz to 30 GHz. These dimensions will be employed in feeding section of the design to make manufacturing convenient.

5.4.2 Bended line Holey glide symmetric PTD Structure

The layout of a segmented PTD-BEL structure is presented in Fig. 5.15. The path is constituted by a single square meander, with four 90° bends.

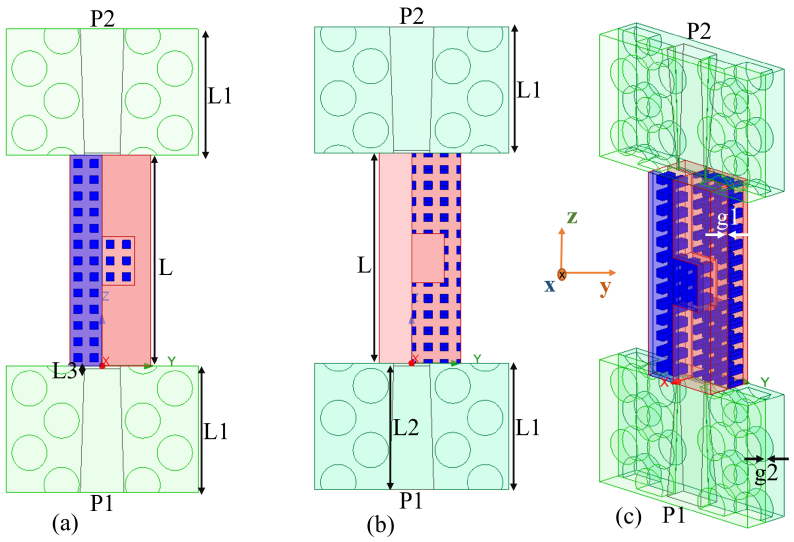

Figure 5.15: PTD-symmetric bifilar edge line with multiple 90° bends (a) Top view, (b) Bottom view, (c) 3 dimensional view.

This layout is analogous to the one given as an example in Fig. 5.9 and it is used to test the robustness of the propagation against discontinuities in the path. The only significant difference is the PTD-BEL used in Fig. 5.9 is with solid PEC block with transition in the form of tapering inside that is referred as ideal transition. While

in Fig. 5.15 two layers of holey glide symmetric [76] withe the aim to provide two advantages: (a) provide the ability to divide structure into two parts namely top layer and bottom layer, (b) block the energy leakage from the sides along y-axis. The considered dimensions in Fig. 5.15(a) and (b) are L = 41.6 mm, L1 = 25 mm, L2 = 24.5 mm and L3 = 0.5 mm. While the g1 and g2 highlighted in Fig. 5.15(c) are 0.55 mm and 0.02 mm respectively. The commercial available WR34 waveguide has been used for excitation where ports P1 and P2 are indicated.

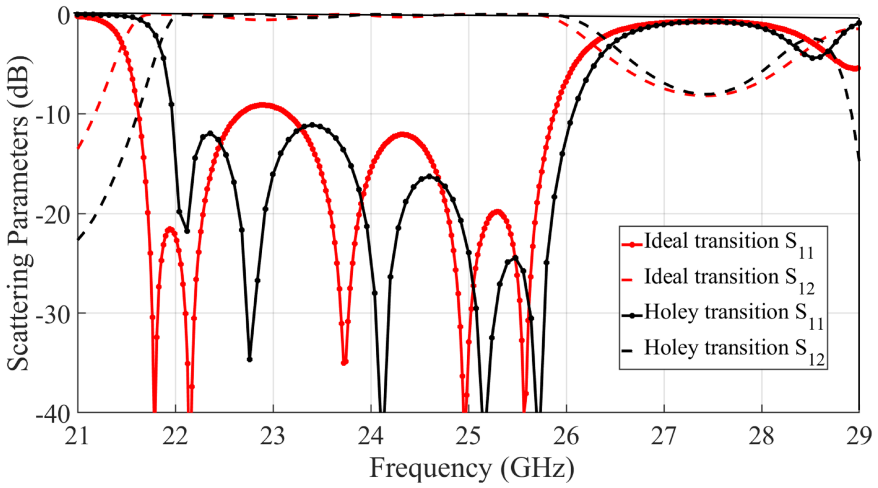

Figure 5.16: Simulated refection coefficients of PTD-BEL shown in Fig. 5.9 (ideal transition) and Fig. 5.15 (holey structure transition) respectively.

The simulated scattering coefficients are shown in Fig. 5.16 by using commercial available *HFSS*©v22 [1]. Despite the abrupt discontinuities provided by the four right-angle bends, the transition with holey structure provides the same level of matching seen for the ideal transition (around -10 dB in the range from 22 to 26 GHz) with 0.02 dB of insertion loss. It is wort noting that these results also include the effect of the two transitions to RWG, which is the major cause of reflections.

A snapshot of the electric field in the longitudinal cross section can be seen in Fig. 5.17. We observe that the field is properly confined at the edge throughout the entire path and the propagation follows the bends.

Fig. 5.18 shows the possible layout which will be used for the practical Realization of glide-symmetric Holey transition with PTD-BEL. The manufacturing

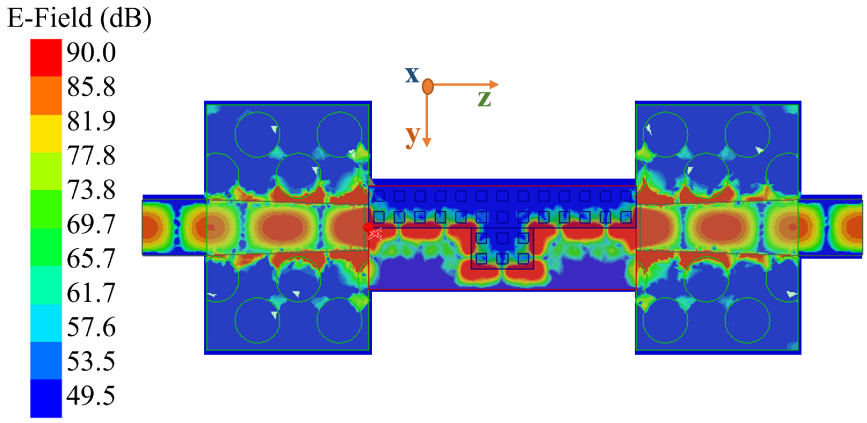

Figure 5.17: Amplitude of the electric field in the central gap of PTD-BEL.

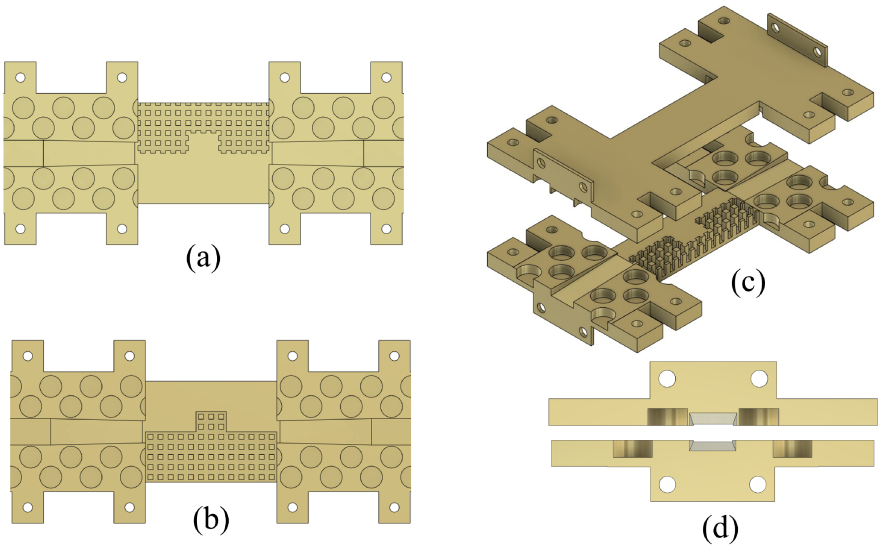

Figure 5.18: Possible layout of PTD-BEL with standard metallic WR34 flange (a) Top Layer, (b) Bottom Layer, (c) 3-Dimensional View, (d) Front view.

process of this layout is still in process.

5.5 Summary of the chapter

The performance of a PTD-symmetric bifilar edge line based on metallic pillars has been analyzed here. Inspired by the ideal PTD-symmetric structure consisting of PEC-PMC boundary conditions, the proposed structure consists of a combination of conducting plates and metallic pillars, arranged so as to exhibit PTD-symmetry in all aspects. It is found that using the glide arrangement of the pillars along two directions gives a larger unimodal bandwidth. Numerical results show that the input reflection coefficient of this guiding structure is very good over a wide bandwidth, even in presence of 90° bends. Consequently, the practical feasibility of a unidirectional all-metal structure in the range between 23-29 GHz has been demonstrated. The fabrication of the feeding by using holly structure is under progress. It is also possible to design a four port junction. In which one port of the coupler and rest of the ports could be decoupled. However, adding the reconfigurabilty in this case is not very straight forward.

Chapter 6

PTD Symmetric TEM square Waveguides

In this chapter the transmission and reflection characteristics of a bent square TEM waveguide constituted by two opposite perfect electric conductor and perfect magnetic conductor walls are analyzed. This waveguide exhibits a parity time-reversal duality (PTD) symmetry with respect to both the diagonal axes. It is found that this property is maintained even when the structure is bent in a plane orthogonal to one of the two PTD symmetry axes (PTD-bend). As a consequence, the TEM mode propagation is protected against backscattering by this class of discontinuities. The preservation of the PTD symmetry with respect to a geometrical flexibility of the bend is also analyzed, thus introducing a new class of bendable waveguides largely immune from backscattering by bend discontinuities. Two dual-polarized arrays have been considered. The first one is constituted by a square waveguide which has perfect electric conducting (PEC) and perfect magnetic conducting (PMC) BC on opposite walls, and open ended in free-space with side by side element rotated by 90°*. The second arrays, we refer to say as checkerboard, is constituted by the same elements but disposed in a diamond shape, with square patches of PEC and PMC BC imposed on the free-space interface in the complementary spaces w.r.t the open ended waveguide terminations. This gives contiguous open*

ended waveguides rotated of 90° *to get dual polarization. Both these array structure exhibits PTD-symmetry along two diagonal axis. It is also shown here that these arrays exhibits wide angle (*0° - $\pm 80^\circ$*) active impedance matching over a large bandwidth together with a good isolation between the cross-polarized ports.* [1]

6.1 Introduction

Planar radiating waveguide arrays are typically used both as direct radiating arrays [78] and dense focal planar array in reflector antennas [79]. Wide band impedance matching and low mutual coupling, togather with reduced size, constitute the major requirements in waveguide array design. To this aim complex cross-section waveguide has been presented through cross-sectional folding and bending. Some examples are π (or rigid), H-waveguide and N-guides [80], [81]. Here, PTD symmetric theory has been used to design a simple cross-sectional waveguide. It has capability of propagation a dominant TEM mode whose field distribution is similar to that described in [20], [2] and also in the conventional dielectric loaded hard wall rectangular waveguide [80], [82], [83]. PTD symmetric theory reveals that if an axis exists in transverse cross-section of a guiding structure then its inversion produce dual boundary conditions (BC) with respect to the original BC $(x,y,z) \rightarrow (x,y,-z)$, [shown in Figure 6.1] this structure supports a propagation immune from backscattering [20]. Therefore, the resultant propagation is robust (i.e., it does not produce any backscattering) against any defect that respect a PTD symmetry w.r.t the same axis. Hence, an array of open-ended square PTD-symmetric waveguides has been investigated in [28, 29]. This array with an ideal BCs fulfills the PTD-symmetry, and it also allows wide angle beam scanning with good matching performance.

6.2 Square TEM waveguide

The geometrical configuration of a square TEM waveguide, PTD-symmetric with respect to both the diagonal axes, is reported in the inset of Figure 6.2. This waveguide can be realized by using printed metasurfaces on two opposite walls [80] to mimic the PMC boundary conditions. It is well known that the ideal structure supports a TEM mode, namely a mode without cut-off [80]. However, in its practical

[1] Few part of the work presented in this chapter has been published as "Flexible Unidirectional PTD-Symmetric Waveguide" in *URSI Radio Science Letters,vol. 3, p. 51 2021*, [77] and rest is submitted to IEEE Antennas and Wireless Propagation Letters (AWPL).

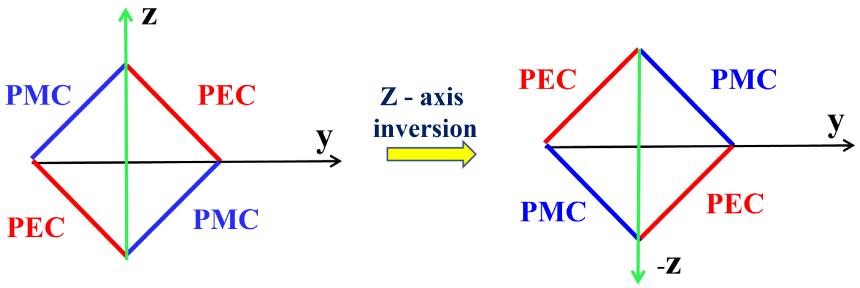

Figure 6.1: Basic illustration of PTD-symmetric TEM waveguide (Z-axis is the parity axis).

implementation with metasurfaces, the supported mode does not have a zero-cut-off frequency and it only exists in a certain bandwidth around the frequency where the metasurface exhibits an equivalent PMC behavior. A basic PTD symmetric waveguide straight section has been designed and analyzed using HFSS commercial software. The length of each wall is $L = \frac{\lambda}{4}$ at $f_0 = 7$ GHz, $W = 0.5$ mm while the overall length of the waveguide along the propagation axis is $H = \lambda$.

Two cases have been analyzed. In a first case, two ideal ports (with the configuration of the TEM mode) have been set at the two end points, and the transmission (dashed-red line) and reflection (red continuous line) coefficients have been calculated. The simulated reflection coefficient at the waveguide port is below -35 dB while the transmission coefficient is close to 0dB. This first example has not a practical relevance except that it calibrates the level of numerical noise in modeling the structure with HFSS ports. In the second example, the waveguide is open ended into free space and only one ideal port is applied at one side. The PEC and PMC boundary conditions have been applied in HFSS even to the external side of the walls. It is seen that the level of reflection coefficient (blue line) is quite low for all the considered frequencies. The reason of this good matching is in the fact that the free space is a particular type of PTD-symmetric medium, and therefore the discontinuity introduced by the termination is PTD-symmetry compliant.

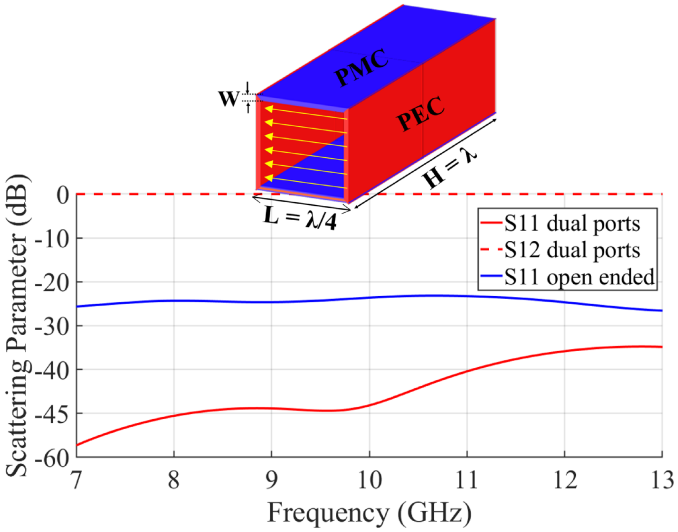

Figure 6.2: Amplitude of the reflection and transmission coefficients vs. frequency for a straight section of PTD symmetric square waveguide calculated by HFSS. Red lines: dual port configuration; blue line: reflection coefficient of the waveguide terminated into free space.

6.3 Reflection properties of 90° bend discontinuities

Let us consider first the waveguide cross-section in Fig. 6.3 where $z-$ axis is the PTD symmetry axis. This means that changing z in $-z$ makes the boundary conditions dual. The cross section can be square (left hand side of Fig. 6.3) or rhombic (right hand side), while maintaining the PTD- symmetry property valid.

In order to assess the impact of the PTD-theory on the reflection properties of a bend, we have considered two types of right-angle bend for a PTD-symmetric TEM waveguide. For simplicity, we will consider first the square cross section. In the first configuration the bend is made in the plane orthogonal to the parity axis. i.e. connecting two straight sections of square cross section with propagation axis in the xy-plane. This geometry fulfils overall the PTD symmetry property and therefore we denote it as PTD-bend. In the second configuration the bend is made around one of the two PEC wall. The two bent sections now share the two planes on which the PMC walls lie. We denote it as non PTD-bend. A PTD-bend in square TEM-waveguide is shown in the inset of Fig. 6.4. In the same figure both reflection

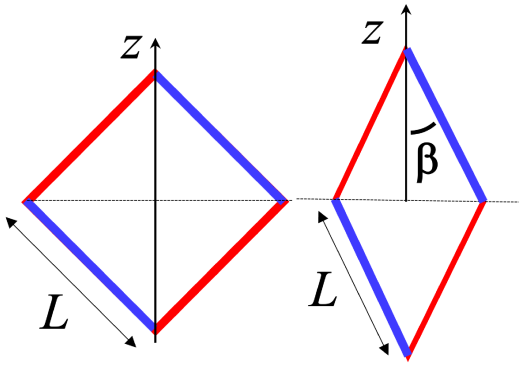

Figure 6.3: Cross-section geometry of the square and rhombic waveguide with the same side length. PMC-walls are represented in blue and PEC-walls in red.

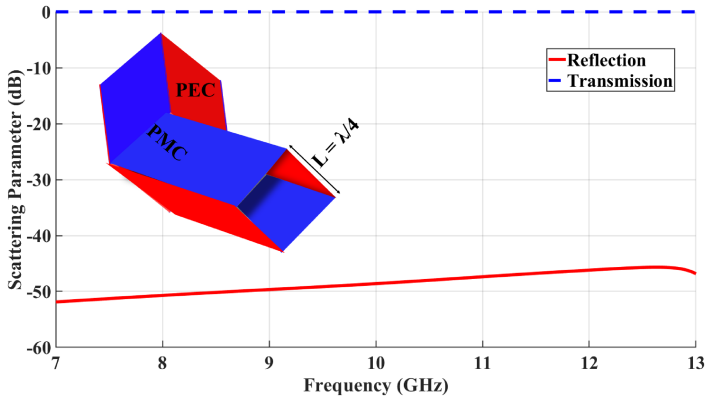

Figure 6.4: Simulated reflection coefficients of PTD symmetric waveguide with PTD-bend.

and transmission coefficients are shown. It is found that the reflection coefficient is below -50 dB in the frequency range between $7 \div 13$ GHz. This means that the structure presents a complete transmission, with no reflection inside the waveguide at the bend discontinuity. A snapshot of the electric field distribution at 11 GHz on the plane shared by the two sections is shown in Fig. 6.5. The electric field excited at one port clearly follows the path between the PMC-PEC walls, and the

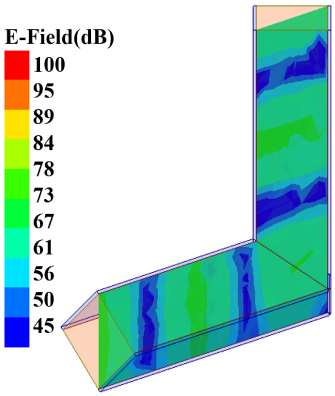

Figure 6.5: Snapshot of E-Field inside the PTD-symmetric waveguide with PTD-bend.

distortion due to the bend does not give rise to reflected field at the cross-section discontinuity.

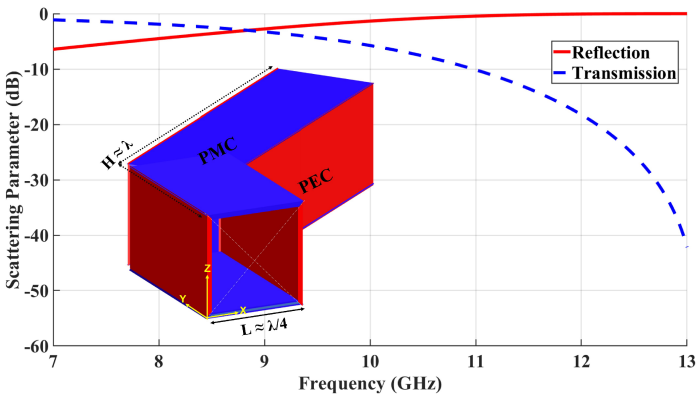

Figure 6.6: Simulated reflection coefficients of PTD-symmetric waveguide with NonPTD-bend.

A non PTD-bend in square TEM-waveguide is shown in the inset of Fig. 6.6.The bend in this case breaks the PTD-symmetry, and this affects the scattering parameters also reported in the same figure. The reflection coefficient is around -5 dB at $f = 7$ GHz and gradually increases up to almost 0 dB at $f = 13$ GHz. As a con-

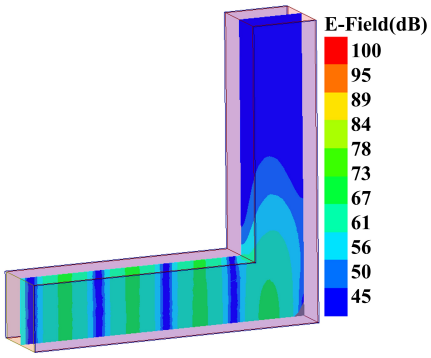

Figure 6.7: Snapshot of E-Field inside the PTD-symmetric waveguide with non PTD-bend.

sequence, on the same frequency range the transmission coefficient decrease from -1 dB till -40 dB. This clearly shows that the field is mostly reflected back at the bent discontinuity. A snapshot of the electric field distribution at $f = 11$ GHz on the plane orthogonal to the PEC walls is reported in Fig. 6.7. It is found that the field excited at one port does not reach the other port, due to the strong reflection at the right-angle bend.

6.3.1 Flexible TEM Square waveguide

A PTD-symmetric bent TEM-waveguide, with an arbitrary bend angle, exhibits an interesting geometrical (and mechanical) property: starting with an initial bent configuration with a square cross-section, the bending angle can be increased continuously changing the cross-section from square to rhombus without breaking the PTD-symmetry of the resulting waveguide. This realizes a flexible PTD-symmetric waveguide. Let us consider the right-angle PTD-symmetric bent waveguide shown in the left hand side of Fig. 6.8, which is the same as that in Fig. 6.8. Let us denote with β the half-angle between PEC and PMC walls across the PTD-axis (z-axis). Moreover, let us denote with α the half-angle between the symmetry axes of the two straight waveguide sections, i.e. x-axis and η-axis in Fig. 6.8. The flexibility of the PTD-symmetric waveguide is implemented by varying β between 45° and 0°. The following relationship holds between the distance $|P_1P_2|$ between the two points P_1 and P_2 and the two angles α and β:

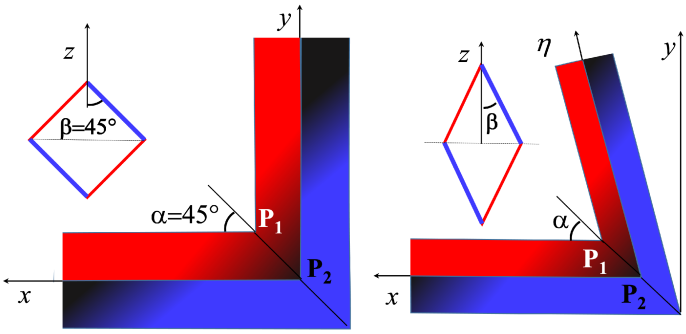

Figure 6.8: Flexible PTD-symmetric waveguide and geometrical parameters.

$$P_1 = (L\sin\beta\cot\alpha, 0, L\sin\beta); \tag{6.1}$$

$$P_2 = (0, L\cos\beta, 0); \tag{6.2}$$

$$|P_1 - P_2| = L\sqrt{1+\sin^2\beta\cot^2\alpha} \tag{6.3}$$

Since the distance $|P_1 - P_2|$ has to remain constant during the folding operation, in order to ensure that the structure is mechanically realizable, the quantity $\sin\beta\cot\alpha$ must also remain constant. Its value is found by imposing one desired angle combination, e.g. $\alpha = \beta = \pi/4$ (square waveguide cross section for a 90° bend) gives $|P_1P_2| = L\sqrt{3/2}$, i.e., $\sin\beta\cot\alpha = L/\sqrt{2}$.

Fig. 6.9 shows some examples of geometry variations for different value of β. It is worth noting that, starting with a square cross-section for a 90° bend, the cross-section becomes rhombic in the folding operation. Fig. 6.10 reports the simulated reflection and transmission parameters for different values of β. For all the considered values the transmission coefficient is close to 0 dB for a considerably large frequency band. The worst performances are obtained for β = 5°, when the aperture of the waveguide based on PEC-PMC walls is very narrow. For higher vales of β the reflection is smaller than -38 dB all over the band between 7 and 13 GHz. It is also found that the characteristics impedance of the TEM-mode is approximately equal to 377Ω for all the β angles. A snapshot of the electric field in the *xy* plane of the PTD-symmetric bent waveguide is presented in Fig.6.11. It is shown that the field propagates with very low backscattering.

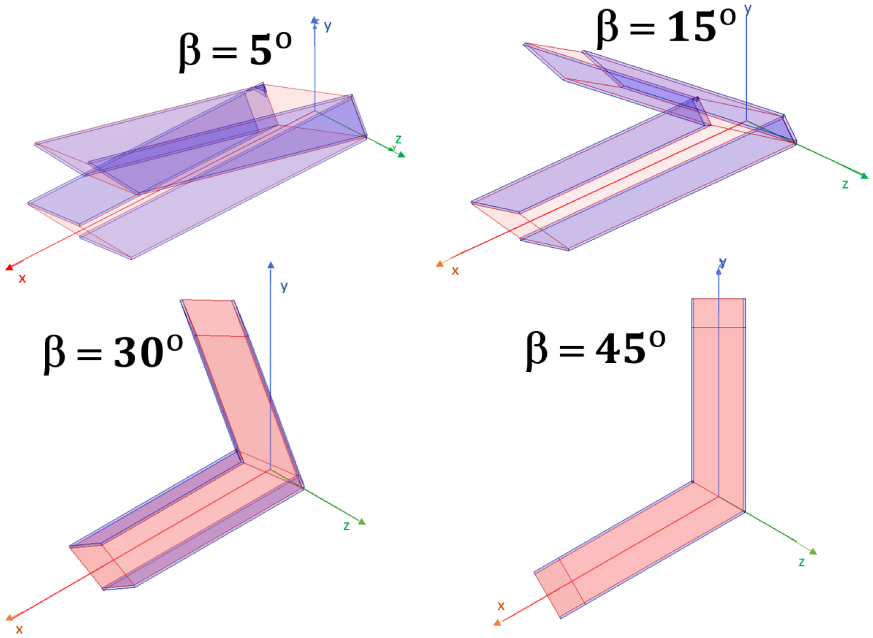

Figure 6.9: Geometry of PTD-symmetric waveguide bend for different values of β.

6.4 PEC-PMC dual polarized TEM waveguide array

Basic geometrical configuration of an open ended square TEM waveguide is reported in Fig. 6.2 corresponds very low reflection coefficient. In order to assess the dual polarized behavior, an arrangement of two square waveguides WG1 and WG2 are mutually oriented alongside the diagonal of X-axis such as to form rohmbic structure [See in Fig. 6.12 (I)] has been implemented. The arrangement is such that the array exhibits a PTD-symmetry w.r.t the planes with normal $\hat{n} = 1/\sqrt{2}(\hat{x} \pm \hat{y})$. The achieved reflection coefficients S_{11} is below -45 dB while the coupling coefficients S_{12} between both ports are below and -59 dB for the frequency band between 3 to 5 GHz, which is extremely low. It also emphasis's that the reflection and coupling almost vanishes if the arrangement respects PTD-symmetry. However, if the square waveguide (WG2) is arrange along y-axis in such a way that individually they satisfy PTD-symmetry property but togather they don't as presented in Fig. 6.12(II). Therefore, the achieved reflection coefficients S_{11} is below -26 dB. This

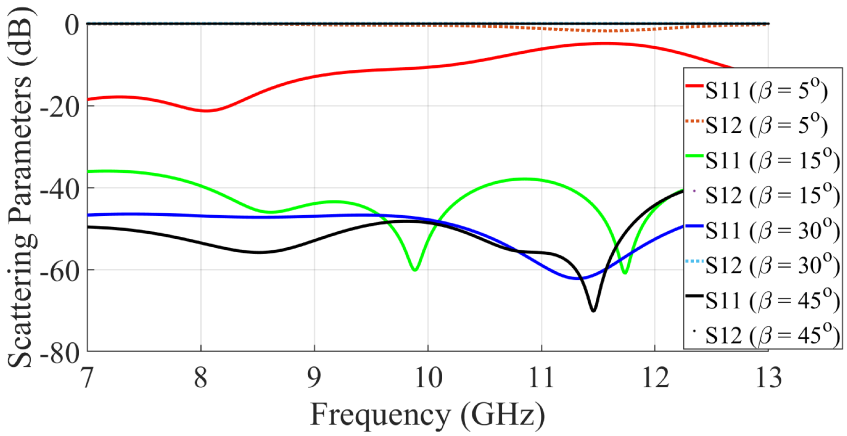

Figure 6.10: Simulated Scattering parameters of the PTD-symmetric waveguide bend for different values of β.

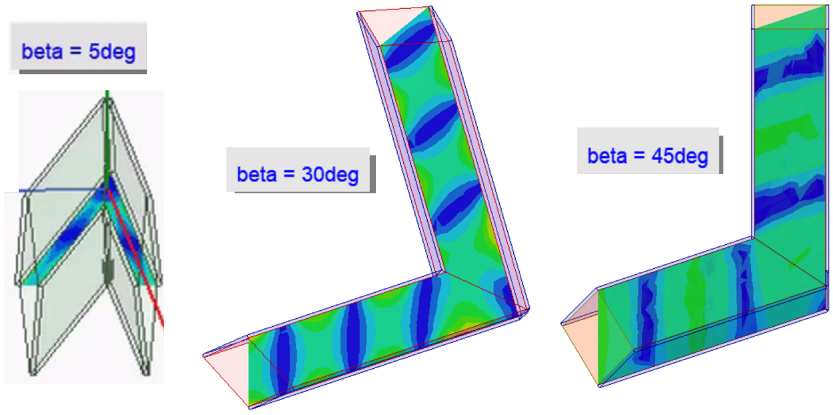

Figure 6.11: Snapshot of the simulated electric field of PTD-symmetric waveguide bend for different vales of β.

indicates the unavoidable deterioration while the coupling coefficients S_{12} is below -12 dB.

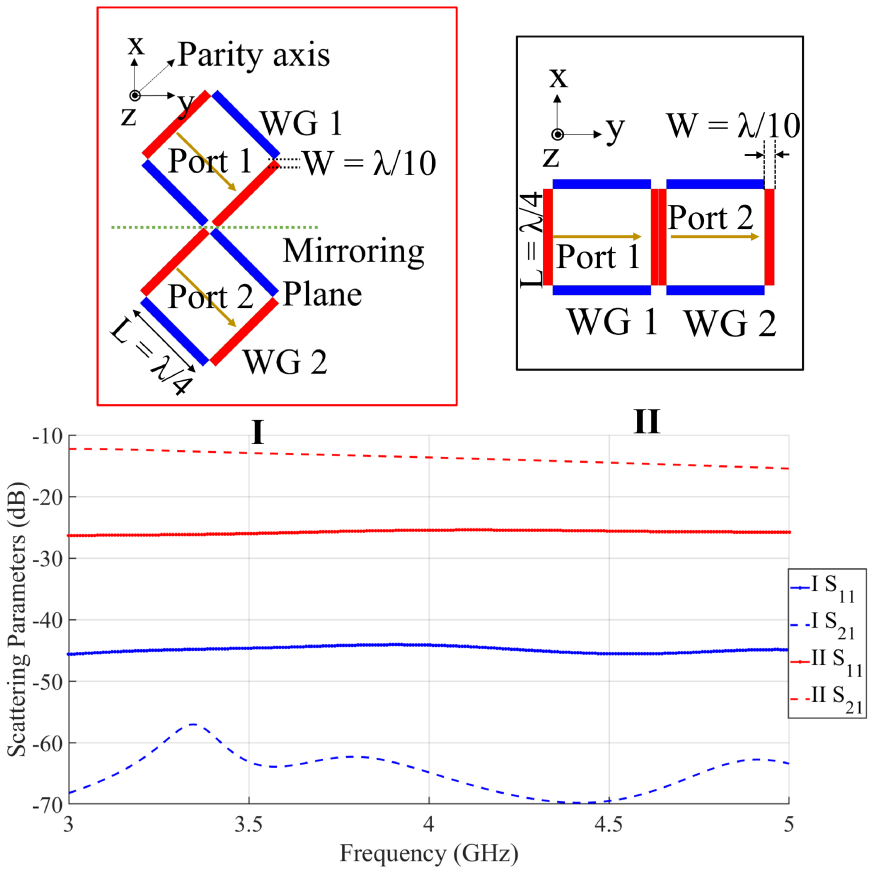

Figure 6.12: Simulated scattering parameters of I (Dual ports square WGs array (rohmbic arrangement of WG2 w.r.t WG1), II (Dual ports square WGs generic arrangement).

6.4.1 Wide Angle impedance matching (WAIM)

To investigate the wide angle impedance matching (WAIM) properties the configuration shown in the inset of Fig. 6.13 is considered. This 4x4 square waveguide is capable of electronic beam scanning through control of phase at the input ports. To assess the scanning capability, the radiation of the array is analyzed along three different scanning planes $\phi = 0°$, $22.5°$ and $45°$. The reflection and coupling coefficients vs. scan angle θ are reported in Fig. 6.14 for various ϕ angles at the central

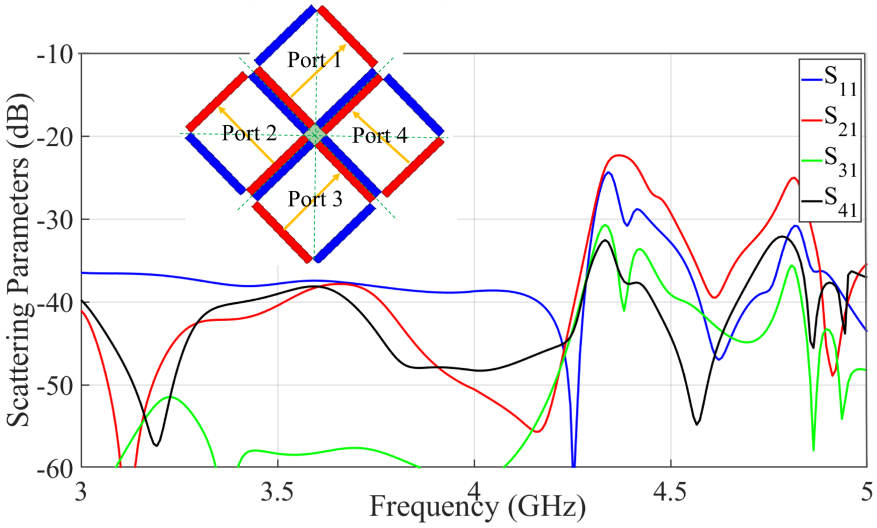

Figure 6.13: Geometry for the unit cell of the PTD-symmetric edge waveguide.

frequency of 3.5 GHz. For $\phi = 0^\circ$ the active reflection coefficient (solid line) is below -30 dB for almost all the elevation angles. Moreover, the coupling coefficients (dotted line) are below -29 dB. Similarly, for $\phi = 45^\circ$ the active reflection coefficient and coupling is below -39 dB, -29 dB respectively. Notice that the these two planes are symmetry axis. However, its performance deteriorates when the scanning is done along $\phi = 22.5^\circ$ [see insect of Fig. 6.14 plane is highlighted in black color] which is not the symmetry axis. Overall the active reflection coefficient and all the coupling coefficients have quite satisfactory performance. Due to implementation constrains, finite thickness boundary conditions have to be used. As a consequence, a small borehole (gray color in the inset of Fig. 6.13), which is an artifact, has been created in the center of the reference system. This acts as another square waveguide and has to be taken into consideration in analyzing the efficiency of the array. As part of the power flows in the hole between Waveguides and this decreases the structure efficiency. The electric field distribution inside the WG is presented in Fig. 6.15. For easy understanding the WG arrangement given in the inset of in Fig. 6.12(II) is considered. The extra backward radiation flowing through borehole between WG1 and WG2 is highlighted with the port at WG1 is excited. This extra flow of energy can be minimized by applying the PTD-symmetric metallic flange (PEC-PMC) at the opening of waveguide.

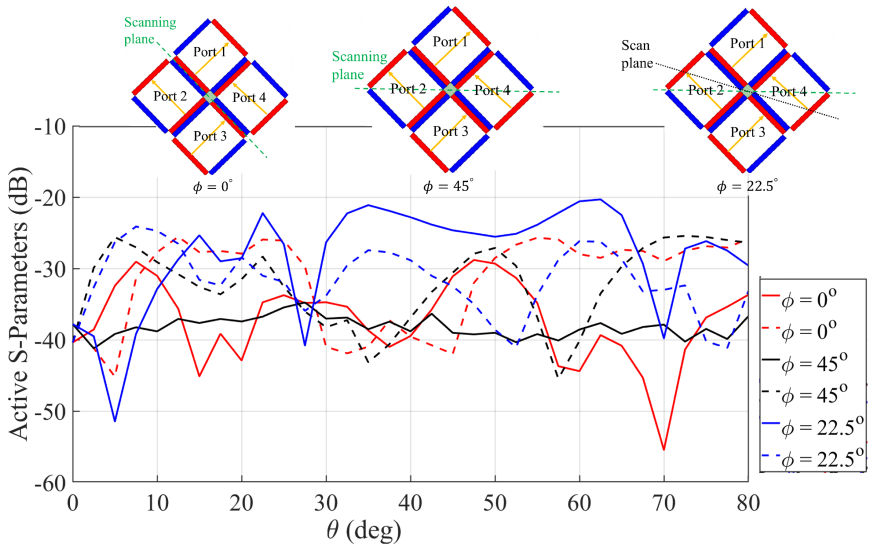

Figure 6.14: Beamscanning of the 4 ports square waveguide for different scanning plane; Reflections (solid line), Coupling (Dotted line).

6.5 Checkerboard dual polarized TEM Waveguide array

This array consists of a dense distribution of TEM waveguides open in a plane which is the combination of PEC and PMC walls As shown in Fig. 6.16(a). Since the front view resembles a checkerboard, it is referred in this article as checkerboard dual polarized TEM waveguide array. The red and blue colored square boxes denote PEC and PMC BCs, respectively. Alternating PEC and PMC square boxes on the aperture plane avoids holes (the central one we observed in previous case (6.15)) while maintaining the PTD-symmetry. According to PTD theory one possible discontinuity is opening to free space. This implies that, when a PTD-symmetric TEM waveguide is open ended to free space through a flange that still respects the PTD symmetry, there is no reflection inside the waveguide due to the discontinuity, whatever the dimension of the aperture is. The external flange should anyway be PTD symmetric w.r.t the same axis as the internal one. This particular configuration of the aperture plane preserves the PTD-symmetry even in the infinite environment is indicated in Fig. 6.16(b). The TEM waveguides in this case are also arranged in

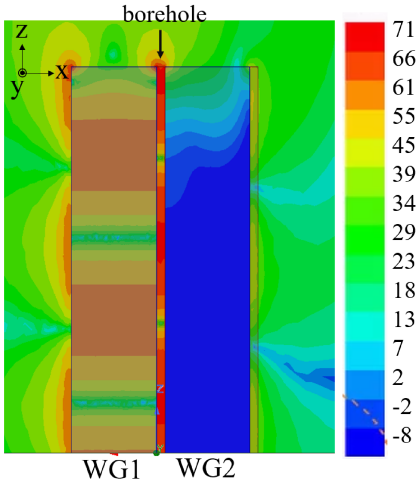

Figure 6.15: Electric Field inside the PTD-symmetric square waveguide (rohmbic arrangement of WG2 w.r.t WG1 with port at WG1 exited).

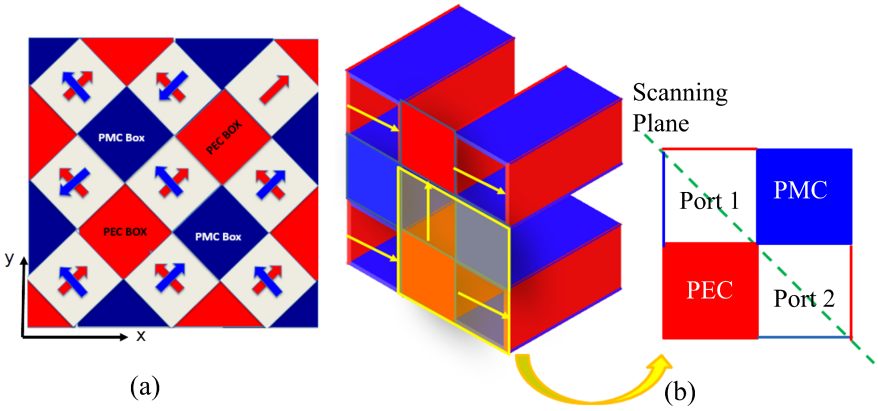

Figure 6.16: Geometry for checkerboard TEM waveguide array.

such a way that contiguous ports are cross polarized. The side dimension of the WG apertures are chosen as L= $\frac{\lambda}{4}$. The length of the open ended waveguide along the direction of propagation is set to 100 mm as shown in the inset of Fig. 6.17. It also

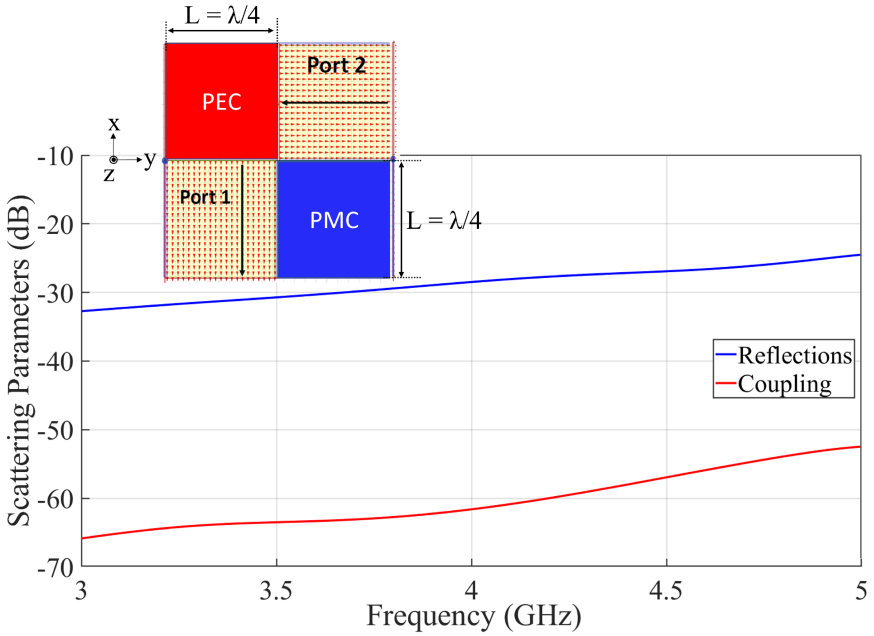

Figure 6.17: Active Reflection (Solid line) and coupling (dotted line) coefficients (dB) as a function of the scanning angle θ at 3.5 GHz.

presents that the simulated reflection coefficients is smaller than -33 dB, while the isolation between cross-polarized ports below -52 dB. This is considerable between frequency band 3 to 5 GHz when Port 1 is excited.

6.5.1 Wide Angle impedance matching (WAIM)

It is interesting to cast the checkerboard dual polarized TEM waveguide array given in the inset of Fig. 6.17 in a scanning array while maintaining (WAIM) properties. Therefore, symmetry BCs are placed on the basic cell (i.e., for broadside radiation). To assess the scanning, the radiation of the array is analyzed in $\phi = 0^\circ$ plane (xz-plane in inset of Fig. 6.18); for beam scanning in elevation $\theta = 0^\circ$ to approximately $\pm 80^\circ$. An active S-parameter (red color) for $\phi = 0^\circ$ obtained is less than -10 dB for θ between 0° to approximately $\pm 35^\circ$ and coupling is below -52 dB. Similarly, in case of $\phi = 45^\circ$ (along symmetry axis) the S-parameter (black color) is below -25 dB and coupling below -20 dB upto $\theta = 45^\circ$. However, $\phi = 22.5^\circ$ shows the

reflection below -10 dB until $\theta = \pm 45^{\circ}$ and coupling below -20 dB upto $\theta = \pm 55^{\circ}$.

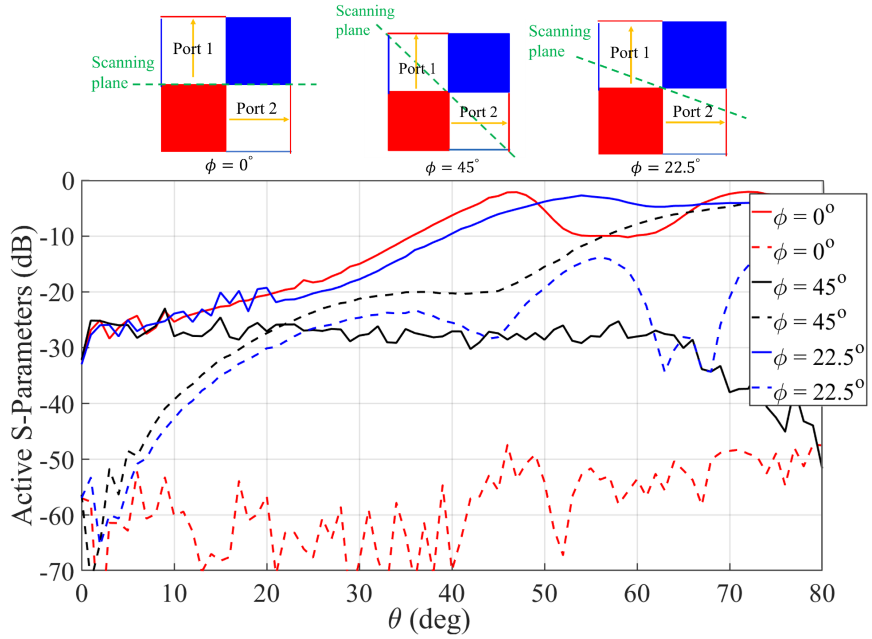

Figure 6.18: Active Reflection (Solid line) and coupling (dotted line) coefficients (dB) as a function of the scanning angle θ at 3.5 GHz.

6.6 Implementation of TEM Waveguide with High Impedance metasurface (MTS)

For practical implementation with high impedance metasurfaces, the supported mode does not have a zero-cut-off frequency. It only exists in a certain bandwidth around the frequency where the metasurface exhibits an equivalent PMC behavior. The practical implementation of the ideal PEC-PMC TEM waveguide in Fig. 6.2 is performed by using a mushroom type metasurface [38] to emulate PMC. The unit cell of this metasurface consists of a square patch printed on a grounded dielectric substrate and connected to the ground plane through a central via, as shown in the inset of Fig. 6.19. Following geometrical parameters have been selected: size of the unit cell $P = 30$ mm, square patch $L = 20$ mm, via radius $r = 0.5$ mm. The

space between the PEC wall and the top of the mushroom is filled by a dielectric with relative permittivity $\varepsilon_r = 2.08$ and has a thickness $h = 4$ mm. Both walls along x-axis are assigned PEC BCs. The resulting structure has been analyzed with [1] HFSSv2022. The dispersion diagram reported in Fig. 6.19, emphasizes the fact that

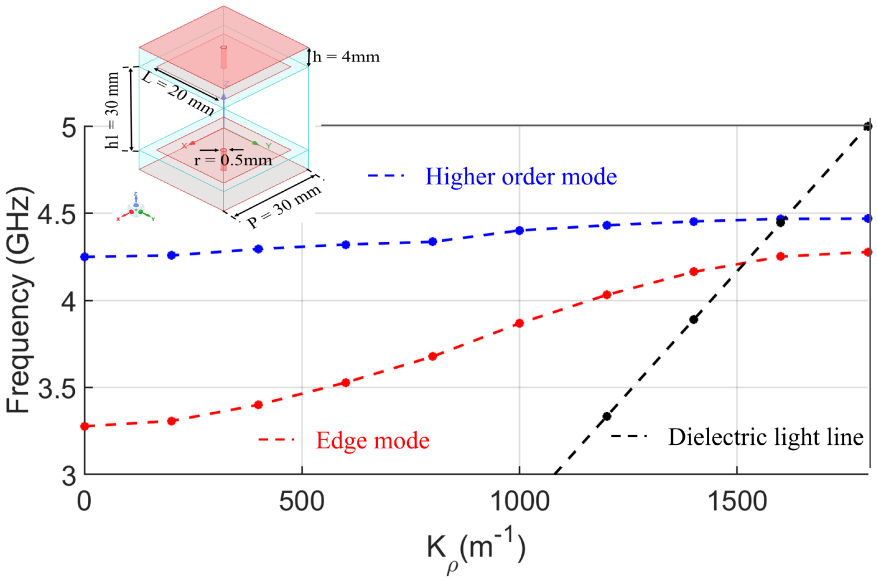

Figure 6.19: Dispersion diagram of of the unit cell implemented with mushroom type MTS shown in the same inset.

the light line crosses the dispersion curve at the frequency where the mushroom surface better emulates the PMC. Around this point, the dominant mode is quasi-TEM. In fact, for the ideal PEC-PMC BCs, the supported mode is TEM [20], [2], but the practical implementation of the PMC through mushrooms introduces a dispersion effect, so that the mode will be quasi-TEM. The unimodal bandwidth ranges from 3.4 GHz to 4.3 GHz.

The basic PEC-PMC square TEM-waveguide is implemented by using 5 mushroom unit cells on top and 5 on bottom while PEC boundary conditions are applied on both sides in y-axis. PEC-PMC based ideal BCs waveguide has been used to fed this structure as shown in the inset of Fig. 6.20. The purpose of using ideal BCs feeding is just to be sure that the dominant mode propagating inside WG is TEM mode. The size of the feeding WG has been optimized to achieve good matching over the frequency band of interest. The scattering parameters at the ideal WG ports

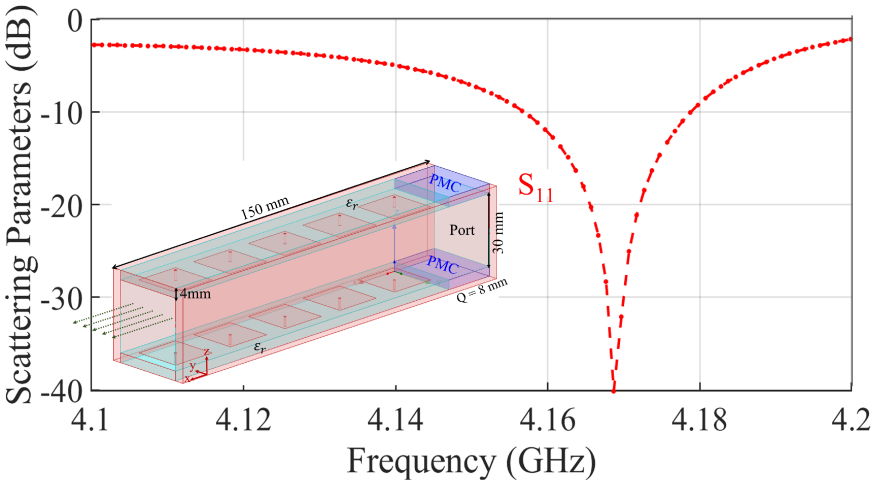

Figure 6.20: TEM square waveguide, PMC is realized by using mushroom MTS and Simulated reflection coefficients(dB)

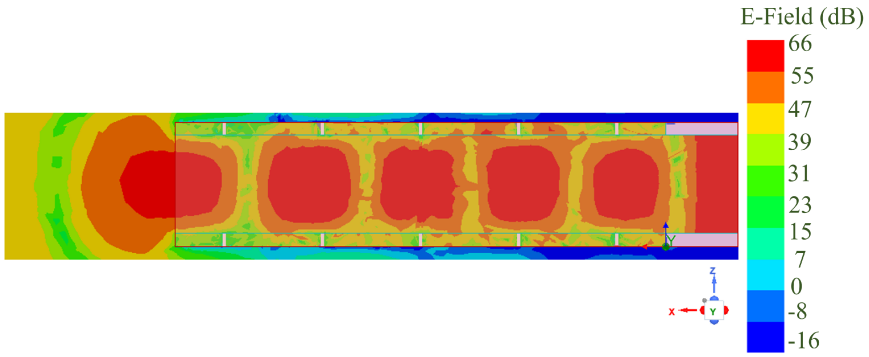

Figure 6.21: Electric field inside the TEM waveguide by using mushroom type MTS at 4.17 GHz.

are shown in Fig. 6.20. it is found that the scattering coefficient is below -10 dB for the bandwidth between 4.15 to 4.18 GHz. Fig. 6.21 presents the propagation of electric field inside the waveguide.

6.7 Summary of the chapter

In this chapter the properties of a bent PTD-symmetric square waveguide constituted by PEC-PMC walls have been investigated. This waveguide supports unimodal TEM mode propagation protected against backscattering from deformations and defects that preserve the PTD-symmetry. This property is also preserved when folding the bent waveguide, thus obtaining a flexible waveguide. The characteristic impedance of the TEM mode coincides with the wave impedance of the mode and with the free-space, and this is obtained for all the folded configurations. Also the wide angle impedance matching properties of an ideal PTD-symmetric square and checkerboard waveguide array composed by cross-polarized TEM waveguides are investigated. The mode supported by each waveguide is protected from the backscattering arising from the class of discontinuities which does not break the PTD-symmetry, including its free space transition. The assessment of the beam-scanning capability of the PTD-symmetric square and checkerboard waveguide array has shown quite satisfactory matching and coupling coefficients for different scanning angles. A square TEM waveguide in which two PEC walls and PMC wall with no of mushroom unit cells is used. its shows considerable matching for the frequency between 4.15 to 4.18 GHz. The waveguides with such characteristic have great potential to be used in many applications like communication and radar systems.

Chapter 7

Conclusion

This chapter summarizes the contribution of the thesis and discusses potential for future research.

7.1 Summary of contribution

The increased interest in protected edge mode transmission line for scientific applications has opened many opportunities for researchers. PTD Symmetric structures can provide backscattering protection even at large discontinuities when these latter respect this symmetry. A PTD-invariant structure consisting of a parallel PEC-PMC plate waveguide, which theoretically supports a unimodal TEM propagation, has been numerically analyzed. It is found that the fundamental propagating mode in this waveguide is protected against backscattering from local perturbations that satisfy the PTD-symmetry condition. A practical implementation of the waveguide can be obtained by using a mushroom structure to emulate the PMC boundary conditions. Despite the passivity and the absence of non-reciprocal elements, the transmission line does not suffer from reflections for any PTD-symmetric discontinuity. The unimodal bandwidth obtained by mushroom-type PTD-symmetric line is related to the modal bandgap associated with the mushroom structure, as expected. This indicates that the unimodal bandwidth has a minimum and a maximum frequency, rather than starting at zero frequency. The propagating mode in the unimodal bandwidth assumes the characteristics of a TEM mode only around the point where the light line and mode dispersion curve intersects. The practical

feasibility of the unidirectional structure has been demonstrated by experiments in the range 20-30 GHz. Despite manufacturing challenges, experimental results have been found completely satisfactory concerning for using the new PTD-symmetric line as a quasi TEM transmission line.

A switchable coupler based on PTD-symmetric transmission line has been realized in which each port is significantly coupled with only one other port (Chap 4). The structure, with a central portion consisting of top and bottom mushroom MTS, can be made reconfigurable by using pin diodes that short circuit to the ground of the mushrooms surface, thus, emulating a ground plane. By acting on the pin diodes it will then be possible to invert the coupled ports. This possibility has been confirmed by a full wave analysis and verified by experimental results, the latter obtained without the switches.

An all metal-gap waveguide in which metallic pins is used to emulate a PMC surface has been also studied (Chap 5). It is found that an unimodal bandwidth can be obtained where TEM propagation features is verified at the point where the light line crossing and the modal dispersion curve intersect. By properly designing the pins, the TEM bandwidth can be improved with respect to that employing mushroom-type MTS. Full wave simulation analysis have confirmed that PEC-Pillars waveguide provides propagation protection from backscattering even if the experimental feasibility of the unidirectional structure is still under manufacturing phase.

According to PTD theory one possible discontinuity is opening to free space. Hence, open-ended PTD-symmetric edge transmission lines can be used as reflectionless antennas. In this case, an important issue is concerned with the boundary conditions at the open-end of the line. The absence of internal reflections is ensured only if the boundary condition at the open end satisfies the PTD symmetry. Although in principle this can be realized by using mushrooms also in the external flange, it is difficult to create a reasonable approximation of PMC in the transition from internal to external boundaries, namely in the practical termination. The additional difficulty is that any external PTD symmetric junction can create additional allowable unidirectional paths along PEC-PMC junctions that redirect the power along these lines more than in free space, thus subtracting power to the desired free space radiation. The above phenomenon limits, if not prevents, the use of open ended PTD line as radiating elements in arrays. As well as PTD-symmetric elements (such as a square element with two PEC and two PMC parallel walls), the alternance of PTD-symmetric elements like the ones we have investigated (Chap 6), seems to inevitably channel power in line-boundary along the free-space interface,

creating undesired coupling paths. However, full wave simulation analysis shows that the active reflection coefficient in infinite array configuration (made with ideal PEC-PMC boundary conditions) for different scanning planes provides satisfactory results.

7.2 Directions for future work

The research outcomes of this thesis work may open the possibility to design and fabricate several types of reconfigurable devices at microwaves, up to 30 GHz, such as directional switches, splitters, filters, and resonators. Alternative configurations, as PTD-symmetry protected edge mode with single layer complementary impedance surfaces (capacitive and inductive) can provide easy solutions towards flexible devices. The extension of PTD-symmetry protected edge mode to the non-reciprocal materials could also be a future topic of interest. Similarly, this work may also be complemented by the design an equivalent DB boundary that behaves as a PEC for TE mode and as a PMC for a TM mode, and is therefore self-dual. The use of DB boundary in the flange would allow to satisfy the PTD symmetry thus, providing a well matched open ended PTD line. At the same time, since the DB boundary prevents any propagation along the surface, it is also expected to provide good decoupling among radiating elements when arranged in an array configuration.

Chapter 8

Publications

This research activity has led to several publications in international journals and conferences. These are summarized below.

International Journals

1. **I. Nadeem**, V. Verri, E. Martini, F. Morgia, A. Toccofondi, M. Mattivi, S. Maci. "Experimental Verification of Backscattering Protection in PTD-Symmetric Bifilar Edge Waveguides", *IEEE Transaction on Antenna & Propagation*, vol. in press, 2022. [DOI:10.1007/s11042-010-0643-7]

2. **I. Nadeem**, V. Verri, E. Martini, F. Morgia, A. Toccofondi, M. Mattivi, S. Maci. "Switchable Edge-line Coupler Based on Parity Time-Reversal Duality Symmetry", *Scientific Reports*, vol. 48, iss. 2, pp. 313-337, 2022. [DOI: 10.1007/s11042-009-0342-4]

3. **I. Nadeem**, E. Martini, A. Toccofondi, S. Maci. "Flexible Unidirectional PTD-Symmetric waveguide", *URSI Radio Science letters*, vol. 3, iss. 1, p. 51, 2021. [DOI: 10.46620/21-0051]

Submitted

1. **I. Nadeem**, E. Martini, A. Toccofondi, S. Maci. "Wide angle impedance matching (WAIM) of PTD-symmetric open ended waveguide arrays", *IEEE Antenna & Wave propagation letters*, 2022. (Submitted)

2. **I. Nadeem**, E. Martini, A. Toccofondi, E. Rajo, S. Maci. "Implementation of a Fully

Metal PTD-Symmetric Bifilar Edge Waveguid", in *17th European Conference on Antennas & Propagation (EuCAP)*, Florence (Italy), Submitted 2023.

In Preparation

1. **I. Nadeem**, E. Martini, A. Toccofondi, E. Rajo, S. Maci. "Edge Mode Excitation in a Fully Metal PTD-Symmetric Bifilar Edge Waveguide", in *IEEE Transaction on Antenna & Propagation*.

International Conferences

1. **I. Nadeem**, E. Martini, A. Toccofondi, S. Maci. "Open Ended PTD Symmetric Bifilar Edge Line (PTD-BEL) Arrays", in *Proc. of IEEE International Symposium on Antennas & Propagation and Radio science meeting USNC-URSI (APS/URSI)* , Denver (USA), 2022.

2. **I. Nadeem**, E. Martini, A. Toccofondi, S. Maci. "Implementation of an Open Ended PTD-Symmetric Edge Waveguide", in *16th European Conference on Antennas & Propagation (EuCAP)*, Madrid (Spain), pp. 1-4, 2022.

3. **I. Nadeem**, V. Verri, E. Martini, A. Toccofondi, S. Maci. "Study of PTD-Symmetric Square-Waveguide", in *Proc. of the IEEE International Symposium on Antennas & Propagation and Radio science meeting USNC-URSI (APS/URSI)*, Singapore , 2021.

4. **I. Nadeem**, V. Verri, E. Martini, A. Toccofondi, S. Maci. "PTD-Symmetric Square-Waveguide Array Based on Complementary Boundary Conditions", in *Proc. of of the 15th International Congress on Artificial Materials for Novel Wave Phenomena-Metamaterials*,New York, (USA), 2021.

5. **I. Nadeem**, V. Verri, E. Martini, A.Toccofondi, S. Maci. "Active Impedance of PTD-Symmetric Checkerboard Type Open Ended Waveguide Arrays ", in *Proc. of the 15th European Conference on Antenna & Propagation (EuCAP)*, Dusseldrof, (Germany), 2021.

6. **I. Nadeem**, E. Martini, A.Toccofondi, S. Maci. "Properties of Z-type open-ended waveguide arrays ", in *Proc. of IEEE International Symposium on Antennas & Propagation and Radio science meeting USNC-URSI (APS/URSI)* , Quebec, (Canada), 2020.

7. **I. Nadeem**, E. Martini, A. Toccofondi, S. Maci. "PTD Symmetric Switchable Bifilar Edge Line Coupler using Complementary Boundary Conditions", in *Proc. of the 16th International Congress on Artificial Materials for Novel Wave Phenomena-Metamaterials*, Siena (Italy), 2022.

Technical Reports

1. **I. Nadeem**, E. Martini, A. Toccofondi, and S. Maci. “PTD Symmetric Structures”, Huawei Milan & Munich, Technical Report, 2022.

Bibliography

[1] Ansys, "HFSS," https://www.ansys.com/it-it/products/electronics/ansys-hfss.

[2] E. Martini, M. Silveirinha, and S. Maci, "Transformation method for ptd symmetric edge waveguide," in *IEEE 13th European Conference on Antennas and Propagation (EuCAP)*, Mar. 2019, pp. 1–3.

[3] M. C. Rechtsman, J. M. Zeuner, Y. Plotnik, Y. Lumer, D. Podolsky, F. Dreisow, S. Nolte, M. Segev, and A. Szameit, "Photonic floquet topological insulators," *Nature*, vol. 496, no. 7444, pp. 196–200, Apr. 2013.

[4] M. G. Silveirinha, "symmetry-protected scattering anomaly in optics," *Phys. Rev. B*, vol. 95, p. 035153, Jan. 2017.

[5] F. Haldane and D. M., "Nobel lecture: Topological quantum matter," *Rev. Mod. Phys.*, vol. 89, p. 040502, Oct. 2017.

[6] F. Haldane and S. Raghu, "Possible realization of directional optical waveguides in photonic crystals with broken time-reversal symmetry," *Physical Review Letters*, vol. 100, no. 1, Jan. 2008.

[7] R. Davis, Y. Zhou, P. Bandaru, D. Sievenpiper *et al.*, "Photonic topological insulators: A beginner's introduction [electromagnetic perspectives]," *IEEE Antennas and Propagation Magazine*, vol. 63, no. 3, pp. 112–124, 2021.

[8] S. Raghu and F. D. M. Haldane, "Analogs of quantum-hall-effect edge states in photonic crystals," *Phys. Rev. A*, vol. 78, p. 033834, Sept. 2008.

[9] Z. Wang, Y. Chong, J. D. Joannopoulos, and M. Soljačic, "Observation of unidirectional backscattering-immune topological electromagnetic states," *Nature*, vol. 461, no. 7265, pp. 772–775, Oct. 2009.

[10] D. J. Bisharat and D. F. Sievenpiper, "Guiding waves along an infinitesimal line between impedance surfaces," *Phys. Rev. Lett.*, vol. 119, p. 106802, Sept. 2017.

[11] H. Lira, Z. Yu, S. Fan, and M. Lipson, "Electrically driven nonreciprocity induced by interband photonic transition on a silicon chip," *Physical review letters*, vol. 109, no. 3, p. 033901, Jul. 2012.

[12] M. G. Silveirinha, "Chern invariants for continuous media," *Physical Review B*, vol. 92, no. 12, p. 125153, 2015.

[13] W. Gao, M. Lawrence, B. Yang, F. Liu, F. Fang, B. Béri, J. Li, and S. Zhang, "Topological photonic phase in chiral hyperbolic metamaterials," *Physical review letters*, vol. 114, no. 3, p. 037402, 2015.

[14] M. G. Silveirinha, "Z_2 topological index for continuous photonic materials," *Phys. Rev. B*, vol. 93, p. 075110, Feb. 2016.

[15] F. Liu and J. Li, "Gauge field optics with anisotropic media," *Physical review letters*, vol. 114, no. 10, p. 103902, 2015.

[16] A. B. Khanikaev, S. H. Mousavi, W.-K. Tse, M. Kargarian, A. H. MacDonald, and G. Shvets, "Photonic topological insulators," *Nature materials*, vol. 12, no. 3, pp. 233–239, Dec. 2013.

[17] R. J. Davis and D. F. Sievenpiper, "Robust microwave transport via nontrivial duality-based rhombic unit cells," in *2021 IEEE International Symposium on Antennas and Propagation and USNC-URSI Radio Science Meeting (APS/URSI)*. IEEE, 2021, pp. 619–620.

[18] W.-J. Chen, Z.-Q. Zhang, J.-W. Dong, and C. T. Chan, "Symmetry-protected transport in a pseudospin-polarized waveguide," *Nature communications*, vol. 6, no. 1, pp. 1–8, Sept. 2015.

[19] D. J. Bisharat and D. F. Sievenpiper, "Electromagnetic-dual metasurfaces for topological states along a 1d interface," *Laser & Photonics Reviews*, vol. 13, no. 10, p. 1900126, 2019.

[20] E. Martini, M. G. Silveirinha, and S. Maci, "Exact solution for the protected tem edge mode in a ptd-symmetric parallel-plate waveguide," *IEEE Transactions on Antennas and Propagation*, vol. 67, no. 2, pp. 1035–1044, Nov. 2018.

[21] A. Li, S. Singh, and D. Sievenpiper, "Metasurfaces and their applications," *Nanophotonics*, vol. 7, no. 6, pp. 989–1011, 2018.

[22] O. Quevedo-Teruel, H. Chen, A. Díaz-Rubio, G. Gok, A. Grbic, G. Minatti, E. Martini, S. Maci, G. V. Eleftheriades, M. Chen *et al.*, "Roadmap on metasurfaces," *Journal of Optics*, vol. 21, no. 7, p. 073002, 2019.

[23] Y. Yuan, K. Zhang, B. Ratni, Q. Song, X. Ding, Q. Wu, S. N. Burokur, and P. Genevet, "Independent phase modulation for quadruplex polarization channels enabled by chirality-assisted geometric-phase metasurfaces," *Nature communications*, vol. 11, no. 1, pp. 1–9, 2020.

[24] K. Zhang, Y. Wang, S. N. Burokur, and Q. Wu, "Generating dual-polarized vortex beam by detour phase: From phase gradient metasurfaces to metagratings," *IEEE Transactions on Microwave Theory and Techniques*, vol. 70, no. 1, pp. 200–209, 2021.

[25] X. Kong, J. B. Dia'aaldin, G. Xiao, and D. F. Sievenpiper, "Analytic theory of an edge mode between impedance surfaces," *Physical Review A*, vol. 99, no. 3, p. 033842, 2019.

[26] Z. Xu and D. F. Sievenpiper, "Interface waves in parallel-plate metasurface waveguides with duality symmetry," in *2021 IEEE International Symposium on Antennas and Propagation and USNC-URSI Radio Science Meeting (APS/URSI)*, 2021, pp. 1978–1979.

[27] Z. Xu, J. Chang, S. Fang, Q. Zhang, R. J. Davis, D. Sievenpiper, and T. J. Cui, "Line waves existing at junctions of dual impedance metasurfaces," *ACS Photonics*, June 2021.

[28] I. Nadeem, V. Valentina, E. Martini, A. Toccafondi, and S. Maci, "Active impedance of ptd-symmetric checkerboard type open ended waveguide array," in *Proceedings of the 15th European Conference on Antenna and Propagation (EuCap), Virtual Conference*. IEEE, March 2021.

[29] ——, "Ptd-symmetric square-waveguide array based on complementary boundary conditions," in *Proceedings of the 15th International Congress on Artificial Materials for Novel Wave Phenomena Metamaterials*, Aug. 2021.

[30] V. G. Daniele and R. Zich, *The Wiener Hopf method in electromagnetics*. SciTech Publishing Incorporated, 2014.

[31] R. Mittra, "Analytical techniques in the theory of guided waves," *Macmillan Series in Electrical Science*, 1971.

[32] F. Yang and Y. Rahmat Samii, "Reflection phase characterizations of the ebg ground plane for low profile wire antenna applications," *IEEE Transactions on antennas and propagation*, vol. 51, no. 10, pp. 2691–2703, 2003.

[33] R. King, D. Thiel, and K. Park, "The synthesis of surface reactance using an artificial dielectric," *IEEE Transactions on Antennas and propagation*, vol. 31, no. 3, pp. 471–476, 1983.

[34] P. A. Belov, R. Marques, S. I. Maslovski, I. S. Nefedov, M. Silveirinha, C. R. Simovski, and S. A. Tretyakov, "Strong spatial dispersion in wire media in the very large wavelength limit," *Physical Review B*, vol. 67, no. 11, p. 113103, 2003.

[35] M. G. Silveirinha, C. A. Fernandes, and J. R. Costa, "Electromagnetic characterization of textured surfaces formed by metallic pins," *IEEE Transactions on Antennas and Propagation*, vol. 56, no. 2, pp. 405–415, 2008.

[36] D. R. Smith, W. J. Padilla, D. C. Vier, S. C. Nemat-Nasser, and S. Schultz, "Composite medium with simultaneously negative permeability and permittivity," *Phys. Rev. Lett.*, vol. 84, pp. 4184–4187, May 2000.

[37] M. G. Silveirinha, "Additional boundary condition for the wire medium," *IEEE transactions on antennas and propagation*, vol. 54, no. 6, pp. 1766–1780, 2006.

[38] D. Sievenpiper, L. Zhang, R. F. Broas, N. G. Alexopolous, and E. Yablonovitch, "High-impedance electromagnetic surfaces with a forbidden frequency band," *IEEE Transactions on Microwave Theory and techniques*, vol. 47, no. 11, pp. 2059–2074, Nov. 1999.

[39] O. Luukkonen, M. G. Silveirinha, A. B. Yakovlev, C. R. Simovski, I. S. Nefedov, and S. A. Tretyakov, "Effects of spatial dispersion on reflection from mushroom-type artificial impedance surfaces," *IEEE Transactions on Microwave Theory and Techniques*, vol. 57, no. 11, pp. 2692–2699, 2009.

[40] O. Luukkonen, C. Simovski, G. Granet, G. Goussetis, D. Lioubtchenko, A. V. Raisanen, and S. A. Tretyakov, "Simple and accurate analytical model of planar grids and high-impedance surfaces comprising metal strips or patches," *IEEE Transactions on Antennas and Propagation*, vol. 56, no. 6, pp. 1624–1632, 2008.

[41] S. Tretyakov, *Analytical modeling in applied electromagnetics*. Artech House, 2003.

[42] I. Nadeem, V. Verri, E. Martini, F. Morgia, A. Toccafondi, M. Mattivi, and S. Maci, "Experimental verification of backscattering protection in ptd-symmetric bifilar edge waveguides," *IEEE Transactions on Antennas and Propagation*, 2022.

[43] A. Hessel, M. H. Chen, R. C. Li, and A. A. Oliner, "Propagation in periodically loaded waveguides with higher symmetries," *Proceedings of the IEEE*, vol. 61, no. 2, pp. 183–195, 1973.

[44] M. Kehn, M. Nannetti, A. Cucini, S. Maci, and P.-S. Kildal, "Analysis of dispersion in dipole-fss loaded hard rectangular waveguide," *IEEE Transactions on Antennas and Propagation*, vol. 54, no. 8, pp. 2275–2282, Aug. 2006.

[45] X.-P. Chen and K. Wu, "Low loss ultra wideband transition between conductor backed coplanar waveguide and substrate integrated waveguide," in *IEEE MTT S International Microwave Symposium Digest*, June 2009, pp. 349–352.

[46] Z. Wang, S. Adhikari, D. Dousset, C.-W. Park, and K. Wu, "Substrate integrated waveguide (siw) power amplifier using cbcpw-to-siw transition for matching network," in *IEEE/MTT-S International Microwave Symposium Digest*, June 2012, pp. 1–3.

[47] F. Taringou, J. Bornemann, and K. Wu, "Broadband coplanar-waveguide and microstrip low-noise amplifier hybrid integrations for k-band substrate integrated waveguide applications on low-permittivity substrate," *IET Microwaves, Antennas & Propagation*, vol. 8, no. 2, pp. 99–103, Jan. 2014.

[48] M. Salehi and E. Mehrshahi, "A closed form formula for dispersion characteristics of fundamental siw mode," *IEEE Microwave and Wireless Components Letters*, vol. 21, pp. 4–6, Dec. 2011.

[49] D. Deslandes and K. Wu, "Accurate modeling, wave mechanisms, and design considerations of a substrate integrated waveguide," *IEEE Transactions on microwave theory and techniques*, vol. 54, no. 6, pp. 2516–2526, June 2006.

[50] I. Nadeem, V. Verri, E. Martini, F. Morgia, M. Mattivi, A. Toccafondi, and S. Maci, "Switchable edge-line coupler based on parity time-reversal duality symmetry," *Scientific Reports*, vol. 12, no. 1, pp. 1–12, 2022.

[51] S. Cohn and R. Levy, "History of microwave passive components with particular attention to directional couplers," *IEEE Transactions on Microwave Theory and Techniques*, vol. 32, no. 9, pp. 1046–1054, 1984.

[52] R. Levy, "Directional couplers," in *Advances in Microwaves*, L. Young, Ed. New York: Academic, 1966, vol. 1, p. 115â209.

[53] B. Liu, W. Hong, Z. C. Hao, and K. Wu, "Substrate integrated waveguide 180-degree narrow-wall directional coupler," in *2005 Asia-Pacific Microwave Conference Proceedings*, vol. 1, 2005, pp. 3 pp.–.

[54] T. Djerafi and K. Wu, "Super-compact substrate integrated waveguide cruciform directional coupler," *IEEE Microwave and Wireless Components Letters*, vol. 17, no. 11, pp. 757–759, 2007.

[55] F. Parment, A. Ghiotto, T.-P. Vuong, J.-M. Duchamp, and K. Wu, "Broadband directional moreno coupler for high-performance air-filled siw-based substrate integrated systems," in *2016 IEEE MTT-S International Microwave Symposium (IMS)*, 2016, pp. 1–3.

[56] A. Doghri, T. Djerafi, A. Ghiotto, and K. Wu, "Substrate integrated waveguide directional couplers for compact three-dimensional integrated circuits," *IEEE Transactions on Microwave Theory and Techniques*, vol. 63, no. 1, pp. 209–221, 2015.

[57] M. Zhou, J. Shao, B. Arigong, H. Ren, R. Zhou, and H. Zhang, "A varactor based 90 $^{\circ}$ directional coupler with tunable coupling ratios and reconfigurable responses," *IEEE Transactions on Microwave Theory and Techniques*, vol. 62, no. 3, pp. 416–421, 2014.

[58] P.-L. Chi and T.-C. Hsu, "Highly reconfigurable quadrature coupler with ideal impedance matching and port isolation," *IEEE Transactions on Microwave Theory and Techniques*, vol. 65, no. 8, pp. 2930–2941, 2017.

[59] S. Y. Zheng, W. S. Chan, and Y. S. Wong, "Reconfigurable rf quadrature patch hybrid coupler," *IEEE Transactions on Industrial Electronics*, vol. 60, no. 8, pp. 3349–3359, 2013.

[60] R. Zhang, M. F. Hagag, L. Yang, R. Gomez Garcia, and D. Peroulis, "A flexible quadrature coupler with reconfigurable frequency and coupling ratio in switchable coupling direction," *IEEE Transactions on Microwave Theory and Techniques*, vol. 67, no. 8, pp. 3391–3402, 2019.

[61] H. N. Chu and T. G. Ma, "A coupler with wide power division ratio tuning range and flexible coupling direction," *IEEE Microwave and Wireless Components Letters*, vol. 31, no. 2, pp. 121–124, 2021.

[62] MACOM, "Ma4fcp200 data sheet," https://cdn.macom.com/datasheets/MA4FCP200.pdf.

[63] E. Rajo-Iglesias, M. Ferrando-Rocher, and A. U. Zaman, "Gap waveguide technology for millimeter-wave antenna systems," *IEEE Communications Magazine*, vol. 56, no. 7, pp. 14–20, 2018.

[64] F. Yang and Y. Rahmat-Samii, *Surface electromagnetics: with applications in antenna, microwave, and optical engineering*. Cambridge University Press, 2019.

[65] M. S. Sorkherizi and A. A. Kishk, "Fully printed gap waveguide with facilitated design properties," *IEEE Microwave and Wireless Components Letters*, vol. 26, no. 9, pp. 657–659, 2016.

[66] P.-S. Kildal, E. Alfonso, A. Valero-Nogueira, and E. Rajo-Iglesias, "Local metamaterial-based waveguides in gaps between parallel metal plates," *IEEE Antennas and wireless propagation letters*, vol. 8, pp. 84–87, 2008.

[67] A. U. Zaman, M. Alexanderson, T. Vukusic, and P.-S. Kildal, "Gap waveguide pmc packaging for improved isolation of circuit components in high-frequency microwave modules," *IEEE Transactions on Components, Packaging and Manufacturing Technology*, vol. 4, no. 1, pp. 16–25, 2013.

[68] E. Rajo-Iglesias and P.-S. Kildal, "Numerical studies of bandwidth of parallel-plate cut-off realised by a bed of nails, corrugations and mushroom-type electromagnetic bandgap for use in gap waveguides," *IET microwaves, antennas & propagation*, vol. 5, no. 3, pp. 282–289, 2011.

[69] A. Valero-Nogueira, M. Baquero, J. I. Herranz, J. Domenech, E. Alfonso, and A. Vila, "Gap waveguides using a suspended strip on a bed of nails," *IEEE Antennas and Wireless Propagation Letters*, vol. 10, pp. 1006–1009, 2011.

[70] F. Fan, J. Yang, and P.-S. Kildal, "Half-height pins-a new pin form in gap waveguide for easy manufacturing," in *2016 10th European Conference on Antennas and Propagation (EuCAP)*. IEEE, 2016, pp. 1–4.

[71] A. Hessel, M. H. Chen, R. Li, and A. Oliner, "Propagation in periodically loaded waveguides with higher symmetries," *Proceedings of the IEEE*, vol. 61, no. 2, pp. 183–195, 1973.

[72] M. Ebrahimpouri, O. Quevedo-Teruel, and E. Rajo-Iglesias, "Design guidelines for gap waveguide technology based on glide-symmetric holey structures," *IEEE microwave and wireless components letters*, vol. 27, no. 6, pp. 542–544, 2017.

[73] W. Yuan, J. F. Chen, C. Zhang, W. X. Tang, L. Wang, Q. Cheng, and T. J. Cui, "Glide-symmetric lens antenna in gap waveguide technology," *IEEE Transactions on Antennas and Propagation*, vol. 68, no. 4, pp. 2612–2620, 2019.

[74] O. Dahlberg, R. Mitchell-Thomas, and O. Quevedo-Teruel, "Reducing the dispersion of periodic structures with twist and polar glide symmetries," *Scientific reports*, vol. 7, no. 1, pp. 1–6, 2017.

[75] M. Ebrahimpouri, E. Rajo-Iglesias, Z. Sipus, and O. Quevedo-Teruel, "Cost-effective gap waveguide technology based on glide-symmetric holey ebg structures," *IEEE Transactions on Microwave Theory and Techniques*, vol. 66, no. 2, pp. 927–934, 2017.

[76] Z. Sipus, K. Cavar, M. Bosiljevac, and E. Rajo-Iglesias, "Glide-symmetric holey structures applied to waveguide technology: design considerations," *Sensors*, vol. 20, no. 23, p. 6871, 2020.

[77] I. Nadeem, E. Martini, A. Toccafondi, and S. Maci, "Flexible unidirectional ptd-symmetric waveguide," *URSI Radio Science Letters*, vol. 3, p. 51, 2021.

[78] M. N. M. Kehn and P.-S. Kildal, "Miniaturized rectangular hard waveguides for use in multifrequency phased arrays," *IEEE Transactions on Antennas and Propagation*, vol. 53, no. 1, pp. 100–109, 2005.

[79] M. N. M. Kehn and L. Shafai, "Characterization of dense focal plane array feeds for parabolic reflectors in achieving closely overlapping or widely separated multiple beams," *Radio Science*, vol. 44, no. 3, pp. 1–25, 2009.

[80] M. N. M. Kehn and P.-S. Kildal, "The n-guide: A novel miniaturized hard quasi-tem waveguide," in *IEEE Antennas and Propagation Society International Symposium. Digest. Held in conjunction with: USNC/CNC/URSI North American Radio Sci. Meeting (Cat. No. 03CH37450)*, vol. 2. IEEE, 2003, pp. 1111–1114.

[81] S. Hopfer, "The design of ridged waveguides," *IRE Transactions on Microwave Theory and Techniques*, vol. 3, no. 5, pp. 20–29, 1955.

[82] V. Komarov, "Classification of metallic waveguides with complex cross-sections," *IEEE Proceedings Microwave Antennas and Propagation*, vol. 148, no. 6, pp. 398–402, 2001.

[83] F.-R. Yang, K.-P. Ma, Y. Qian, and T. Itoh, "A novel tem waveguide using uniplanar compact photonic-bandgap (uc-pbg) structure," *IEEE Transactions on microwave theory and techniques*, vol. 47, no. 11, pp. 2092–2098, 1999.

Author's Information

Iram Nadeem, *a researcher and author, was born and raised in Taxila, one of the oldest cities founded in 1000 BCE, located in Pakistan. Her doctoral research, carried out in collaboration with Huawei Research center Munich and Milan, focuses on Protected Edge Modes in Metasurface Junctions with specific reference to Parity Time reversal Duality Symmetric structures.*

During her PhD, she was awarded two grants based on her academic profile: the TICRA-EurAAP Grants-2022 and the Dr. Mojgan Daneshmand Grant-2022. She also conducted research as a visiting researcher at University Carlos III Madrid, Spain, investigating Glide Symmetry along with PTD symmetry.

Iram holds an M.Eng degree in Information and Communication Engineering from Chosun University in South Korea, which she received on a full-time scholarship from the Korean Government in 2018. From 2018 to 2019, she worked as a researcher in the Department of Information and Communication Engineering at Chosun University, focusing on ultra-wideband antenna design for location detection applications.

Additionally, Iram has an M.S. in Telecommunication Engineering, with a major in Optical Fiber Communication, and a B.S. in Electrical Engineering, with a major in Power Systems, both from the University of Engineering and Technology (UET) Taxila, Pakistan. From 2011 to 2015, she worked as a lecturer and lab engineer in different engineering institutes of Pakistan.

Iram's research interests include Higher order symmetries, Gap-wave technology, UWB, and MIMO antenna design. Her work has been published in several reputable journals and conferences throughout her career.